UNIVERSITY OF MINNESOTA

This is to certify that I have examined this copy of a master's thesis by

Thomas Kenneth Johnson

and have found that it is complete and satisfactory in all respects,

and that any and all revisions required by the final

examining committee have been made.

Vicki L. Hansen

Name of Faculty Adviser

Signature of Faculty Adviser

October 27, 2009

Date

Structural, Kinematic, and Hydrothermal Fluid Investigation of the Gold-Bearing Murray Shear Zone, northeastern Minnesota

A THESIS

SUBMITTED TO THE FACULTY OF THE GRADUATE SCHOOL

OF THE UNIVERSITY OF MINNESOTA

BY

Thomas Kenneth Johnson

IN PARTIAL FULFILLMENT OF THE REQUIREMENTS

FOR THE DEGREE OF

MASTER OF SCIENCE

Advisers: Vicki L. Hansen and George J. Hudak

October 2009

Acknowledgements

Without the support of my family, advisors, and close friends this thesis would not be possible. I would like to thank my mother, Carol, for her belief in me, her belief in the value of education, and for her amazing humanity for no better word describes her. My father, Ken, I thank for his instruction through the years on how to believe in myself and in my abilities while staying true in a troubled world. I thank Lindsay, my future wife, for her support, love, and for her beauty both inside and out. I'd also like to thank my advisers Vicki and George. I thank Vicki for her utmost support when I chose to start this journey, for instilling in me the value of science, and for her kind mentorship. I thank George for his ability to make any topic interesting and for sharing his time with me.

Abstract

Gold mineralization within Archean granite greenstone terrains of northeastern Minnesota continues to be enigmatic despite its known association to shear zones, faults, and folds. As products of deformational events shear zones, faults, and folds localize fluid transportation and ultimately gold mineralization. Their kinematic history and structural architecture contain important clues about the genesis, characteristics, and mechanics of ore-bearing fluids. The Murray Shear Zone of northeastern Minnesota hosts subeconomic gold in a unique structural setting. Evidence exists in support of shear zone-hosted gold mineralization that coincides with established models for well-known and profitable gold deposits of other Archean greenstone terrains. This thesis presents a structural, kinematic, and hydrothermal fluid investigation of the Murray Shear Zone with implications for gold mineralization. Field and laboratory research such as structural mapping, analysis of thin sections for microstructures and deformation mechanisms, and geochemical study was conducted to provide a comprehensive look at gold mineralization processes of the Murray Shear Zone.

TABLE OF CONTENTS

LIST OF FIGURES

LIST OF TABLES

APPENDIX

I. INTRODUCTION

Archean (3.8-2.5 Ga) cratons throughout the world host lode-gold deposits within granite greenstone terranes (Figure 1). Known gold deposits within granite greenstone terranes of the Superior province of North America are associated with shear zones, faults, or fold hinges, all of which provide structural settings for fluid transportation and mineral deposition. Mapping of and exploration within these terranes of northeastern Minnesota, primarily in the past 30 years, uncovered numerous subeconomic gold showings. Northeastern Minnesota has yet to host a gold mine, although gold showings exist within both the Murray and Mud Creek Shear Zones of this region (Figure 2). Like all ancient shear zones, the Murray Shear Zone offers a present-day narrowed view of broad regional deformation events; it records a long history of crustal deformation and translation accompanied by metamorphism, fluid flow, and mineralization. Study of the Murray Shear Zone facilitates enhanced understanding of gold potential within the historically undeveloped district in northeastern Minnesota.

Previous geologic mapping (Peterson and Jirsa 1999; Peterson 2001; and Peterson and Patelke 2003) identified the Murray Shear Zone as a steeply dipping, east-west trending wedge-shaped shear zone (Figures 3a, b).

Figure 1 (next page): World map showing the distribution of gold deposits in metamorphic terranes. Data from the Geological Survey of Canada world gold database. Local deposits: 19 = Duport; 20 = Hemlo; 21 = Renabie; 22 = Canadian Arrow; 23 = East Malartic; 24 = Clearwater; 25 = Cooke. See Goldfarb (2005) for entire listing. Modified from Goldfarb (2005).

Geological World Map with Locations of Other Gold Deposits

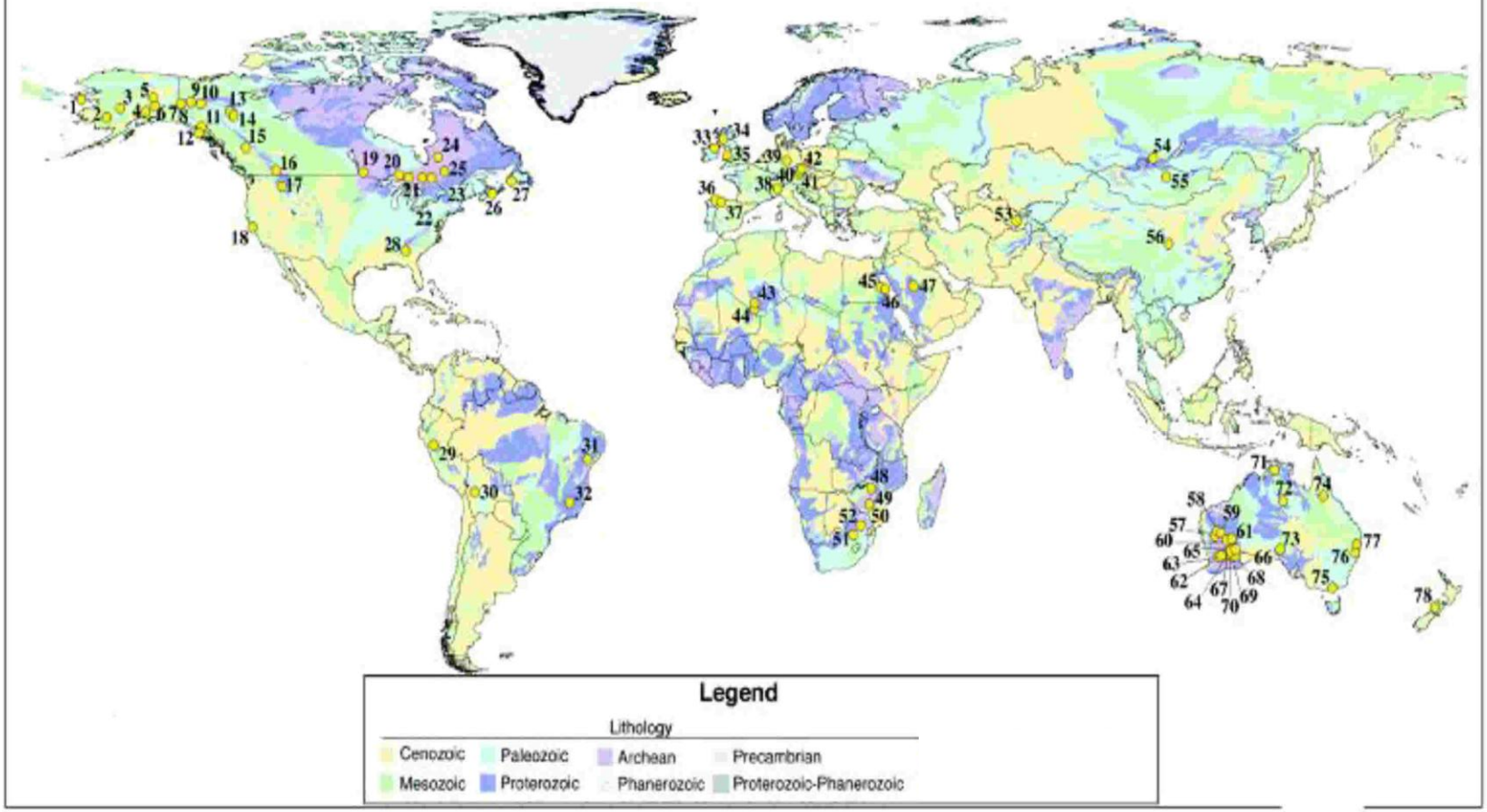

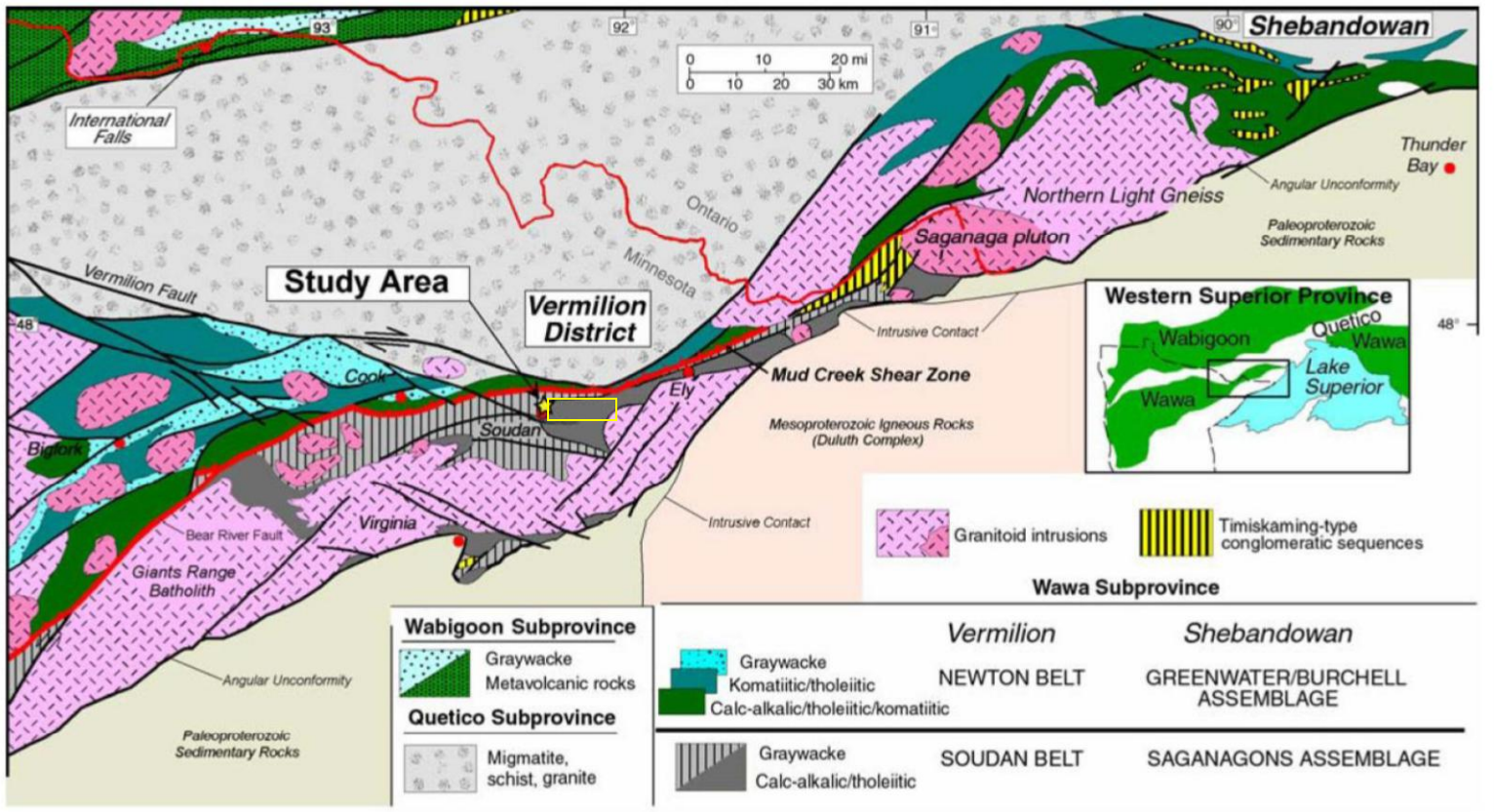

Figure 2: Regional geology map of the Vermilion district showing simplified Archean assemblages. Also shown are the Murray Shear Zone of this study (yellow box) and Mud Creek Shear Zone. Inset shows major subprovinces of the southwestern Superior province. Modified from Peterson and Patelke (2003).

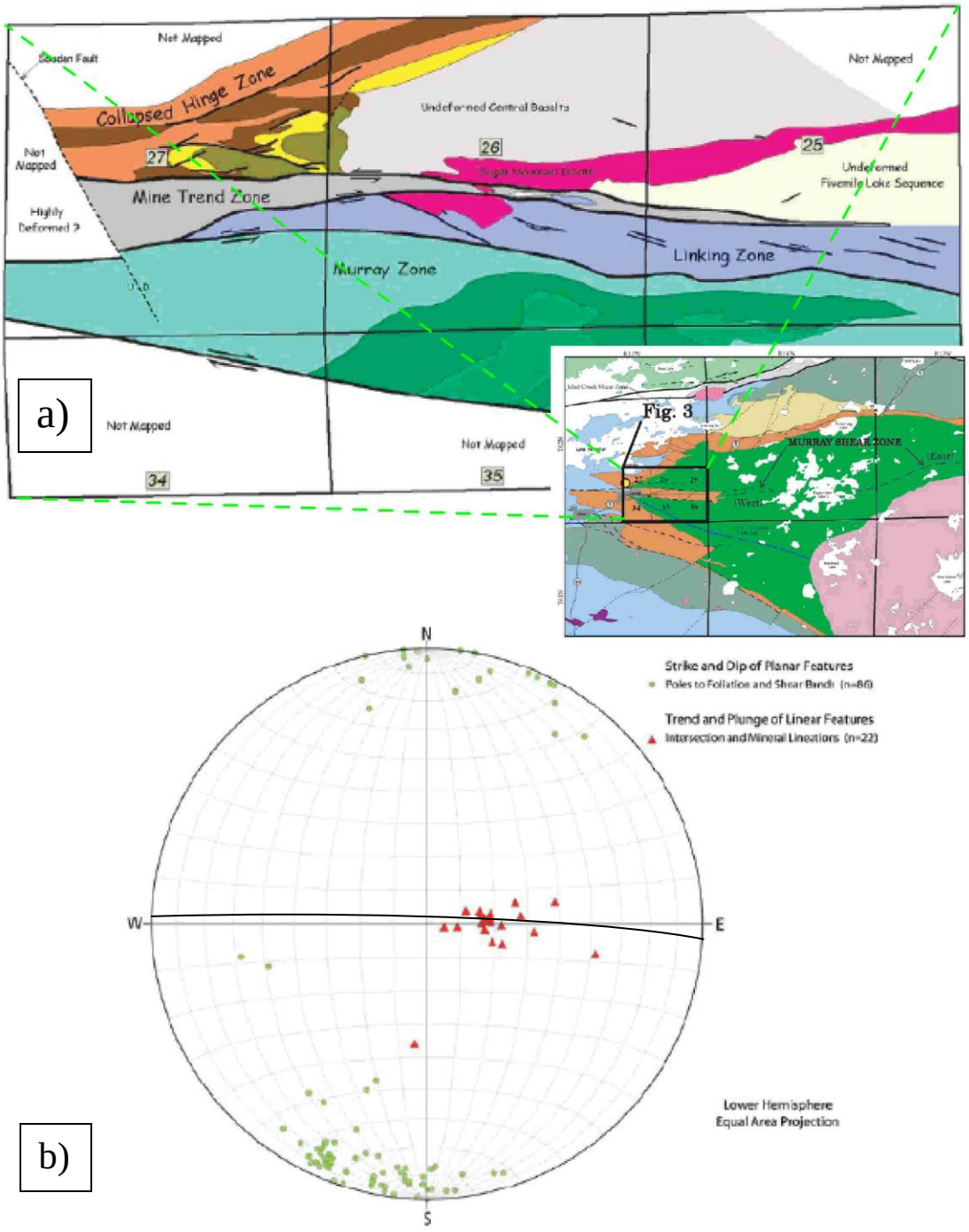

Figure 3: Interpretation and data from previous geologic mapping in the Murray Shear Zone (MSZ); a) Structural domain map of the western 6 km of MSZ; b) Stereonet equal area projections of foliations (avg. foliation in black line), shear fabrics, and linear features. Inset location of MSZ western 6 km. From Peterson and Patelke (2003).

West of Eagles Nest Lake, the Murray Shear Zone splays from an east-west corridor into curvilinear belts of highly strained rock (Figure 3). To the east of Eagles Nest Lake, the location and extent of the Murray Shear Zone are less constrained, although foliation trajectory focuses to sub-parallel in map view. In the middle to late 1980s, Newmont Mining Corporation discovered subeconomic gold mineralization (12.5 ppm) along the northern margin of the Murray Shear Zone (Figure 3a). Exploratory drill holes intersected anomalous gold, but substantial gold mineralization was not discovered at that time.

The structural architecture of the Murray Shear Zone is investigated herein as a suitable host for gold mineralization. Prior to field investigation and data collecting, a background investigation was conducted with the following primary objectives: 1) a specific look at processes that contribute to Archean gold mineralization (i.e. tectonic setting and source of fluids throughout a unique kinematic history), 2) the commonalities of similar structures in other parts of the world enriched with gold, and 3) the genetic and depositional models of enriched structures in an effort to determine why this particular shear zone is hitherto economically unproductive. With a thorough background investigation complete realization of the gold potential of this shear zone required detailed geologic mapping, kinematic and petrographic study, and lithogeochemical work.

This thesis consists of five parts; a) background investigation of Archean gold deposits and models; b) geological summary of the study area; c) structural investigation of the Murray Shear Zone including orientation, internal structure, and kinematic history;

d) lithogeochemical study of host rock lithology, metamorphic facies, alteration assemblages, and immobile and trace element analysis utilizing the isocon method (Grant, 1986); and e) interpretation of the data sets collected for this investigation and the connection to gold deposition within the Murray Shear Zone.

II. PERSPECTIVE AND REVIEW OF ARCHEAN GOLD MINERALIZATION

Deposits of Archean gold prove to be: 1) a vast resource for the world's precious metal demand; and 2) a moderately constrained scientific problem. Much of the world's production, manifested in everyday life, derives itself from an ancient source—over 2.5 billion years old. As significant are the academic challenges inherent in efforts to characterize such deposits including structure, depositional style, host rock lithology, and time scale.

1. Greenstone-Hosted Gold

Lode-gold deposits occur within Archean granite greenstone terrains of all Precambrian platforms (i.e., shields, blocks, basements, cratons) such as the Superior and Slave provinces of the Canadian shield, the Yilgarn and Pilbara blocks of Western Australia, the Kapvaal and Zimbabwean cratons of southern Africa, the West African and East African shields, the Guianan and Sao Franciscan cratons of South America, and the Archean terrain of central India (Figure 4a). Greenstone belts within these cratons contain 23,000 to 25,000 tonnes of gold in past production and defined resources (Goldfarb et al., 2001). Temporally, lode-gold mineralization is most prominent in Neoarchean terrains and only recurs in late Proterozoic and Phanerozoic orogenic belts. Early Proterozoic oxygenation of the atmosphere-hydrosphere may explain the temporal

gap in mineralization (Meyer, 1988). Most shear zone associated gold deposits are considered epigenetic in that they formed after emplacement of host lithology and during regional metamorphism. They occur in metamorphic terranes of mainly greenschist facies although sub-greenschist to lower amphibolite grade exists in some areas. Greenstone belts within the Vermilion District (Figure 4b) comprise a package of iron-formation, metavolcanic (mafic to felsic) and derivative metasedimentary rocks and domains of interfering intrusive rocks.

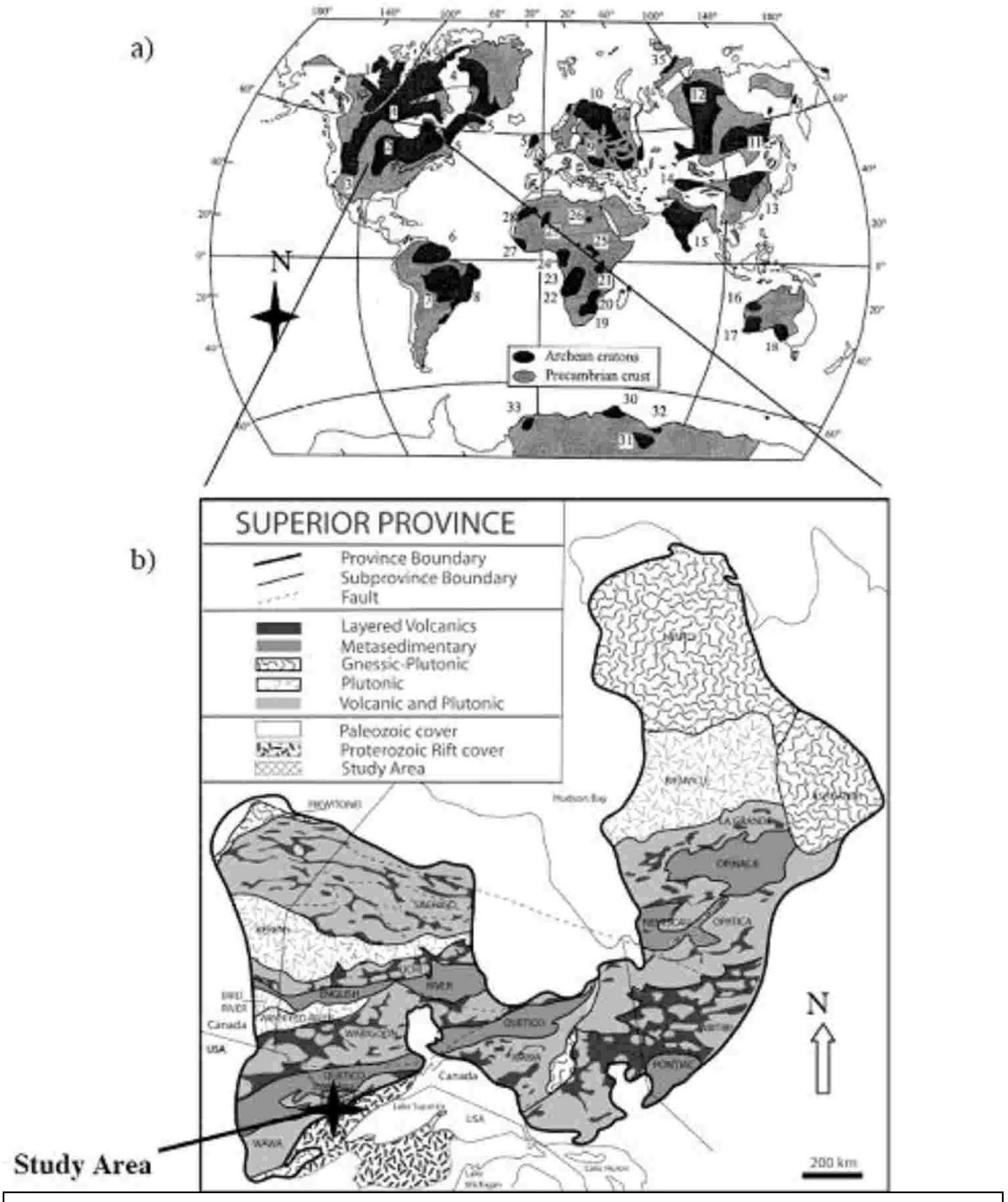

Figure 4: a) Archean Cratons/Provinces: 1=Slave, 2=Superior, 3=Wyoming, 4=Kaminak (Hearne), 5=North Atlantic (Nain, Godthaab, Lewisian), 6=Guiana, 7=Central Brazil (Guapore), 8=Atlantic (Sao Franscisco), 9=Ukranian, 10=Baltic (Kola), 11=Aldan, 12=Anabar, 13=Sino-Korean, 14=Tarim, 15=Indian, 16=Pilbara, 17=Yilgarn, 18=Gauwler, 19=Kaapvaal, 20=Zimbabwe, 21=Zambian, 22=Angolan, 23=Kasai, 24=Gabon, 25=Kibalian, 26=Uweinat, 27=Liberian, 28=Maritanian, 29=Ouzzalian, 30=napier Complex, 31=Prince Charles Mountains, 32= Vestfold Hills, 33=Heimefront Ranges, 34=deeply buried Archean rocks of East European Shield, 35=Tajmyr (adapted from Kusky and Polot, 1999). b) The Superior Province and subprovinces form a granite-greenstone terrain (adapted from Card, 1990; from Goodman, 2008).

1.2 Structural Control and Gold Mineralization

Perhaps the most obvious feature of greenstone-hosted gold deposits is their association with major crustal breaks. Ore can be found not in first order faults but in higher order, divergent splays; within relatively narrow, highly permeable structural pathways. Late, subsidiary deformation structures that branch off first order faults and shear zones host lode-gold deposits (Goldfarb et al., 2005 and references therein). The largest and most productive first-order deformation zones include the Porcupine-Destor and Larder Lake-Cadillac breaks of the Abitibi Greenstone Belt, Canada; the Campbell-Giant shear zone of Northwest Territories, Canada; the Boulder-Lefroy shear zone of the Eastern Gold Province, Australia; and the Champion Reef system, India. Mineralization styles within these structures consist of mostly lode-style vein fill (see below).

Structural complexity modulates gold endowment. Ductility contrasts within host rocks and brittle characteristics of specific lithologies create suitable conditions for fault fracture meshes and veining, whereby localized high-permeability conduits within otherwise low-permeability crust, allowing for episodic rapid flow of substantial fluid volumes (Sibson, 2004). Dilatant extensional fractures of fault-fracture meshes in compressive/transpressive environments are interlinked by low-displacement shears (Figure 5). Recent field mapping conducted within the Murray Shear Zone uncovered distinctive outcrop-scale deformational features that represent a high degree of structural complexity. Veining, faulting, and rheology contrasts highlight the potential for localized gold in brittle structures.

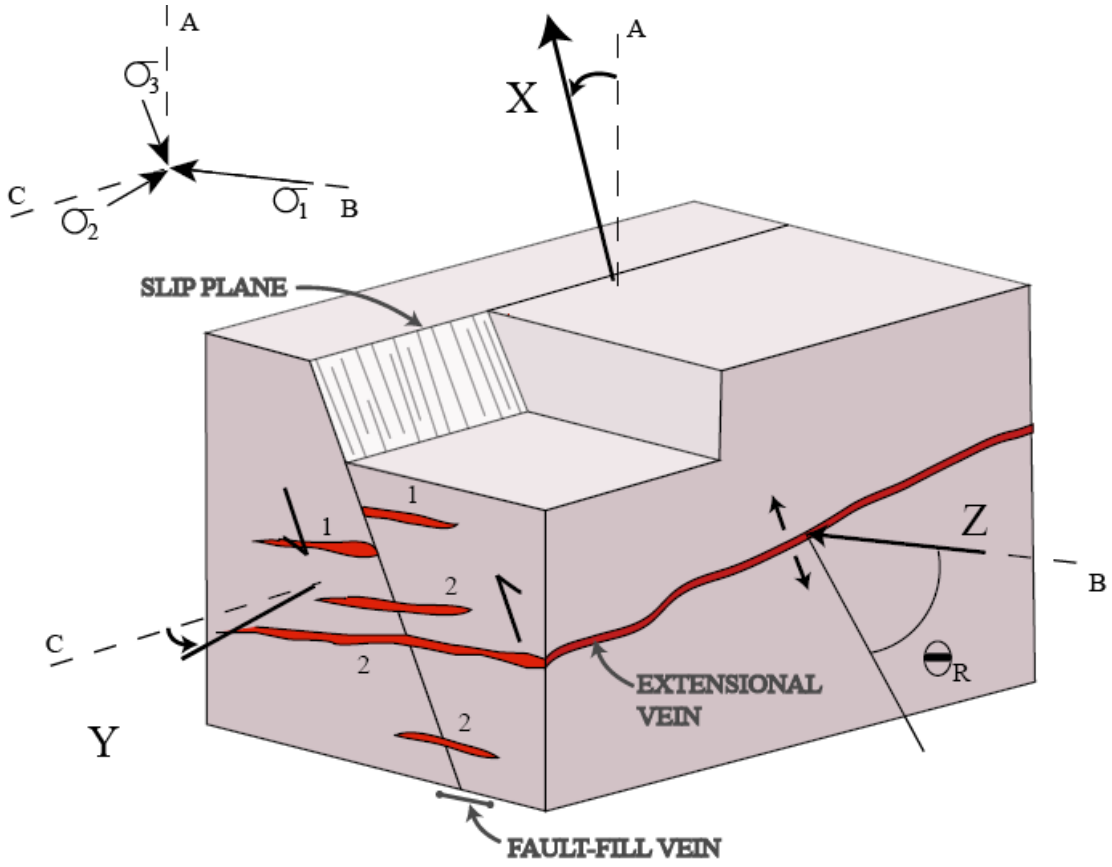

Figure 5: Block diagram illustrating a fault slip plane in a compressive environment. Dilational (opening) veins occur in a sequential pattern, time 1 precedes time 2 as overprinting and translation of earlier veins occurs during subsequent deformational events. The principal strain axes X and Y are shown oblique to the A-C plane. Maximum principal shortening (Z) is parallel to B. Also shown are principal stress axes and the angle of reactivation, Θ_R. See text for further discussion. Modified from Dube and Gosselin (2005).

2. Archean Gold Deposit Models

Models of Archean gold deposits facilitate deeper understanding with which to base exploration in shear zones. Various models attempt to consolidate commonalities in hydrothermal fluids, structure, depth in the crust, mineralization style, and other observations, between known gold deposits. For example, the unified genetic model

(Superior) of Kerrich and Wyman (1990), the crustal continuum model (Yilgarn) of Groves et al. (1991), and the depositional model (Superior) of Colvine (1989) asserts: 1) a deep source for the primary ore fluid with common constituents H_2O, NaCl, CO_2, CH_4, and $CaCl_2$; 2) structural control on mineralization style within shear zones, faults, and fold hinges; 3) sequential change in style of mineralization with increasing depth, which corresponds to a change in rheological behavior of the lithosphere from brittle to ductile; 4) common spatial association between gold deposits and intermediate to felsic, saturated to under-saturated intrusions (Hodgson and MacGeehan, 1982); and 5) late Archean timing of gold mineralization (Superior and Yilgarn cratons) from ca. 2660 to 2630 Ma (Robert et al., 2005).

2.1 Environmental Constraints on Gold Mineralization

Physical attributes shared amongst established gold deposits require three first-order assumptions: a) gold extracts from a local or proximal source to a structurally controlled setting; b) fluids transport gold into the structure; and c) tectonic forces drive lode-gold mineralization.

2.1(a) *Inherent Gold Source: Conceptual Models*

Many hypotheses exist for gold origination in greenstone-hosted deposits, but two contrasting conceptual models are at the forefront of discussion. The first invokes a complex, multistage and multiprocess explanation, called the depositional model. Initial sea floor hydrothermal activity forms stratiform auriferous exhalites followed by several possible types of later metamorphogenic remobilization, including shearing, within these strata, in order to form discordant epigenetic veins, vein systems, and stock works

(Boyle, 1976; Hutchinson, 1976; Foster and Wilson, 1984; Hutchinson and Burlington, 1984; Hutchinson, 1987). The second hypothesis, referred to as the genetic model, advocates a single stage of epigenetic emplacement by complex fluids generated from metamorphic dewatering reactions in structurally prepared, sheared, and brecciated rocks to form both concordant stratiform and discordant vein-type lodes (Colvine et al., 1984; Fyfe and Kerrich, 1984; from Hutchinson, 1987). The former model is indeed more complex in process and coincides with the idea that Earth's paleo-seafloor was gently rolling and undulating with black smokers and hydrothermal systems operating continuously, amid copious subaqueous and subaerial volcanism. As early Earth cooled and cratons stabilized, stratiform auriferous exhalites became incorporated into local stratigraphy, the source of gold thus created. The latter model relates closely with convergence and deformation producing anastomozing crustal-scale shear zones and associated strain patterns. Consequently, the boundary conditions and structural framework exist to host various styles of mineralization throughout a crustal profile from lower (ductile) to upper (brittle) regions. Dewatering of volatile-rich rocks, and/or magmatic fluids provide the constituent fluid species observed in mineralized deposits and metamorphic aureoles. In reality a combination of syn- and epigenetic processes may be responsible.

2.1(b) *The Role of Fluids*

Fluids play a critical role in gold deposition. Fluids provide: 1) a transporting medium to move soluble material; 2) a driving force for fracturing, and; 3) they influence mechanical/rheological properties of rocks, and therefore they affect the nature and extent

of deformation. Hydrothermal fluid, a ubiquitous agent and product of metamorphism, consists of hot H_2O- and CO_2-rich fluid derived from de-volatilizing intrusions at depth or lateral advection from wall rocks during deformation. Differing hypotheses on the composition of fluids relate to each conceptual model described above. The depositional model asserts that hydrothermal fluid is universal within an extensive mineralizing system. According to the model, structural conduits transport non-unique fluids in highly variable hosting lithology. This leads to many styles of mineralization and alteration (Colvine, 1989). However, fluid composition, temperature, and pressure vary spatially and temporally on most faults; there is no such thing as a typical fault fluid (Parry, 1998). Variations in mineralogy and fluid-inclusion characteristics of individual faults reveal separate fluids that differ in chemical composition but experience the same properties of state. This supports the implication that emphasis on the environment of deposition is imperative, rather than the fluids. Thus, a genetic model seems appropriate to explain lode-gold quartz vein systems. On the other hand, a source of gold may or may not be derived from metamorphic fluids and could possibly be remobilized in accordance with the depositional model.

2.1(c) *Tectonic Setting*

Lode-gold mineralization requires compressive or least-compressive tectonics. Regardless of gold sources or fluid composition, lode-gold mineralization calls on crustal instabilities from a principal stress differential as the driving force to fluid mobility and fractures. Heat from intrusive magmas also has the potential to drive fluid mobility and

therefore, fractures. Structural asymmetries (i.e. fractures, faults, and veins) support stress field involvement.

Differing tectonic regimes can potentially create a suitable structural environment for mineralization. Most conceptual models require a tectonically thickened crust. Field observations of structural asymmetry orientations with evidence of interacting hydrothermal fluid invoke shortening and stacking of the crust rather than subsidence and thinning. The unified genetic model, the crustal continuum model, and the depositional model postulate convergent margin orogenic events as responsible for field relationships. However, vertical tectonics in the form of rising granite domes and sinking greenstone cover rocks from gravitational density instabilities may produce similar field relationships. A strong link between vertical tectonics and mineralization is less established. As an exception, Lin (2005) demonstrates a genetic link between mineralization and sagduction/diapirism in some greenstone-hosted gold deposits of the northwestern Superior Province. In lieu of debate regarding Archean granite-greenstone formation the operative hypothesis is gold mineralization within structurally controlled, fluid-rich environments, which depend most directly on structural facies development, rheological evolution of the crust, and fluid availability, composition, and flow. The required structural architecture, rheology, and fluids might be achieved within different tectonic settings.

2.2 The Fault Model

Conceptual models of Archean gold mineralization exist independent of a specific orogenic process and free of locally-specific empirically-based parameters. Fault models

of Sibson et al. (1988); Boullier and Robert (1992); Byerlee (1993); and Robert et al. (1995) call upon cycles of fluid pressure fluctuations, vein formation, and hydrothermal self-sealing as the proper environment to generate mineralization. These authors suggest that mineralization results from precipitation under the influence of pressure and temperature fluctuations; host lithology and fault fluids are generic.

2.2(a) *How it Works*

Definition of variables for the following discussion: ℓ_f = fluid density, g = gravity, h_F = height of fluid column, ℓ_L = rock density, h_L = height of rock column.

At the brittle/ductile transition zone (Figure 6), hydrostatic pressure developed within the pore spaces of a rock (equal to the weight of an overlying column of water within those pore spaces; P_F = Pressure of the Fluid = $\ell_f g h_F$) may approach values close to lithostatic overburden pressure, or the weight of an overlying column of rock (P_L = Pressure of the overlying Lithosphere = $\ell_L g h_L$ = vertical stress, σ_V) if metamorphic fluids generated at depth are contained within a compressive regime. The brittle/ductile transition is associated with the mesothermal environment for mineralization and greenschist facies metamorphism. Fluid pressure at depth may be expressed as a relationship between hydrostatic and lithostatic pressures, known as the pore-fluid factor: $\lambda_v = P_F / \sigma_V$, where fluid pressure is *hydrostatic* when $\lambda_v \sim 0.4$, the ratio of water to rock densities (ℓ_f = 1000 kg/m^3 and ℓ_l = 2650 kg/m^3). Fluid pressures are *lithostatic* when they equal overburden pressures ($\lambda_v = 1.0$). Hydrostatic pressure build-up to lithostatic values

requires an impermeable cap rock or "load-bearing carapace"

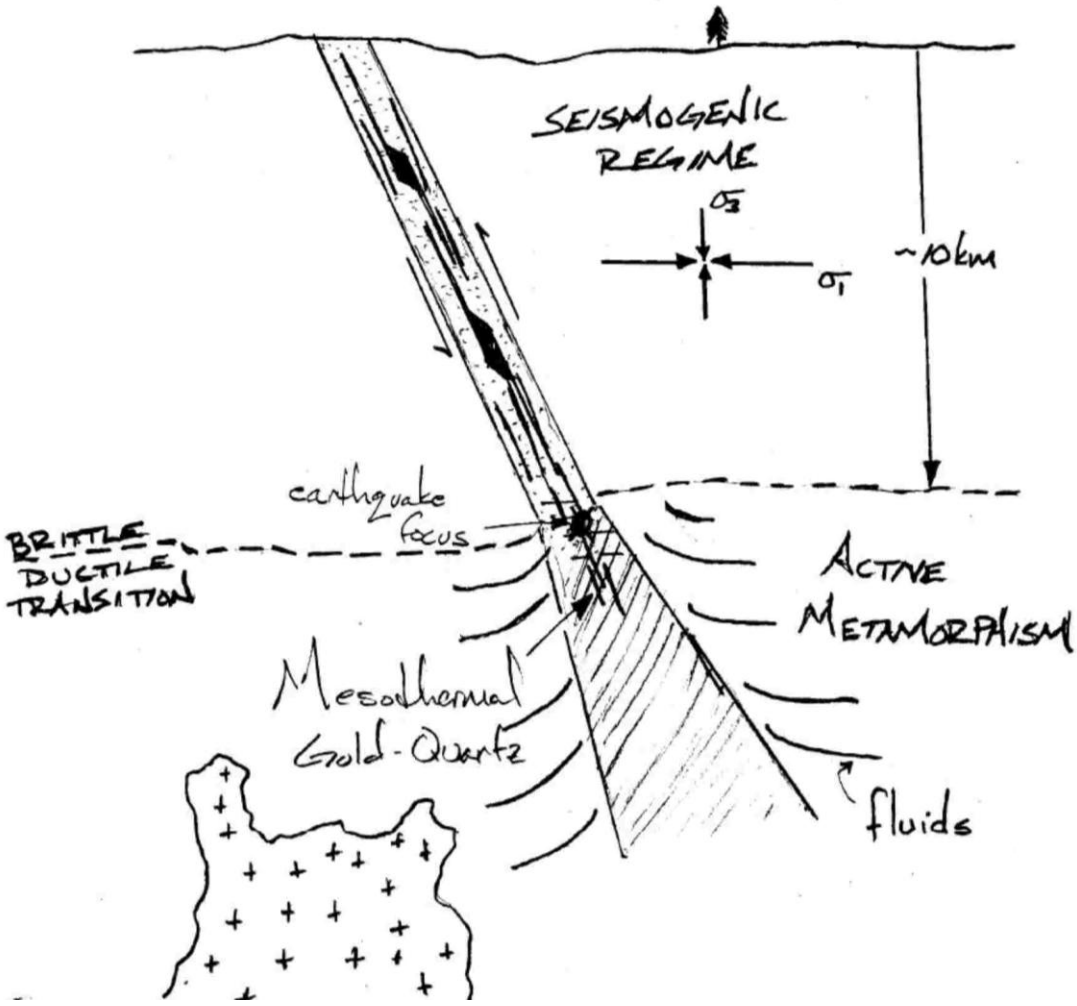

Figure 6: Synoptic diagram (not to scale) of inferred tectonic setting for mesothermal gold-quartz vein system in relation to continental seismogenic regime. Modified from Sibson 1988).

(Sibson, 2004). The carapace is an impermeable yet brittle membrane that seals off metamorphic or magmatic fluid generation processes, promoting an increase in P_F to near-lithostatic values thus allowing λ_v to approach unity. In a compressive regime with a horizontal maximum compressive stress (Figure 6), over-pressuring of fluids to near-lithostatic values ($\lambda_v \rightarrow 1$) may exceed the vertical minimum principal stress ($P_F > \sigma_3$;

tensile overpressure condition), or local rock strength, and cause hydraulic extension fracture meshes to form within the brittle carapace (Sibson, 2004). This seismic activity is accompanied by a sudden release of fluids and resulting drop in fluid pressure, which instigates immediate crystallization within veins and fractures. Within fault-fracture meshes hosting mesozonal Au-quartz lodes, the widespread distribution of extension and extensional-shear veins with crack-seal and open-spaced fill textures suggests local attainment of $P_F > \sigma_3$, allowing flow through gaping fractures (Sibson, 2004). The drop in fluid pressure (ΔP_F) and subsequent discharge through mesh structures across steep hydraulic gradients is a key factor to hydrothermal precipitation. Sudden drainage of over-pressured fluids during a seismic event precedes rapid mineral crystallization and hydrothermal self-sealing or self-healing, which reinstates the impermeable characteristic to the carapace allowing the cycle to repeat. The build-up of fluid pressure may happen suddenly in an episodic fashion on the time scale of seconds, or slowly increase over days, months, or years. Sibson (1988) termed the entire process of fluid pressure build up and sudden release along high-angle reverse faults as "fault-pressure-activated valves" (Figure 7). Both fluid pressure and shear stress build until an earthquake rupture event, at which point the "valve" releases fluids, dramatically decreasing pressure to hydrostatic (normal) levels. Inversely, mechanics of an epithermal environment operate concurrently at higher levels in the crust. Epithermal depositional mechanics differ in that slip transfer across dilational fault jogs during rupture propagation generates instantaneous negative-pressure, pulling fluids to shear zone center lines. Sibson (1988) called the negative fluid pressures from dilational jogs near the surface a *suction pump* effect.

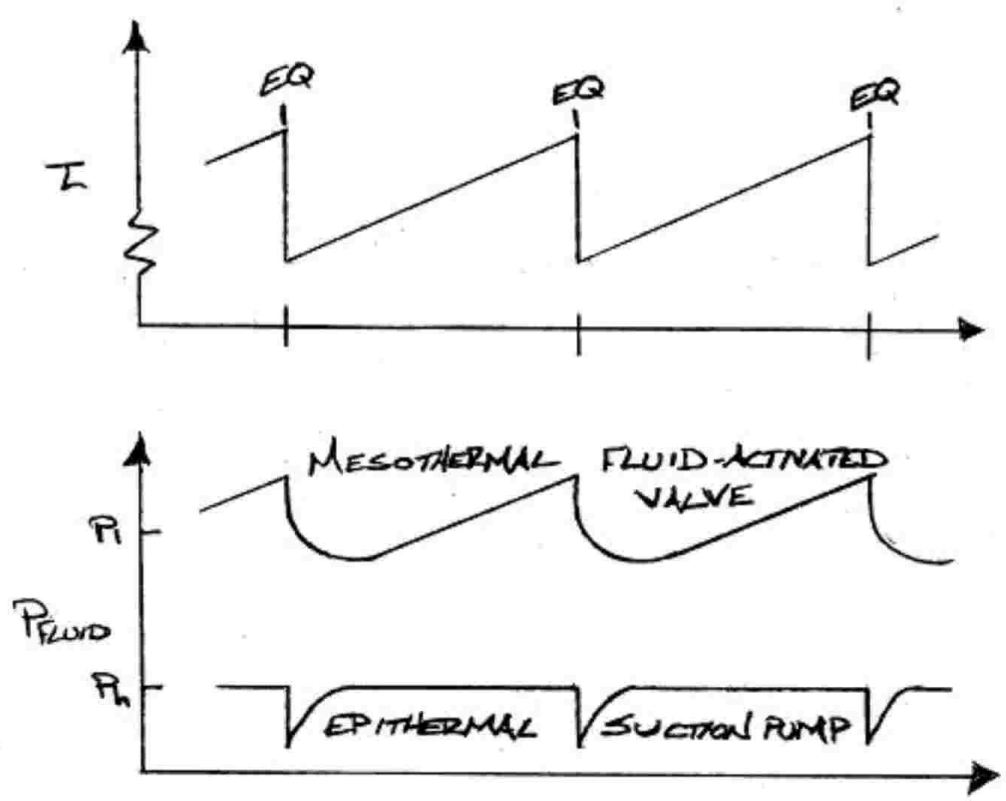

Figure 7: Inferred fluid-pressure (P_{FLUID}) fluctuations induced by valve and pump mechanisms in relation to successive earthquake rupturing episodes (EQ). τ is shear stress with respect to earthquake events. Notice sudden release of τ upon rupture. P_h and P_l represent hydrostatic and lithostatic fluid pressure, respectively. Modified from Sibson (1988).

2.2(b) *Compressional Setting*

Permeable, dilational areas within a low-permeability, contractional tectonic regime allow for focused discharge of upwardly advecting fluids. The episodic interaction of overpressured hydrothermal fluids at supralithostatic ($\lambda_v > 1.0$) values and surrounding crust occurs in conjunction with tensile or frictional shear failure (depending on the instantaneous differential stress) and the formation of extensional fractures or fault veins, respectively. Tensile fractures denote openings in rock that parallel the direction

of principal stress, whereas fault fractures are hybrid in that both opening and slip-shearing occur. Both tensile and fault fractures allow for mineral precipitation in newly created openings. As a consequence of displacement along new and optimally oriented faults and depressurization, syn-tectonic veins and extension fractures record episodic histories of deposition. Optimally oriented faults coincide with existing planes of weakness well-oriented for reactivation based on the Andersonian model of crustal behavior (see below), within otherwise intact rock. Fractures and faults provide structural pathways or conduits for focused fluid discharge in areas of fluid stress release, in the context of shortening and contracting crustal systems. Channelized, deep-seated fluids impregnated with gold or other precious metals deposit their load in local, massive lenses to extensional vein-fillings.

2.2(c) *Tensional Setting*

An important caveat to the fault model arises when mesh structures, opening veins, or fault veins occur in extensional tectonic regimes. The concept remains the same but principal stress axes change orientation. Maximum principal stress axis σ_1, now perpendicular to the horizontal ground surface in an environment of normal faulting and extension, fractures rock more efficiently by means of smaller differential stress (Figure 8). Dilatant extensional and extensional-shear fractures develop at sub-lithostatic fluid-pressure levels rather than the supralithostatic fluid pressures needed to create dilatant meshes in compressional regimes. Tertiary mineralization within the extensional Alaska-Juneau lode system serves as a popular example of this model. The lode system contains fault-veins developed along a system of normal faults interlinked by extension veins

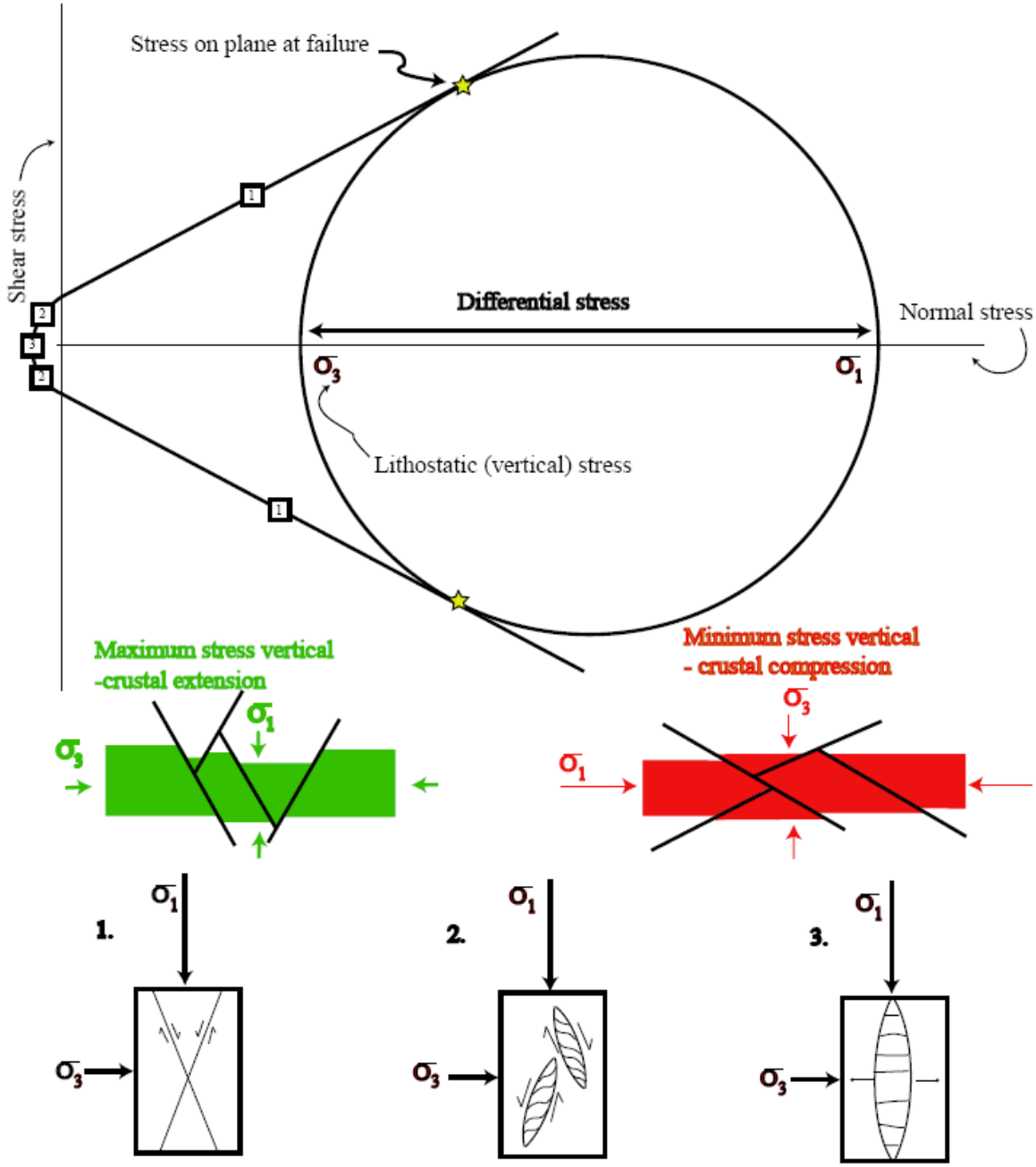

Figure 8 (previous page): Mohr-Coulomb fracture criterion for different states of stress, which highlights the magnitude of stress differential in crustal extension (thinning) and compression (thickening). Note the stress magnitude needed to cause reverse faulting in a compressive environment versus normal faulting in extension. Also shown are reality space diagrams for different failure conditions in the case of: 1) shear fractures with no dilation; 2) hybrid dilation fractures with oblique crystal fibers; and 3) dilation fracture with crystal fibers perpendicular to vein walls. Note shear sense on fractures oriented oblique to σ_1 in case 1 and 2. Intermediate principal stress axis, σ_2, is perpendicular to page for all diagrams.

preferentially concentrated within a high-competence folded gabbro layer set in a cleaved pelitic matrix (Miller et al., 1992). However, fluid overpressures take place more effectively in compressive tectonic regimes, and the potential for high amplitude fluid pressure cycling from fault-valve action increases.

2.2(d) *Transitional Setting*

The presence of through-going low-cohesion faults optimally oriented for frictional reactivation in the prevailing stress field inhibits all modes of brittle failure within intact rock (Sibson, 2004). Optimally oriented faults limit maximum overpressure for a given differential stress state, thus inhibiting a tensile overpressure condition ($P_F > \sigma_3$). Tectonic settings likely to develop mesozonal lode gold systems require the absence of through-going faults, which may occur in: 1) intact or metamorphically reconstituted crust; 2) faults with restored cohesive strength through cementation or sealing; 3) faults misoriented from inheritance (change in stress state); and 4) progressive rotational misorientation of faults or *domino steepening* (Sibson, 2004). The Anderson model of homogenous isotropic upper crust behavior states that fault planes represent Coulomb fractures, and as such they form parallel to the intermediate principal stress orientation (σ_2), and *c*. 30° from σ_1 (Figure 8). In a regime of tectonic constriction, low angle faults form, whereas in extension with vertical σ_1 ($\sigma_1 = \sigma_v$) and horizontal σ_3 ($\sigma_3 = \sigma_H$), high angle faults form. Changing regional stress state from thinning to thickening inherits a well-oriented set of faults for reactivation in an extensional environment, now severally misoriented in a constrictional regime. For example, domino-steepening of well-oriented

reverse faults during progressive shortening in a convergent plate margin will facilitate frictional lock-up, yet another favorable environment for mesh activation.

2.2.2 The Fault Model: Structural Environment

Epigenetic mesozonal lode-gold deposits occur within Archean granite greenstone terrains of Precambrian shields. Their affiliation to the brittle-ductile transition at the base of the seismogenic regime within shear zones and faults (Figure 6) is well known (Sibson, 1987; Goldfarb, 2005 ref. therein). Gold mineralization spatially associated with shear zones and faults in compressive/transpressive environments takes place in a predictable manner. Transpressive environments experience a deformational strain that is both coaxial and non-coaxial; flattening and shearing occur simultaneously. At the continental seismogenic zone, also called the brittle-ductile or seismic-aseismic transition, discontinuous and continuous shear zones exist in areas of crustal convergence and thickening. A transition in rheological behavior from brittle to ductile coincides with the strongest portion of the crust, which typically occurs at depths between 5 and 15 km, and is termed the load-bearing carapace. The position of this carapace fluctuates based on variations in geothermal gradient, host-rock lithology, fluid pressure, and strain rate, which also effect mineralization characteristics (see below). For quartz-dominant and feldspar-dominant lithologies, respectively, the crustal brittle-ductile transition corresponds approximately to isotherms at 300-350 °C and *c.* 450 °C (Figure 9), defining an undulating transition zone in the mid-crust with a relief on the order of 5-10 km (Sibson, 2007). Irregularities in topography within the seismic-aseismic transition establish rupture nucleation sites (Sibson, 2007) and most likely play a critical role in

focusing the discharge of overpressured metamorphic fluids. This may resemble a rug on a hardwood floor that wrinkles when pushed. Nucleation sites are located at the "wrinkles" in the carapace, which may account for the observed spacing of mesozonal deposits within transcrustal shear zones. The geographic or spatial distribution of gold lodes constitutes an important metallogenic characteristic (Goldfarb et al., 2005).

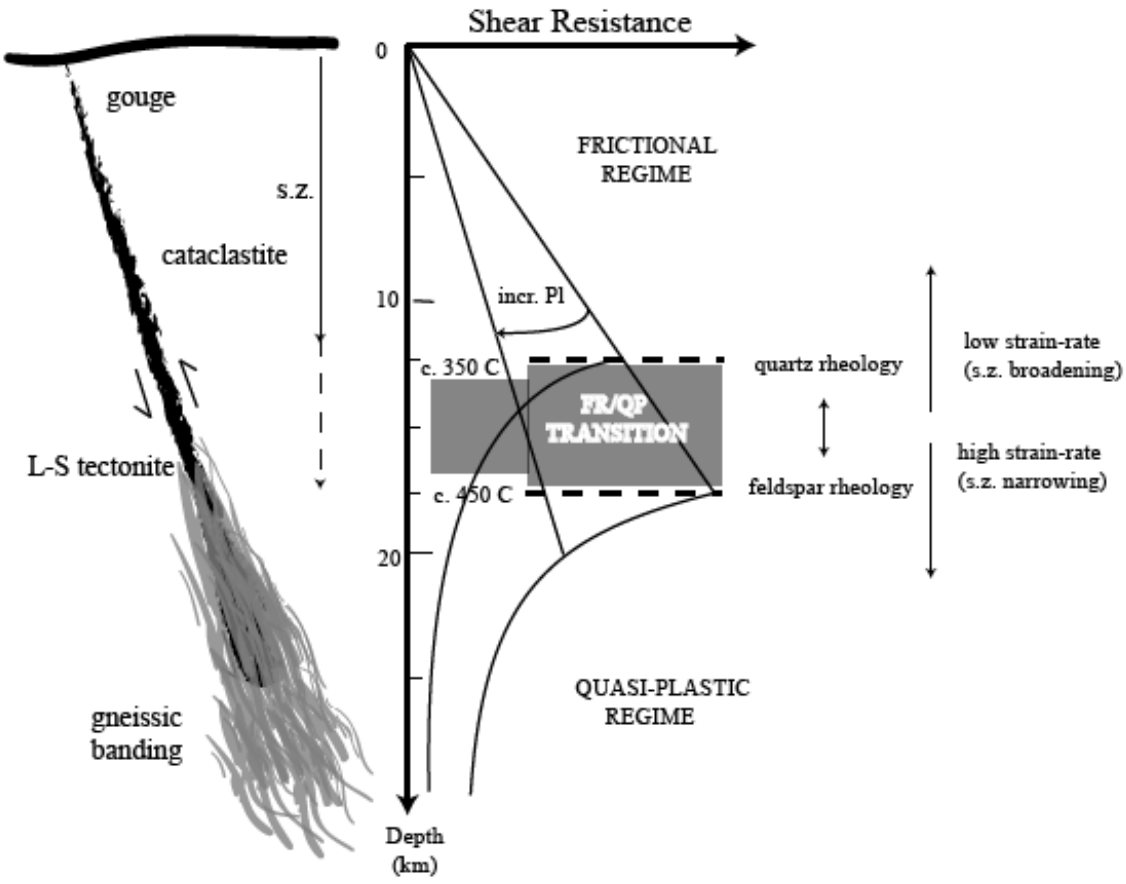

Figure 9: Schematic cross-section of transcrustal continental fault zone and related shear strength profile illustrating the effect of lithological and physical factors on the depth of the Frictional-Quasi Plastic (FR-QP) transition defining the base of the seismogenic zone (s.z.). Modified from Sibson (2007).

The mesozonal brittle-ductile style of mineralization comprises the central part of a continuum of styles over a crustal depth profile of 10-15 km (Groves et al., 1991). According to Groves (1991) the continuum develops as a product of an actively deforming convergent margin; portions thereof remain visible today after uplift and erosion. Three major segments delineated within the continuum of mineralization include deposits of many types. 1) epizonal, brittlely-dominated, sub-greenschist grade metamorphism within the first few kilometers of the crust overlies 2) mesozonal, brittle-ductile, greenschist grade, which overlies 3) hypozonal, ductilely-dominated, amphibolite grade at depth. Compiled from the characteristics of known Canadian Shield gold deposits the continuum represents a composite Archean gold system. Segmental change takes place in the style of mineralization and depositional mechanics with increasing depth; it does not imply a complete system developed at a particular location.

The majority of known gold deposits formed epigenetically (Colvine, 1989) so a close relationship likely exists between style of mineralization (i.e. epizonal, mesozonal, and hypozonal), metamorphic grade of wall rocks (i.e. sub-greenschist, greenschist, amphibolite), and crustal depth as terranes actively deform. Physical parameters dependent on crustal depth such as ambient pressure, fluid pressure, and geothermal gradient effect rheology, generating different styles of deformation, which in turn lead to different styles of fluid load deposition, summarized as follows:

- (< 6 km, 150°-300° C) Epizonal veining and brecciation result from slip transfer across dilational fault jogs during rupture propagation, causing negative fluid pressures and a suction pump effect. Metamorphic grade increases to sub-

greenschist in this environment while lode-style mineralization occurs within veins and breccias. Deposits of this type remain products of a pressure-dependent plasticity with little dependence on temperature or strain rate.

- (6-12 km, 300°-475° C) Mesozonal systematic veining occurs in the strongest portion of the crust at the brittle-ductile transition. Structural frameworks that host mineralization result from fluid pressures exceeding local rock strength, in a contracting or expanding tectonic regime. Middle to upper greenschist grades prevail throughout the mesozonal environment.

- (>12 km, > 475° C) Hypozonal foliation-parallel mineralization, although strain rate and temperature-dependent, has little dependence on pressure; rocks are too weak (ductile) to sustain mesh structures. Amphibolite facies lensoid to disseminated mineralization dominate in this ductile environment.

2.3 Alteration

Hydrothermal alteration associated with lode gold systems typically occurs 20 to 100 m.y. after sedimentation and marine volcanism (Schulz, 1980). Hydrothermal alteration haloes in wall rocks hosting mesothermal gold deposits reflect the interaction of an H_2O-CO_2-H_2S ($\pm CH_4$ and N_2) fluid with different rock types at various temperatures (e.g., Mikucki, 1997). Wall-rock alteration is largely controlled by the composition and competence of the host rocks and their metamorphic grade. In greenschist facies rocks, alteration presents itself through a variety of carbonate phases (mostly Fe-bearing including ankerite and ferruginous dolomite), sulfide minerals in the

form of pyrite (less commonly arsenopyrite), silicification, and alkali metasomatism that leads to the formation of sericite, biotite, albite, and chlorite. Alteration haloes near veins show enrichment in CO_2, K_2O, and S; leaching of Na_2O; and various amounts of chlorite and calcite away from the vein (Dube and Gosselin, 2007).

2.4 Fluids

Shear zones of mixed brittle-ductile character active within a sub-greenschist to mid-greenschist metamorphic environment host mesozonal Au-quartz lodes in fault-fracture meshes (200 Mpa < P < 400 Mpa and 250° C < T < 400° C: Ho, 1987; Roberts, 1987; Sibson and Scott, 1998). Epigenetic mesozonal gold deposits originate within vertically extensive structurally controlled hydrothermal systems as evidenced by: a) the association of universal mineral-bearing fluid species and isotopic characteristics (Mikucki, 1998); b) the extensive fluid-rock ratios within ore zones; c) systematic depth-dependent crystallization of quartz; and d) fluid leaching from wall rocks and intrusions.

2.4(a) *Fluid Composition and Source*

Gold concentration accompanies a distinct suite of elements (As, W, B, Mo, and Sb) stimulating correlations between fluid compositions. The distinctive elements and broad similarities in hydrous mineralizing fluid composition (generally, H_2O-CO_2-H_2S $\pm CH_4$ and N_2) at all temperatures give support to the 'crustal continuum' models, in which Archean lode-gold mineralization involved either a single fluid moving through the middle and upper crust, or a combination of ore fluids at different crustal levels (Figure 10). Although several gold models implicate a deep source, the origin of ore fluid

remains debatable. A number of deep fluid and solute reservoirs arise, including the basal segments of greenstone belts, mantle lithosphere, intrusive granitoid bodies, or subducted oceanic lithosphere (Colvine, 1989). Magmas crystallizing at mid-crustal depths may evolve low-salinity fluids; however, a potential problem is transfer throughout the crust at temperatures above the granite water-saturated solidus, without causing partial melting and incorporation of the fluid into a melt (e.g. Ridley 1990). Regardless of fluid source, induced boiling or phase separation of CO_2 resulting from sudden drops in fluid pressure seems likely an important mechanism for rapid fluid load precipitation (Sibson, 1988 and ref. therein). Fluid inclusion studies show that fluctuations in fluid pressure between lithostatic and lower values occurred during vein development. At the Sigma mine in the Val d'Or District of the Abitibi Greenstone Belt, interpretation of fluid inclusions indicate that three types of fluids resided during the development of quartz-tourmaline-carbonate veins: CO_2-rich, H_2O-CO_2, and H_2O-NaCl fluids (Robert et. al., 1995). Analysis of coexisting CO_2-rich and H_2O-NaCl fluids lead to the interpretation that variable degrees of intermittent unmixing occurred from a homogenous parent H_2O-CO_2 fluid of low salinity that infiltrated veins, which resulted from variations in fluid pressure.

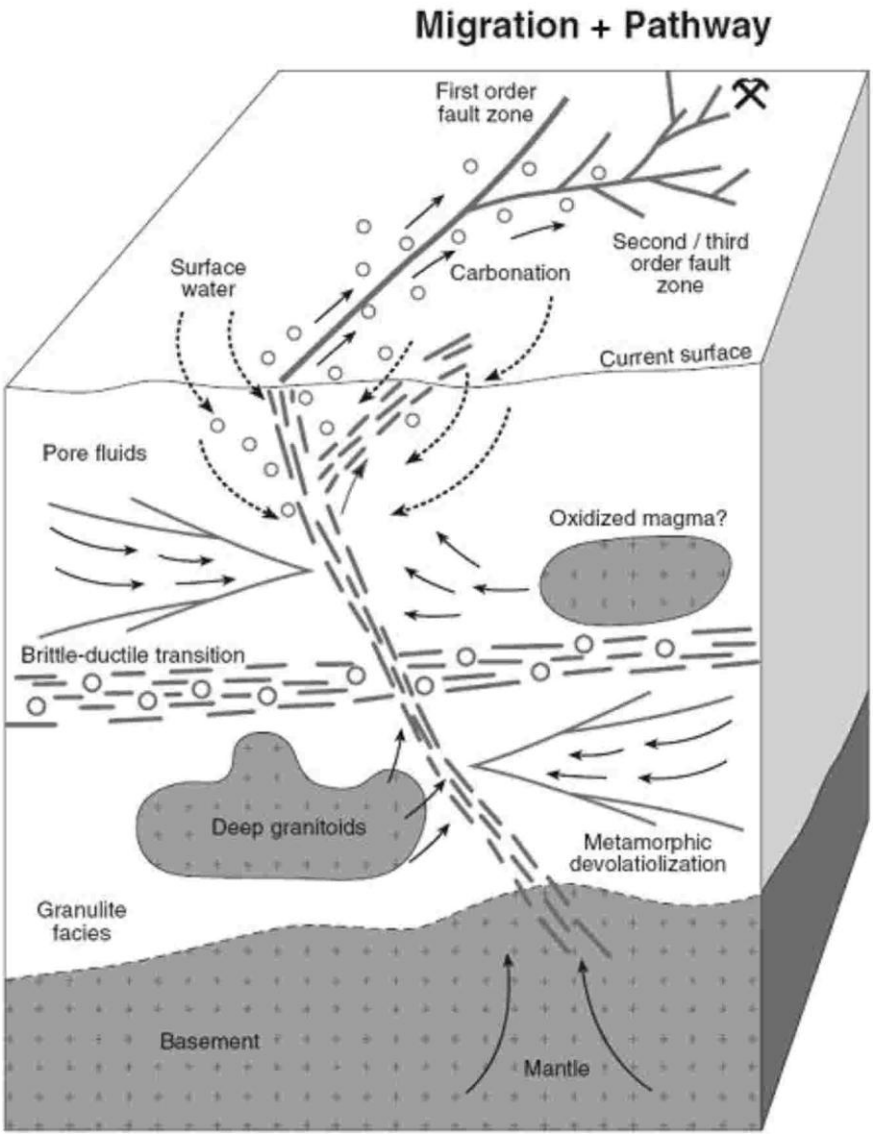

Figure 10: Permissive fluid sources for the formation of gold deposits in metamorphic terranes include meteoric, metamorphic, magmatic, and mantle reservoirs. Stable isotope data, however, generally rule out significant meteoric waters, and a variety of geochemical data are not consistent with fluid components derived from the mantle. Notice possible location of minable deposit in high-order splays of deformation zones. From Goldfarb (2005).

2.4(b) *Fluid-Rock Interaction*

Interaction of ore fluid with surrounding wall rocks is an essential part to any model of greenstone-hosted, mesothermal, shear-zone-related, lode gold deposits. High fluid-rock ratios become important to explain the elevated concentrations of gold and other minerals in a deposit. As an example, flow of ~1 km^3 of hydrothermal fluid could potentially give rise to a modest deposit containing ~10 tonnes of Au housed in a quartz ore-shoot occupying ~4 x 10^5 m^3 (e.g. a 1m x 400m x 1000m vein) carrying 10g/tonne (Seward, 1993). The production of high fluid volumes and flow rates clearly requires giant metamorphic or magmatic complexes.

2.4(c) *Quartz Vein Morphologies*

Quartz (SiO_2) is a ubiquitous vein component of all hydrothermal gold deposits (Vearncombe, 1993). A wide variety of vein morphologies present in outcrop can be used in the classification of hydrothermal deposits. A simplified scheme categorizes quartz vein morphology from gold deposits based on the growth direction of quartz in veins (Vearncombe, 1993). Although not associated with mineralization styles specifically, quartz vein morphologies might provide a record of crustal depth. The scale-independent categories of crystal growth include: 1) face-control (growing out from vein walls); 2) displacement-control (oblique to vein wall growth from shearing); 3) parallel-control (growth in different directions dependent on vein wall undulations); 4) radiating; 5) non-directional control (massive growth); 6) replacement; and 7) modified (later shear distorts original growth). Parallel and radiating textures characterize gold deposits formed at the near surface; displacement and non-directional control typify

deposits at mid-crustal depths (accompanied by greenschist to amphibolite conditions); and face-control shows a range of conditions from the near surface to mid-crustal levels. Replacement and modified textures embrace a wide variety of alteration and deformation conditions, and occur in gold deposits at all crustal levels.

2.4(d) *Fluid Leaching*

Study of unique fluid-rock interaction in the Yellowknife gold deposits, Northwest Territories, Canada revolutionized ideas in gold economic geology in the 1970s and 1980s. The principal contributor has been R. W. Boyle (1955, 1959, 1961, 1979) who developed evidence, in the face of considerable opposition at the time, that components of the ores were extracted or leached from the subjacent and laterally adjacent wall rocks in response to district-scale thermal-metamorphic gradients rather than "from an unknown intrusion at depth" (Guilbert and Park, 1986). Gold ore at Yellowknife is hosted in individual steeply dipping quartz-carbonate veins that crosscut their altered wall rocks. Boyle (1955, 1959, 1961; also see Guilbert and Park (1986)) noted that altered subjacent and laterally adjacent wall rock, that hosts mineralized veins, is low in quartz relative to background values in metamorphosed but unaltered greenstone lithologies—metabasalt, meta-andesite, and metadacite. Figure 11 is a plot of silica content across a typical composite alteration zone showing a "gull-wing" shape reflecting the presence of lowest silica values in the altered rocks on either side of the shear zone (Guilbert and Park, 1986). In lieu of the observation at Yellowknife, gold and silica anomalies associated with quartz lenses and veins were attributed to the presence of a granodiorite intrusion. Boyle argued that the gull-wing curve represents abstraction of

silica from the walls rather than addition of silica from an intrusive source. He further postulated that the intrusion provided heat energy to drive off volatiles, which in turn migrated from the altered wall rocks toward the centerlines of shear zones where they precipitated their loads. Precipitation could not occur under normal stress conditions because the wall rock requires dilation. The manner in which precipitation occurs necessitates a fault-activated valve system coinciding with wall rock leaching.

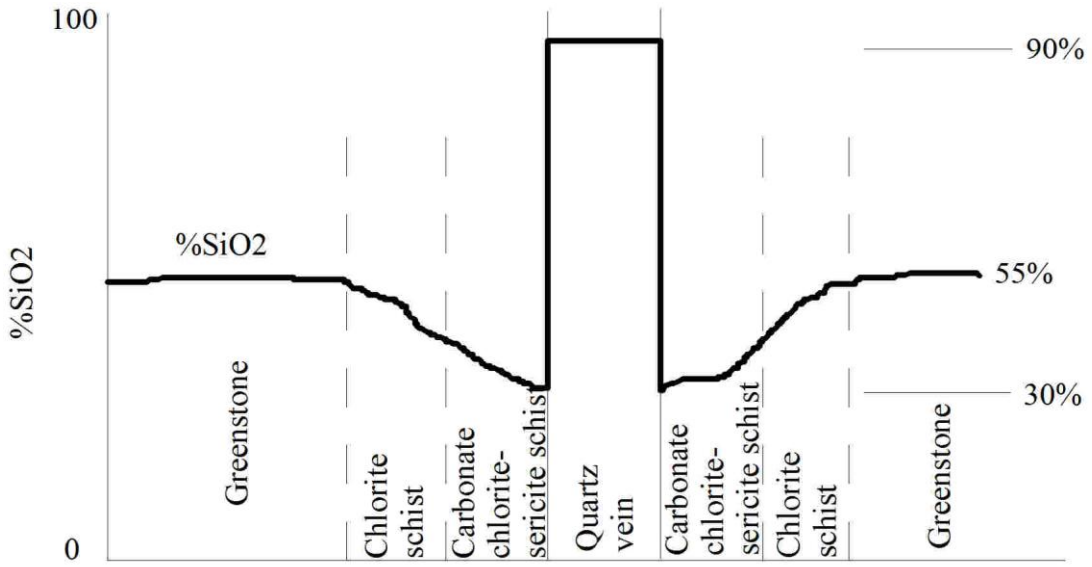

Figure 11: Percent SiO_2 profile across alteration zones adjacent to gold-bearing quartz veins. The profile suggests migration of SiO_2 from the altered walls toward and into present sites of quartz veins. Modified from Boyle (1955).

III. GEOLOGY OF THE MURRAY SHEAR ZONE

The geology, stratigraphy, lithology, structural history, and mineral potential within and surrounding the study area benefit from a rich history of mapping and study over the last 40 years (Sims et al., 1968; Ojakangas, 1972; Sims, 1972; Sims, 1973; Sims, 1976; Ojakangas, et al., 1978; Schulz, 1980; Sims and Southwick, 1980; Sims, 1985; Sims and Southwick, 1985; Southwick, 1985; Peterson and Jirsa,1999(a); Peterson and Jirsa, 1999(b); Jirsa et al., 2001; Peterson, 2001; Hudak et al., 2002; Jirsa and Boerboom, 2003; Peterson and Patelke, 2003; Hudak et al., 2004; Hudak et al., 2006; Hoffman, 2007; Ericksen, 2008; Goodman, 2008; Karberg, 2008). The Murray Shear Zone, as defined by this study, cuts an arcuate succession of rocks in the southern reaches of the western Vermilion District in northeastern Minnesota (Plate 1). Several attempts at dating various protoliths within the Vermilion District place the Murray Shear Zone in the late Archean (Jahn and Murthy, 1975; Boerboom and Zartman, 1993; Peterson et al., 2001). On the basis of gross lithology rocks cut by the Murray Shear Zone consist of: 1) Eagles Nest Basalts, Fivemile Lake Sequence, and Central Basalts of the Lower Member of Ely Greenstone; 2) the Soudan Iron Formation; 3) felsic volcanic and clastic sedimentary rocks of the Vermilion Formation; and 4) intrusive rocks (felsic porphyries, granodiorite, diorite, gabbro, and lamprophyre). Distinct curvilinear zones of schist with variable proportions of quartz, chlorite, sericite, ankerite, green mica, and pyrite exist in a variety of lithologies throughout the study area. Schistose rocks characterize the shear zone as they contain discrete evidence of deformation events. Rocks affected by the Murray Shear Zone are tholeiitic to calc-alkalic volcanic rocks of the Upper Ely Member,

and mafic volcanic rocks of the Knife Lake Group and Newton Lake Formation (Figure 12).

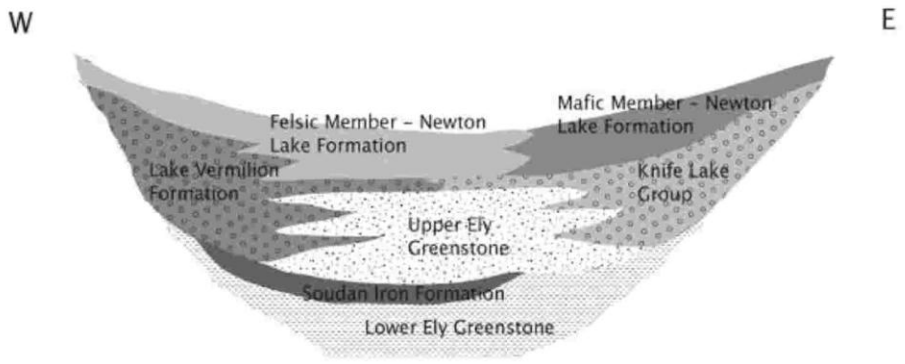

Figure 12: Vermilion greenstone belt cross-section cartoon shows reconstructed stratigraphic relationships, pre-folding, and faulting (After Schultz, 1980; From Goodman, 2008).

1. Lithology

Previous workers (Peterson, 2001; Peterson and Jirsa, 1999a; Hudak et al., 2002a; Hudak et al., 2002b) classified the bedrock geology within the study area using properties such as composition, texture, and color. This study uses the rock classification system of the previously cited works, and the map unit code nomenclature of Peterson and Patelke (2003). For a more detailed narrative on the historical development of the coding of lithologic units and descriptions see Peterson and Patelke (2003), and for additional detailed descriptions of each lithologic unit see Hoffman (2007).

The Lower Member of the Ely Greenstone consists primarily of greenschist-facies metamorphosed mafic to intermediate amygdaloidal pillowed to massive lava flows,

tonalite, diabasic dikes, mafic to felsic volcaniclastic rocks, porphyries, intermediate to gabbroic intrusions, and lenses of iron formation (Schulz, 1980; Peterson and Jirsa, 1999(a); Peterson, 2001; Hudak et al., 2002; Peterson and Patelke, 2003). The Soudan Member separates the upper and lower members of the Ely Greenstone. The Soudan Member comprises iron formation consisting of alternating layers of chert, magnetite, hematite, and jaspelite, with varying proportions of interbedded volcanic strata, transitional with volcanic units in the Lower Member of the Ely Greenstone (Jirsa and Boerboom, 2003). Lake Vermilion Formation rocks are mostly greenschist facies interbedded strata that vary, and locally grade, from felsic (calc-alkalic) volcaniclastic rocks, through rocks having evidence of variable reworking to mixed-source greywacke (Jirsa and Boerboom, 2003).

2. Structure

The Murray Shear Zone is one of several steeply-dipping broadly east-west striking shear zones in the Vermilion District (Figure 13). The 19 km long shear zone narrows eastwardly from 4 km to 0.4 km in width (Plate 1). Extents of the Murray Shear Zone determined for this study are constrained at the map scale by swamp and lowlands over Eagles Nest Basalt to the south, massive rocks of the Central Basalt and Fivemile Lake Sequences to the north, Giants Range Batholith and intrusive rocks to the east, and tuffaceous greywacke of the Vermilion Formation to the west. At its eastern extent, the shear zone cuts Eagles Nest Basalt and the tonalitic Purvis Pluton. To the east, the Giants Range Batholith most likely truncates the shear zone with distinct intrusions and phases

emplaced both during and after the Murray Shear Zone deformational event (Jirsa and Boerboom, 2003).

Mapping conducted by Peterson and Patelke (2003) for the National Underground Science and Engineering Laboratory (NUSEL) report recorded structural measurements in portions of the study area (Figure 3a). These data allow for comparison with recent field data collected for investigation of the Murray Shear Zone. Structural measurements in the vicinity of the Murray Shear Zone include 86 foliations and 22 linear features consisting of both mineral lineations and intersection lineations (Figure 3b). Average foliation interpreted from their data shows a strike of 275° and dip of 95°N. Lineations plunge consistently and steeply east and include both mineral and intersection lineations, plotted as one suite. Previous interpretations consider these lineations to have formed as a result of oblique strike-slip displacement, postulated to be responsible for the Murray Shear Zone architecture as seen today.

Peterson and Patelke (2003) identified the Murray Shear Zone as an east-west trending, dextral, wedge-shaped panel. They divided the Murray region into four main structural domains that include: 1) the Murray Shear Zone; 2) the Mine Trend Shear Zone; 3) the Linking Zone; and 4) the Collapsed Hinge Zone. In the words of Peterson and Patelke (2003) these domains: *"... appear to be internally structurally coherent, and are separated from each other either by areas of relatively undeformed rocks or discrete sheared boundaries."* They hypothesized that: *"Major shearing that produced the Mud Creek…and related shear zones, e.g. the Murray Shear Zone in the Soudan Mine area, is attributed to the late stages of…dextral transpression."*

The Mud Creek and Murray shear zones have been interpreted regionally in the Vermilion District as zones of deformation and metamorphism formed during a 3-phase (D_1, D_2, and D_3) northeast-southwest directed transpression sequence within the Vermilion District (Jirsa and Boerboom, 2003), which involved regional N-S shortening (D_1) followed by E-W strike-slip shearing (D_2), followed by NW and NE directed faults (D_3).

This study of the Murray Shear Zone identified and recorded similar foliation and lineation data to that described by Peterson and Patelke (2003). Foliations dip steeply and strike nearly E-W. Lineations were not mixed together as $L_{mineral}$ and $L_{intersection}$ but rather contain only $L_{mineral}$, and show a similar steep plunge. However, this study includes macro- and microstructural observations, which lead to a new interpretation of the Murray Shear Zone. Structural data identify an architecture produced by flattening strain rather than strike-slip shearing. Heterogeneities from ductility contrasts in the host material play an important role in the anastomozing character of the Murray Shear Zone as described below. In addition, gold mineralization is likely to have occurred within a constrictional environment due to the interaction of high pressure mineralized fluid and surrounding lithology.

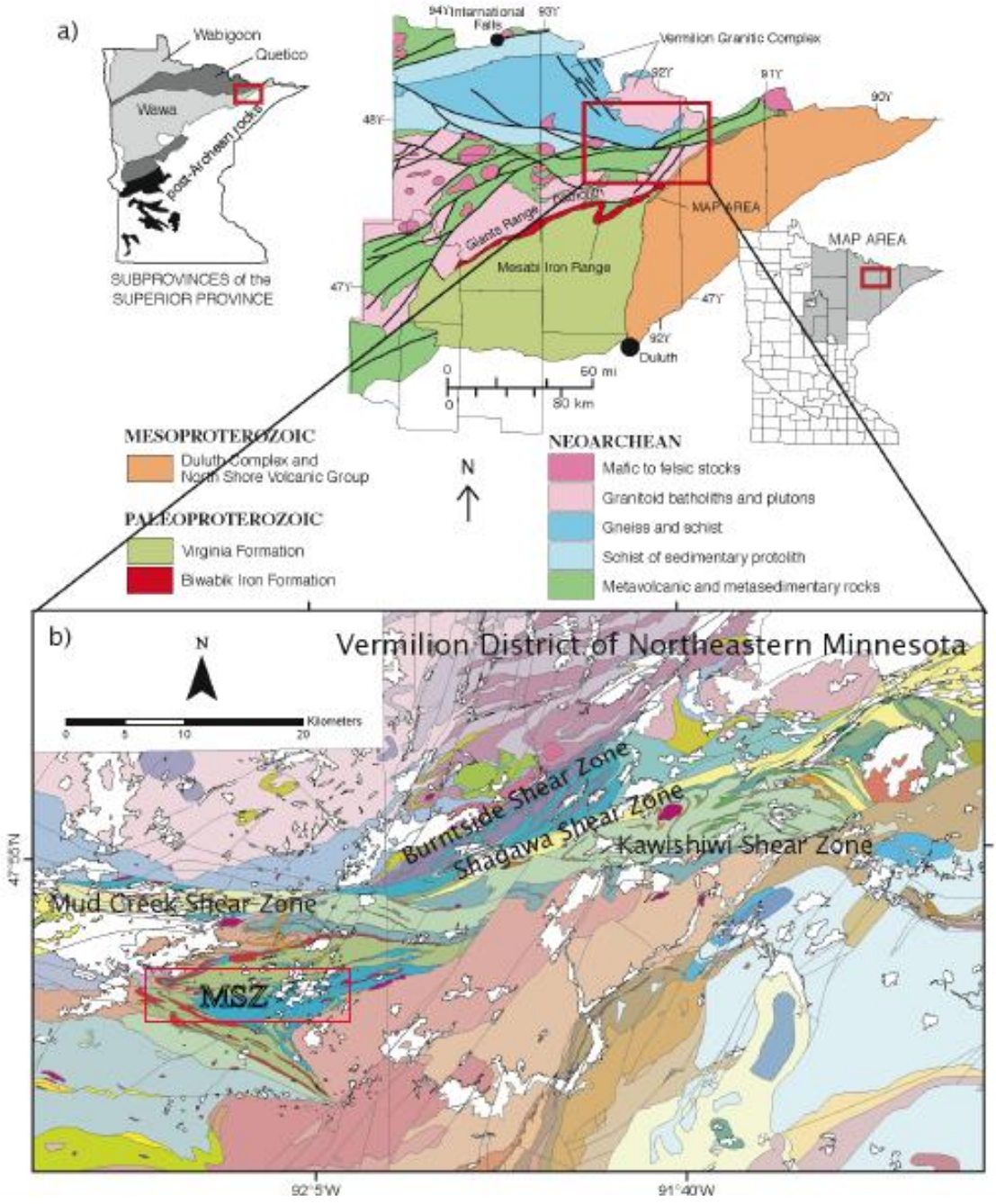

Figure 13: a) Generalized Minnesota Precambrian geology and Vermilion District location. b) Shear zones of the Vermilion District and location of the Murray Shear Zone (MSZ). Kawishiwi Shear Zone, Goodman, 2008; Shaqawa Lake Shear Zone, Ericksen, 2008; Mud Creek Shear Zone, Peterson, 2001 and Karberg, 2009. From Goodman, 2008.

3. Previous Gold Exploration

From 1988 to 1991, Newmont Mining Corporation conducted a drilling campaign after encouraging results from reconnaissance mapping and sampling of rocks, soil, and stream sediments in the northern edge of the Murray Shear Zone. The potential for gold culminated in a comprehensive exploration program that included eight drill holes, several meters of channel sampling, and soil sampling, reporting values up to 12.5 ppm gold (Robinson, 2005). Anomalous gold mineralization, associated with quartz-carbonate-pyrite-galena-tetrahedrite veins, and ankerite-sericite-green mica alteration, in strongly sheared and carbonatized rocks, ranged in the sub-500 ppb (parts per billion) and occasionally a few ppm (parts per million) (Newmont Exploration Limited, 1991). Newmont also found high gold values in chlorite-ankerite ± sericite schist, quartz veins, sheared mafic volcanic rocks, mafic-intermediate lapilli tuff, diorite intrusions, and chemical sedimentary rocks. Commonly, spikes in gold mineralization closely correlated with high levels of pyritization. Newmont's method of exploratory drilling utilized diagonal cross-stratigraphic holes in an effort to identify the gold-bearing lithology.

According to the work of Peterson and Patelke (2004), gold mineralization exposed at the surface parallels the orientations of linear structures in outcrop and is conformable with foliation. This observation coincides with the Newmont data; near-vertical foliation and steeply plunging lineation parameterize the structural situate for gold mineralization in the Murray Shear Zone.

(IV) RESULTS AND ANALYSIS

This investigation examines the structural architecture, crustal kinematics, and geochemistry of the Murray Shear Zone with implications for fluid distribution and gold mineralization. A first order investigation of structural architecture requires collecting data from accessible outcrop and procuring oriented hand samples. Thin sections prepared from oriented hand samples permit microstructural analysis. Microstructures within oriented thin sections allow for shear sense interpretations used to decipher local fabric asymmetry. Geochemical examination tests a suite of samples adjacent to mineralized veins for mobile and trace element behavior in hydrothermally altered wall rock.

Comprehensive investigation of the Murray Shear Zone entails: 1) structural mapping of 156 outcrops at a 1:5,000 scale; 2) collecting 135 oriented hand samples; 3) kinematic, petrographic, and alteration assemblage analysis of oriented thin sections from 41 oriented samples; and 4) geochemical analysis of 21 samples from three suites of rocks as defined by similar lithologic packages and proximity to quartz veins.

1. Field Data

1.1 Methods

Groundwork investigation of the Murray Shear Zone requires bedrock geologic mapping and sample collecting for laboratory analysis. Rock outcrop is sparse in northeastern Minnesota where thick forest and swamp are common. Due to poor exposure, mapping employed a cross section approach by utilizing perpendicular (N-S)

transects through the mainly E-W striking shear zone. Mapping perpendicular to strike placed attention on outcrops as a representation of varying degrees of strain measured from the shear zone centerline. A handheld global positioning system (GPS) device calculated NAD83 UTM coordinates at each outcrop. Table 2 is a summary of collected field data and outcrop locations.

1.2 Structural Fabric

Bedrock geologic mapping in the Murray Shear Zone defined inhomogeneous structural architecture that records both ductile and brittle strain environments. Architecture of the shear zone identified from field data shows structural fabric made up of: a) metamorphic foliation; b) elongation lineation; and c) dilational fractures. Ductile and brittle features present in outcrop provide clues to kinematic history, which I interpret within the context of the fault-valve model.

Structural fabric within the Murray Shear Zone is defined by steeply dipping planar elements. Mean-value metamorphic foliation (F_m) data show an average strike/dip of 272/80N (Figure 14). As defined herein, F_m constitutes discrete, continuous, penetrative planar elements within various protoliths of the shear zone. Typically, F_m is defined by aligned platy, granular, or elongate metamorphic minerals (chlorite, mica, epidote, actinolite, feldspar, and ankerite). F_m is secondary to primary depositional features such as bedding in sedimentary rock and modal, grain size, textural, phase, or combination layering of igneous rocks (Miller et al., 2002). A minimum bulk principal strain or maximum shortening axis, z, is interpreted perpendicular to foliation.

Steeply-dipping nearly E-W striking F_m pervades the host lithology as anastomozing schistose bands, or shear zones. Penetrative foliation is lacking in structurally coherent lithology bordered by narrow (cm to m scale) curvilinear shear zones. Anastomozing shear zones weave through massive mafic to felsic volcanic rocks, iron-formation, and clastic sedimentary rocks indiscriminately. Highly constricted F_m fabric within the narrow shear zones can be traced from outcrop to outcrop in smooth curvilinear trajectories varying 10-15 degrees along strike from an E-W direction. Foliation trajectories connect similar foliation orientations within the Murray Shear Zone, which have dip measurements that vary only slightly from vertical (10-15 degrees) (Plate1 and Figure 14). In this study, foliation trajectories are defined as the 2-D map projection of a 3-D planar (F_m) surface. NNW-trending F_m trajectories in the western portion of the study area cut regional fabric development at a higher angle of incidence. Map view also shows trajectories bordering offset stratigraphy in the west, which converge eastward from a curvilinear to a strongly linear belt. Interpreted strain partitioning appears to be the culprit of these map-scale features.

Mineral elongation lineations (L_e) characterize linear features within rocks of the Murray Shear Zone. L_e lies within F_m, plunging steeply at 090/68 (Figure 14). L_e are marked by chlorite, epidote, actinolite, tourmaline, and talc. The alignment of such minerals reveals a defined linear pattern that is visible in outcrop. In rare cases two suites of L_e are present in outcrop, both plunge steeply. L_e are interpreted as parallel to maximum bulk elongation strain—the x-axis of a strain ellipsoid.

Dilational and hybrid fractures filled with mineral precipitates typify brittle deformation features. Field inspection discloses quartz and calcite fractures that commonly cut F_m and L_e fabric at high angles (Figure 15a, b). Two suites of fractures strike NW-SE and dip NE and SW, respectively, with a dihedral angle of about 125°. The dihedral angle is the arc length between two fracture suites, measured within the plane that contains the poles of the two suites of fractures. Dilational fractures trend parallel to and open perpendicular to the maximum compressive stress axis, σ_1, or trend perpendicular to and open parallel to the minimum compressive stress axis, σ_3 (Figure 8). Infiltrating minerals precipitate rapidly with crystal fiber growth parallel to σ_3. Hybrid dilational fractures have an additional component of shear within a plane orthogonal to the opening direction. Orientations of crystal fibers with respect to fracture walls and orientations of opening fractures with respect to pre-existing structural fabric (e.g. F_m and L_e) allow for principal stress interpretations during the time of brittle failure.

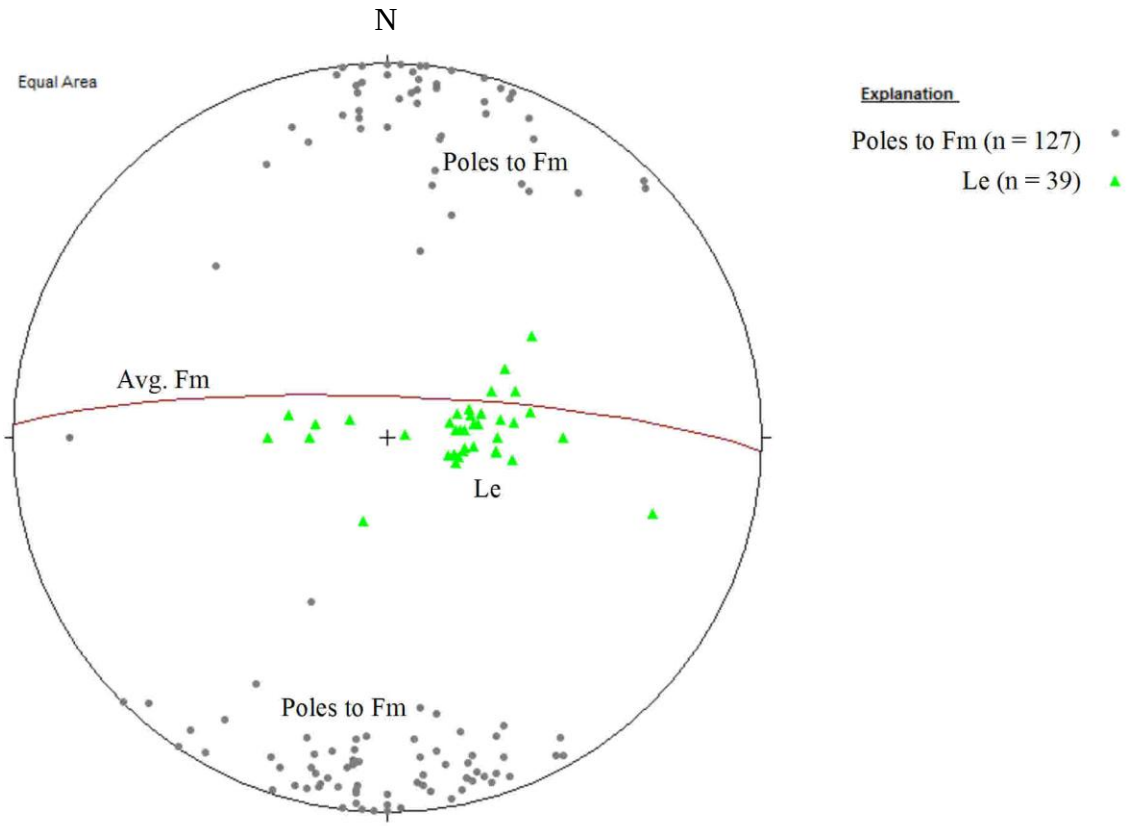

Figure 14: Foliation (F_m) and Lineation (L_e) data on equal area lower hemisphere projection. Average foliation plane shown. North points to top of page.

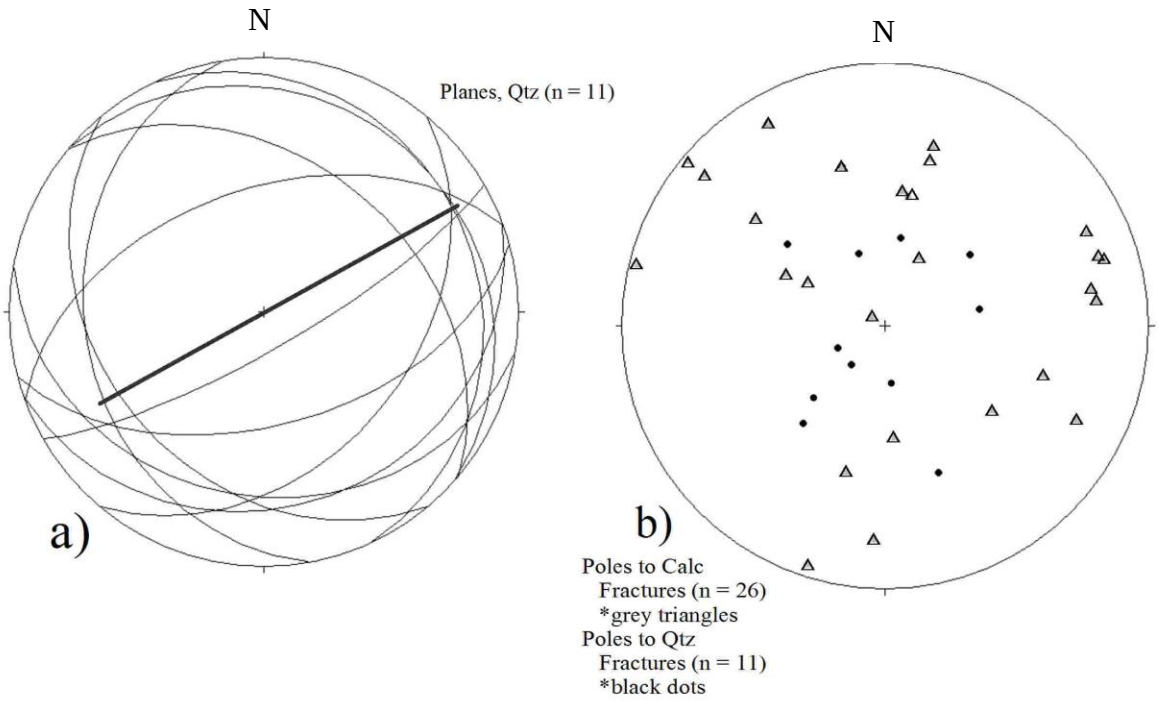

Figure 15: Equal area lower hemisphere projection. **a)** Fractures filled with quartz. All field data except outcrops M08-003, M08-029, M08-030, and M08-033. Note the arc length marked as a dark line between the two sets of fractures discussed in text. **b)** Poles to fractures filled with calc (all field data) and poles to qtz fractures. Qtz = quartz, Calc = calcite. North points to top of page.

1.3 Structural Analysis

Key field outcrops show common structural features that may help describe the Murray Shear Zone. Figure 16 is a cartoon block diagram showing the basic features in outcrop M08-033, a roadside outcrop along Hwy 169 north of Soudan, MN (Plate 1, Figure 3, red star B). The outcrop shows well-defined pillows on its top surface and a well-defined L_e (108/73) on the surface facing Hwy 169. F_m strikes 108/88 in the outcrop and is highly penetrative in a narrow margin at the road cut surface. Coherent pillows on the top surface of the outcrop exist within a meter from the road cut. The photograph in

Figure 16 is taken from Hwy 169 and shows F_m as slightly oblique to the exposed surface.

Asymmetric fabric within a motion plane describes a response to deformation (Figure 25). The motion plane lies normal to F_m and parallel to L_e (Passchier and Trouw, 2005). Orientation of the motion plane with respect to a vorticity axis allows for identification of shear sense. Vorticity, an axis of torque perpendicular to a shear couple, is usually normal to L_e. If L_e forms perpendicular to the vorticity axis, then L_e orientation delineates between dip-slip (steeply down-dip L_e), strike-slip (L_e near parallel to strike), or oblique slip (L_e between these two end members) shear. In rare cases the axis of vorticity is parallel to L_e resulting in a rolling lineation (Figure 17a). In this case, the plane normal to L_e should exhibit asymmetric fabrics, and evidence of rotation. Because asymmetries exist in the motion plane one would expect to find lineations either parallel with or perpendicular to that plane depending on vorticity. In other words, the mutual orientations of the motion plane, axes of vorticity, and lineations give rise to distinct 3 dimension structural analysis.

True strike-slip sub-horizontal shear would produce fabric asymmetries (e.g. S-C fabric, boudins, and porphyroblasts) in a (near) horizontal plane, perpendicular to Fm; in the case of the Murray, this horizontal plane preserves well-defined pillows, which represents a plane of symmetry rather than asymmetry. Therefore, the Murray cannot have experienced strike-slip shear deformation. In the case of the Murray, the motion plane lies parallel to, not normal to, L_e (as is typical); as such the motion plane is near vertical, normal to steep foliation and containing steeply plunging L_e. Put another way,

strike-slip shear would produce asymmetries (stretching or distortion) in the pillows of outcrop M08-030. Also, a penetrative foliation is not apparent in the plane of symmetry, as is shown in the cartoon diagram. The possibility exists that an entire block of relatively undeformed pillows is rheologically indifferent to deformation. Perhaps a silica-rich hydrothermal alteration hardened the outcrop and left a distinct rheological contrast to surrounding material.

In outcrops M08-006 and -007 L_e marked by tourmaline trend and plunge in a direction similar to L_e of M08-033 (106/76) (Figure 18). F_m strike and dip (106/83S) are also similar in orientation. A sub-horizontal surface in this outcrop does not show obvious asymmetries in the form of S-C fabric. In fact, the conspicuous linear elements signified by tourmaline crystals are manifested as rod ends in a sub-horizontal plane. The presence of tourmaline rod ends, in addition to elongated crystals in a vertical plane, may help identify the motion plane if lineations were created from rolling. A sub-horizontal motion plane in this case requires strike-slip shear and a vorticity axis that parallels the lineations. However, a sub-vertical motion plane is also plausible and explains the lack of asymmetry in the sub-horizontal surface. In the case of a sub-vertical motion plane lineations are formed from stretching. Figure 17b illustrates the case of L_e that are perpendicular to the motion plane while Figure 17c clarifies the location of symmetric and asymmetric fabric. Both block diagrams require a vorticity axis that is orthogonal to L_e and the motion plane.

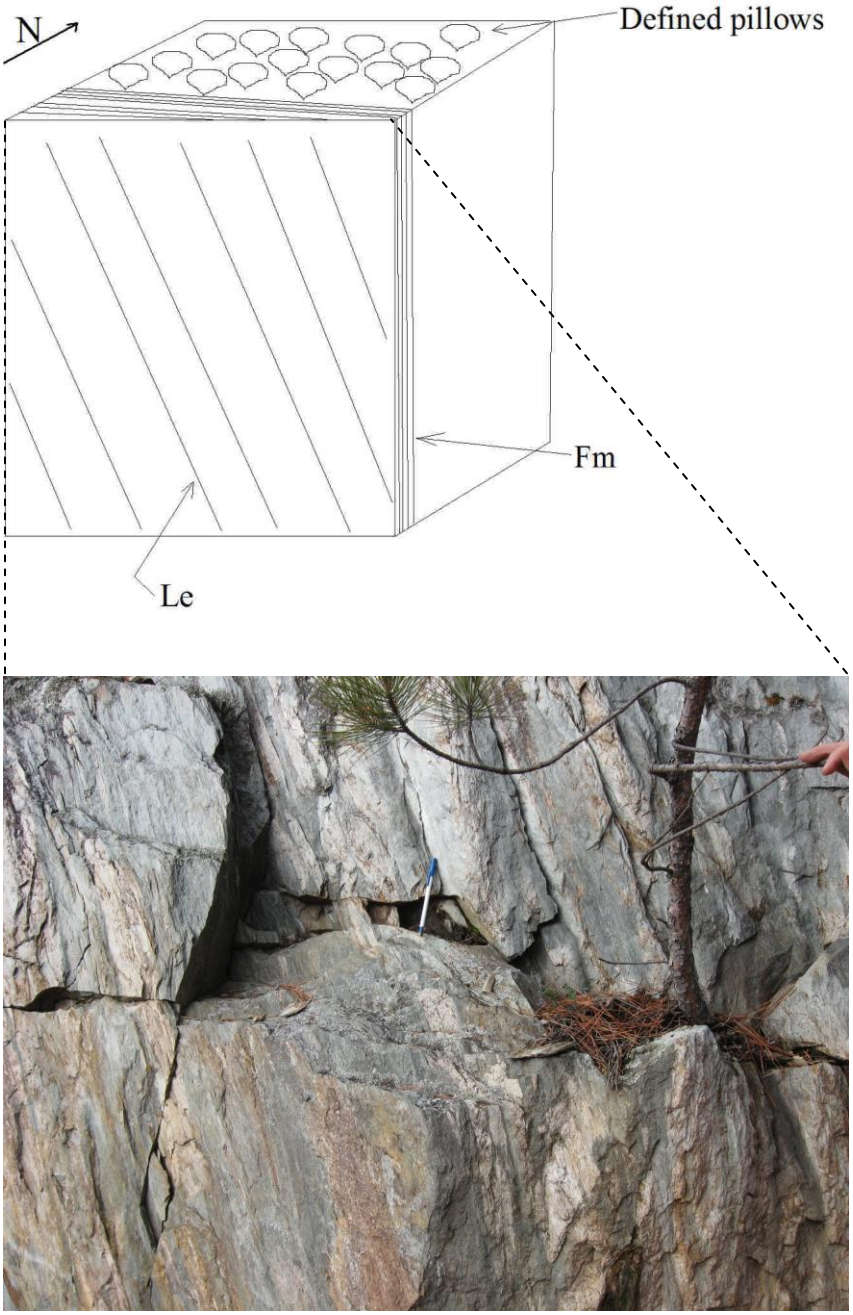

Figure 16: Block diagram of outcrop M08-033. Not to scale. Picture of south face showing strong L_e fabric that parallels F_m planes. F_m is constricted to the south margins of the outcrop and strikes oblique to the exposed face. Pen for scale.

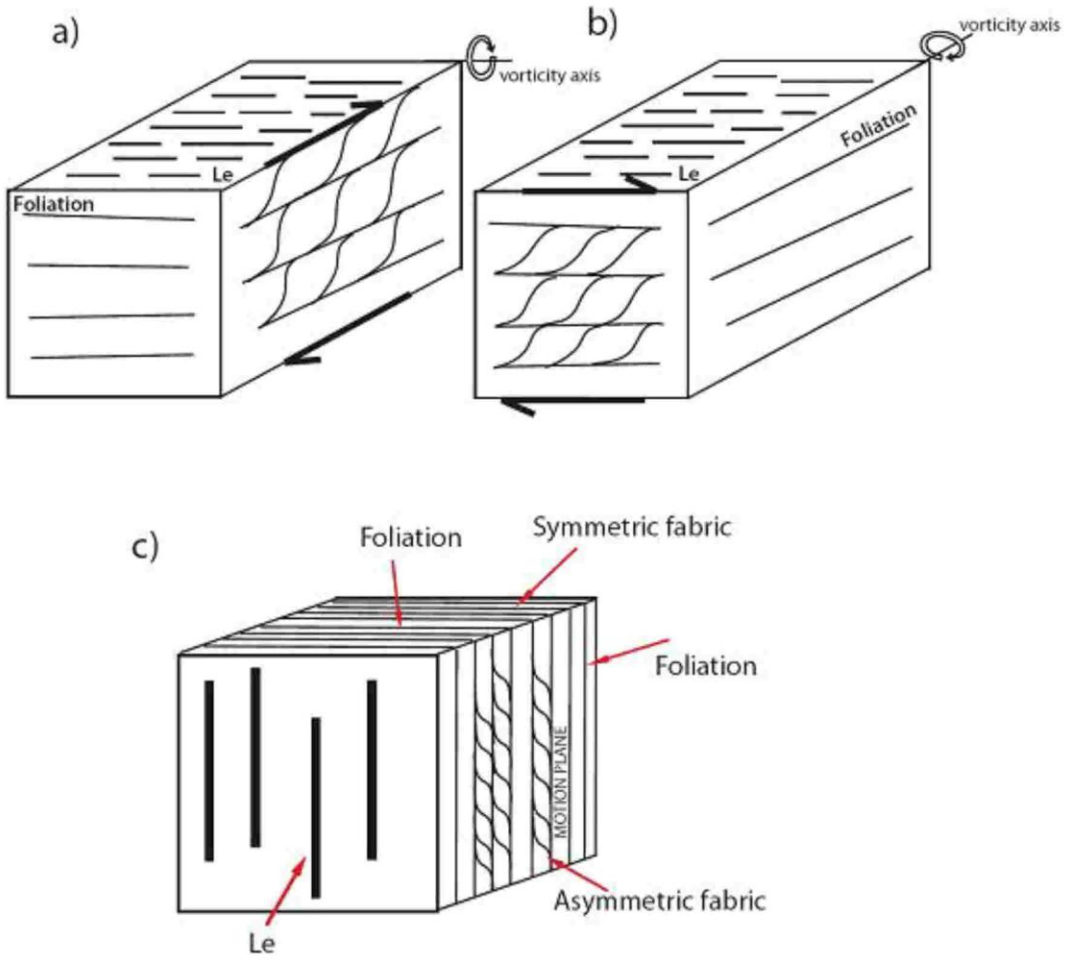

Figure 17: Schematic diagram of possible non-coaxial shear sense orientations. **a)** shear sense orientations with vorticity axis parallel to L_e; this is a rare case; **b)** shear sense orientations with vorticity axis perpendicular to L_e; **c)** Location of fabric asymmetry and motion plane for Murray Shear Zone L-S tectonites in reference to the L_e and the foliation plane based on microstructures. Modified from Ericksen (2008).

Figure 18: Field photograph of tourmaline-talc schist from outcrops M08-006 and -007. L_e trend and plunge in a direction similar to that of outcrop M08-033. Finger points to a vertical north-facing surface. Notice in top center of photograph a chipped sub-horizontal surface showing rod ends of tourmaline.

Four interesting cases of brittle over ductile deformation not included in the description above are discussed separately to emphasize observations of brittle-ductile behavior. All four outcrops below share similarities with respect to dilational quartz veins and orientations of F_m and L_e yet their differences prevent direct correlation. Outcrops M08-003, -029, -030, and -033 contain detectable gold in quartz veins (see discussion below). M08-003, -030, and -033 appear hydrothermally altered with sericite, carbonate, chlorite, green mica, and quartz. Outcrop M08-029, with low gold values around 2 parts per billion, experienced greenschist facies metamorphism, and lacks

evidence of hydrothermal alteration. F_m and the dilational quartz vein in M08-003 are sub-parallel, whereas outcrops M08-029, M08-030, and M08-033 have quartz veins that crosscut planar and linear elements at a high angle. Relationships between brittle and ductile features help to substantiate interpretations of the orientation of principal stress axes, which contributed to resulting strain recorded within the Murray Shear Zone. See figures 20 and 21 for the following discussion.

Outcrop M08-003

This outcrop contains the Murray Vein, which is a 10-15 cm-wide gold bearing quartz vein (275/86) (Plate 1, Figure 3, red star A). M08-003 is altered from a basalt protolith to ankerite + sericite + green mica schist. Penetrative F_m (275/85N) and L_e (rake: 120) present in outcrop signify a 20 m-wide zone of deformation (Figure 19a). Wall rock is only exposed to the north of the Murray Vein; the southern margin borders lowlands without outcrop exposure. A ptygmatic quartz vein deformed into a fold with an axis of 089/60 crosscuts a penetrative, nearly E-W F_m 15 m to the north of the Murray Vein. In Figure 20a, a field photograph shows a penetrative E-W foliation and a folded quartz vein. The mineralized quartz vein is 15 meters to the south of the location where this photograph was taken.

Interpretations of principal stress axes based on orientations of F_m and L_e follow a few simple rules relating to principle strain axes and dilational fractures: 1) the minimum bulk elongation or maximum bulk shortening Z-strain axis aligns perpendicular to F_m; 2) the maximum bulk elongation X-strain axis parallels L_e; and 3) the opening direction of dilational fractures parallels the minimum compressive stress axis, σ_3. In the case that

dilational fractures are normal to L_e, then the maximum bulk elongational strain (X) and the minimum compressive stress σ_3 parallel each other.

In the case of outcrop M08-003 a shortening or minimum bulk elongational strain direction should be perpendicular to both the orientation of F_m and the axial planes of the ptygmatic quartz vein. The vein fold axis parallels L_e and therefore could be related to the maximum elongation strain. Principal stress directions are not well confined using the dilational quartz vein only as a lack of fibers inhibits determination of minimum principal stress. However, thin laminar inclusions of wall rock or opaque minerals parallel to vein walls may signify an opening direction. Assuming laminar features present in the quartz vein represent episodic opening of the vein under high pressure fluid release, opening occurred orthogonal to the strike of the vein. Episodic high pressure fluid release is further exemplified in the dilational nature of the vein. Maximum bulk shortening strain, Z, inhibits dilational veining except in the case where fluid pressures approach lithostatic overburden pressures, thus necessitating fluid as a catalyst for fracturing.

Outcrop M08-029

A predicament arises while studying the large number of dilational quartz veins in outcrop M08-029 (Plate 1, Figure 3, red star D). Although many interesting deformational features are present, this location is likely underlain by iron formation surmised because a Brunton compass yields inconsistent readings. Regardless, structural data collected from outcrop M08-029 match other field observations although accuracy is

compromised. The structural data were measured at a 10 meter distance, where the supposed iron formation did not affect compass readings.

M08-029 appears to be a gabbro protolith that is bluish green to pale blue in color with 1-5 mm chlorite nodules. A weak planar fabric (095/75S) exists in outcrop M08-029. There is a dominance of brittle deformation features in this outcrop and paucity of highly penetrative F_m and L_e in comparison to other outcrop data. Slickenside lineations (L_s), marked by sub-horizontal millimeter-scale SSW fault striations, and right lateral offset signify a shear fracture (Figure 19b). One suite of dilational fractures strikes NNW and dips shallowly to the ENE; another suite strikes NNE and dips shallowly to the NW. A dihedral angle of 120° separates these suites, which are interpreted here as conjugate fracture sets. Quartz fibers that are slightly oblique to vein walls yet are parallel within the fracture suite further signify a conjugate fracture set. A third set of fractures strikes E-W and dips N. Quartz vein material in the third suite is generally massive with rims of quartz fibers perpendicular to vein walls (Figure 20b). Enclosed in all quartz veins are centimeter-scale chlorite-altered wall rock inclusions.

Hypothetically, maximum principal compressive stress, σ_1, would orient in a sub-horizontal NE line *ca.* 30 degrees from L_s (Figure 19b) as accounted for by dilational veins, shear fractures, and Mohr-Coulomb relationships (Figure 8). Minimum principal compressive stress, σ_3, could be any orientation within the group of poles to fractures in Figure 19b, which also correlate with quartz fibers and, thus, an opening direction.

Figure 20b shows a field photograph of a dilational quartz vein exposed in the southern road cut face of M08-029 (adjacent to Hwy 169). Notice the wall rock

inclusions and massive bulk quartz in the vein. Also, quartz fibers oriented perpendicular to vein walls can be seen in the central portion of the photograph. A later diagonal shear fracture crosscuts the host rock and quartz vein from lower right to upper left.

Outcrops M08-030

Formerly basalt, outcrop M08-030 is now altered to ankerite schist with extensive iron staining throughout (Plate 1, Figure 3, red star B). Maximum finite elongation strain, X, is aligned to L_e (rake: 117) while maximum finite shortening, Z, is perpendicular to F_m (270/85N). Two parallel dilational quartz veins (225/64N) crosscut F_m and L_e. Quartz vein fill is mostly massive with local crystal fibers marking an opening direction perpendicular to vein walls. Principal stress axes would be confined by and parallel to the orientation of quartz fibers in this case. The minimum principle compressive stress direction parallels the orientation of quartz fibers (Figure 19c). In this case, σ_3 would position in a NW sub-vertical direction.

A photomicrograph of a thin section oriented in the motion plane gives possible evidence of flattening in the direction of the maximum shortening Z-axis (Figure 20c). Foliation marked by chlorite, ankerite, and opaque minerals wraps around relatively undeformed rounded quartz crystals. Shear sense is difficult to determine in this particular section, although interpretation of another oriented thin section from this outcrop reveals sinistral shear based on sigmoid porphyroclasts of polygonal quartz crystals.

Outcrops M08-033

M08-033 is altered from a basalt protolith to sericite + ankerite schist (Plate 1, Figure 3, red star C). Principal strain axes parallel those in outcrops M08-003 and M08-030. Z is perpendicular to F_m (108/80S) and X parallels L_e (rake: 73); Y is unconstrained. Interpretation is wide-ranging with respect to maximum principal stress. Minimum principal stress was parallel to the crystal fibers (Figure 19d). M08-033 also contains defined pillows on the horizontal surface as discussed earlier, (not shown in Figure 19d for clarity). The quartz vein (136/30S) in this outcrop has similar appearance to opening veins of outcrop M08-029, including oriented quartz fibers perpendicular to vein walls, inclusions of wall rock, and a lack of hydrothermal alteration surrounding the vein.

Photomicrographs of a motion plane thin section display evidence of sinistral shear (Figure 20d). Grain Shape Preferred Orientations (GSPO) of quartz in a small hybrid dilational vein is highlighted in the accompanying sketch. Sinistral motion plane shear represents north-side-up, south-side-down displacement. Penetrative F_m in micro-section corresponds to flattening strain normal to Z and parallel to F_m in outcrop.

In summary, outcrops M08-003, -029, -030, and -033 possess brittle and ductile features providing evidence of deformational environments at the frictional-quasi plastic rheological transition. Interpretations of principal stress and strain axes are gleaned from brittle and ductile fabric in outcrop and micro section. An overarching interpretation is that N-S flattening in the region of the Murray Shear Zone produced anastomozing F_m and concomitant steep L_e in outcrop. Dilational quartz veins signify brittle deformation

under the influence of near lithostatic fluid pressures in a highly strained ductile environment.

Figure 19 (next page): Cartoon block diagrams illustrate salient brittle-ductile features and interpreted stress and strain orientations (with respect to an arbitrary coordinate system A,B, C) within four outcrops of the MSZ. Strain ellipses do not represent magnitude; they show orientations of maximum (X), intermediate (Y), and minimum (Z) elongation inferred from L_e and F_m. Likewise, stress axes do not represent magnitude. Principal stress axes are interpreted based on orientations of fractures and crystal fibers. In most cases maximum principal stress σ_1 is broadly constrained due to poor exposure of fractures. Narrowed constraint of minimum principal stress σ_3 orientation is based on crystal fibers within the fracture. **M08-003 (a):** Fold axis (089/60) of folded vein shown in dark blue signifying ductile deformation followed brittle deformation. V_f = vein fold axis in stereo plot. Mineralized dilational vein (285/76N) shows brittle deformation conforming to ductile fabric. Dark lines in vein parallel to vein walls may represent thin laminations of wall rock or platy minerals signifying episodic opening. **M08-029 (b):** Slight foliation in outcrop with lack of L_e as shown in grayed-out principal strain axes X and Y. Multiple dilational fractures, quartz fibers normal to wall rock, and slickenside lineations (L_s) confine σ_1 and σ_3. **M08-030 (c):** Broad constraint on σ_1 and specific constraint on σ_3 based on quartz fibers. Quartz vein (225/64N) carries low but detectable gold values. **M08-033 (d):** Similar constraints as outcrops M08-003 and M08-030. A quartz concentration (not shown) carries low but detectable gold. Defined pillows discussed earlier in text not shown.

Figure 19

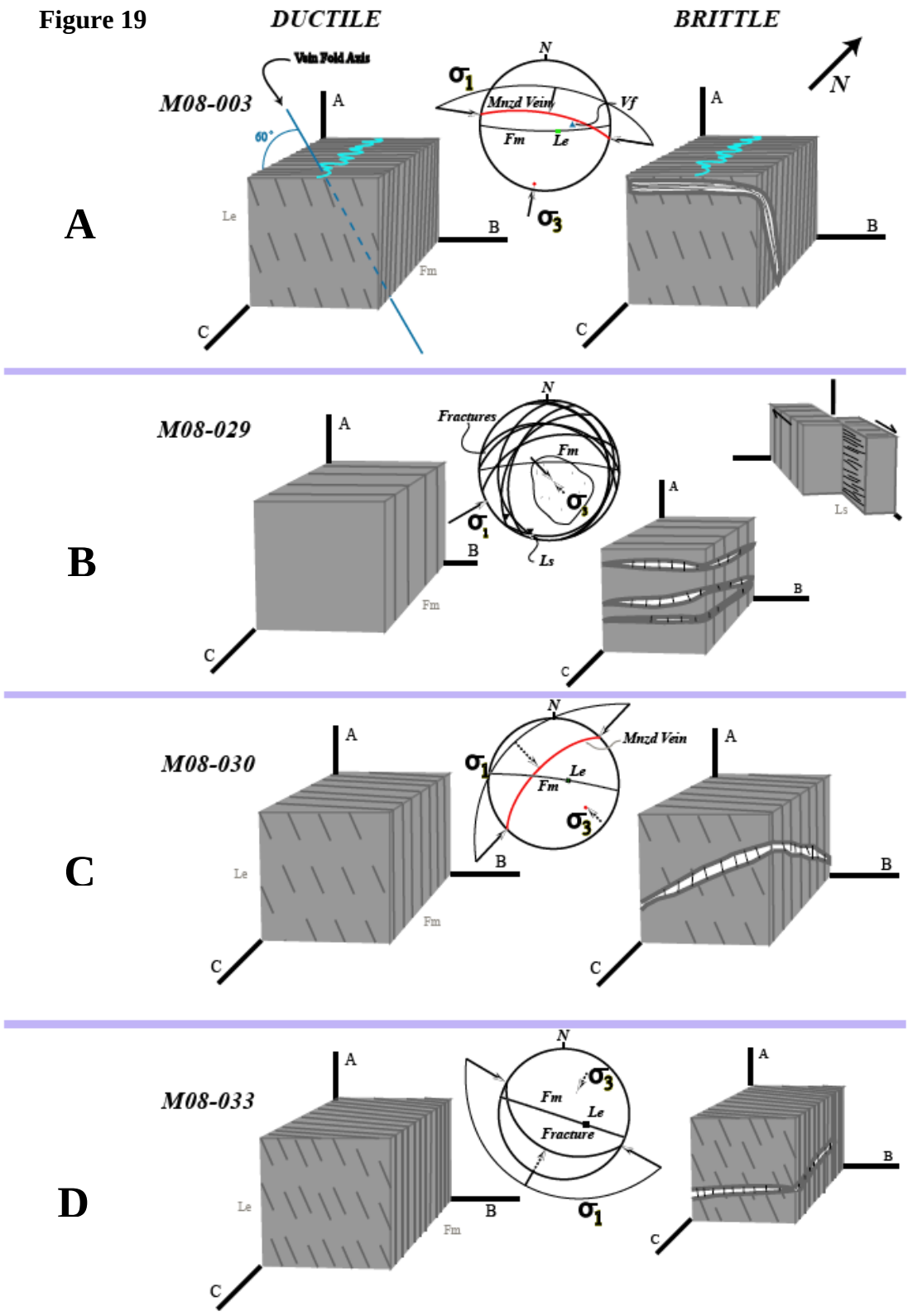
DUCTILE
BRITTLE
A
M08-003
Vein Fold Axis
60°
Le
Fm
B
C
N
σ1
Mnzd Vein
Vf
Fm
Le
σ3
B
M08-029
Fractures
Fm
σ1
Ls
Ls
B
M08-030
Mnzd Vein
σ1
Le
Fm
σ3
M08-033
σ3
Fm
Le
Fracture
σ1

Figure 20

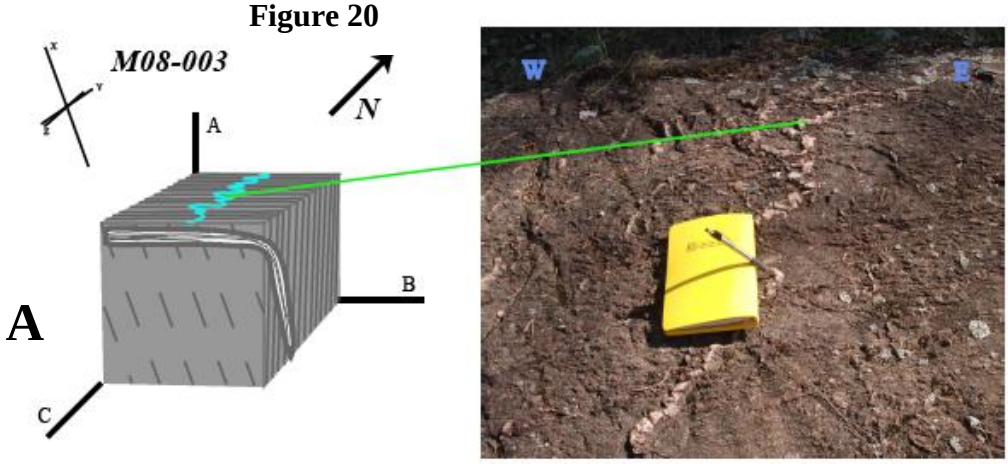
M08-003
N
A
B
C
A
W
E

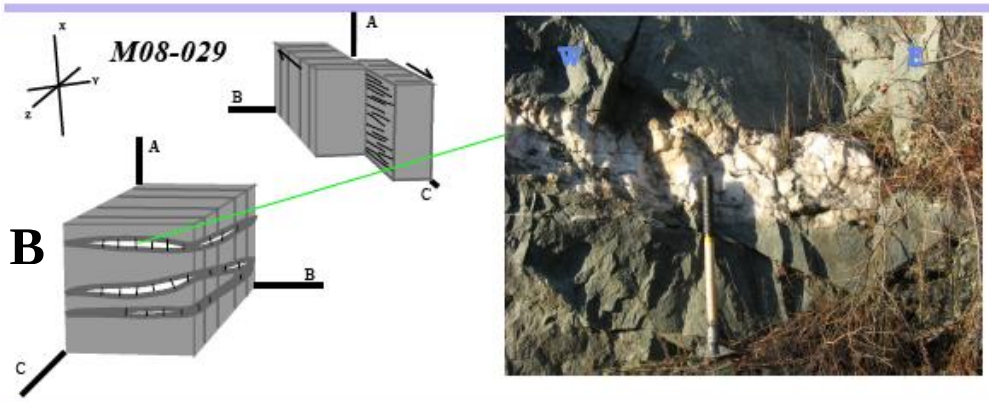
M08-029
A
B
C
B
A
B
C
W
E

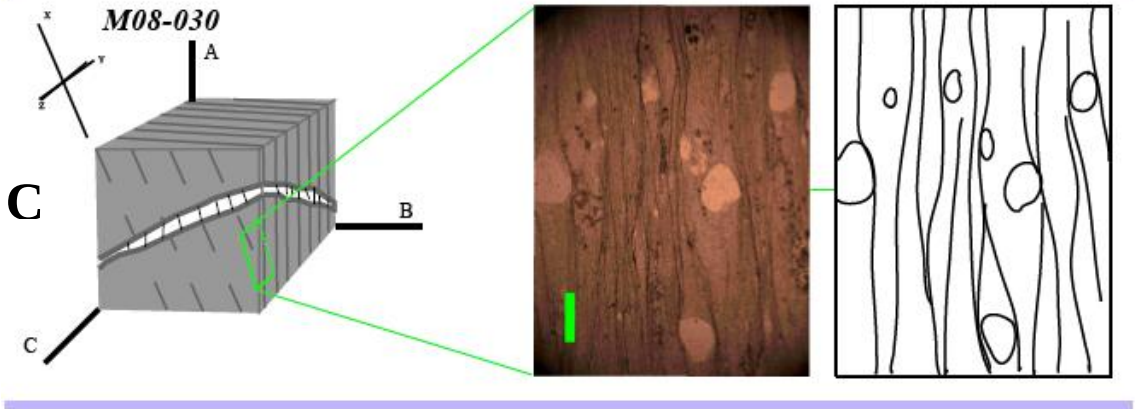
M08-030
A
B
C
C

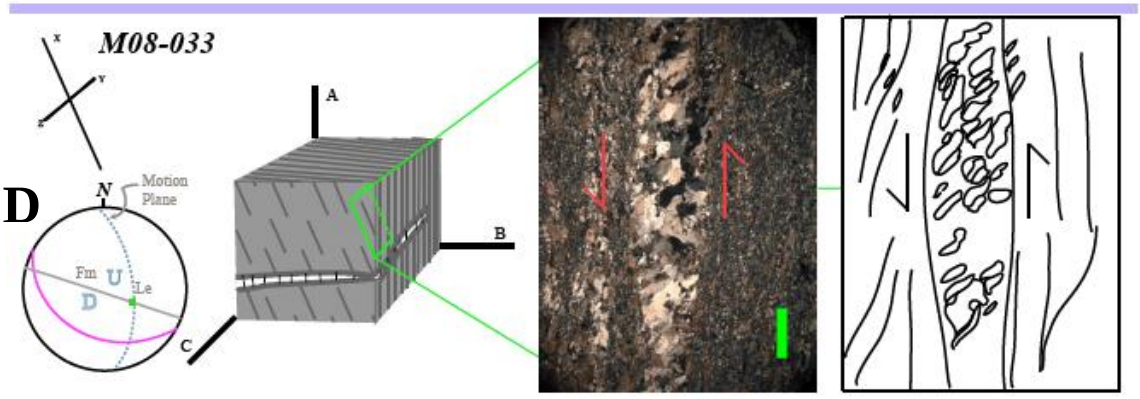
M08-033
A
B
C
D
N
Motion
Plane
Fm
U
D
Le

Figure 20 (previous page): Field photographs and photomicrographs of features present in outcrops of Figure 19. **M08-003 (a):** Folded quartz vein with pencil pointing in direction of fold axis. Penetrative foliation is difficult to see in this view. Folded quartz vein occurs 15 meters north of dilational mineralized vein. **M08-029 (b):** Dilational quartz vein with wall rock inclusions and thin laminar features of dark minerals parallel to vein walls. Note massive non-foliated appearance of greenstone wall rock. Veins are not mineralized with gold. View looking north, 50 cm hammer for scale. **M08-030 (c):** Photomicrograph (plane polarized light, scale bar = 1 mm) of carbonate-sericite schist with rounded quartz crystals. Motion plane view highlighted in sketch to right of photomicrograph. Note spaced penetrative foliation of chlorite, ankerite, and opaque minerals wraps around quartz crystals. **M08-033 (d):** Photomicrograph of hybrid dilational quartz vein showing quartz fiber GSPO (crossed nicols, scale bar = 1mm). Sketch to right of photomicrograph highlights interpreted sinistral shear, which represents dip-slip, north side up shear. See text for further discussion.

1.4 Hydrothermal Alteration Assemblages

Hydrothermal alteration results from a series of disequilibrium reactions between fluids and host rocks, commonly associated with seafloor hydrothermal systems and metamorphic or magmatic fluids. Hydrothermal alteration mineral assemblages relating to gold mineralization within the Murray Shear Zone can be used to guide exploration of Murray-type gold mineralization. Alteration envelopes that occur adjacent to mineralized white quartz veins progress from external metamorphosed but unaltered greenstone lithologies—metabasalt and meta-andesite—through outer alteration envelopes of chlorite schist, carbonate-chlorite schist, and carbonate-sericite ± green mica schist.

Rocks within the study area affected by greenschist metamorphism are characterized by concentrations of chlorite, ankerite, sericite, green and white mica, albite, actinolite, quartz, and epidote. Prior to the development of the Murray Shear Zone, regional quartz + epidote alteration occurred within Ely Greenstone Lower Member rocks (Peterson, 2001; Hudak et. al., 2002). This regional alteration was overprinted by three proximal alteration assemblages associated with the Murray Shear Zone gold mineralization: 1) chlorite schist; 2) carbonate-chlorite schist; and 3) carbonate-sericite ± green mica schist. Outcrop M08-003 shows envelopes of alteration adjacent to a mineralized quartz vein (Figure 21), and typifies what is believed to be the alteration envelopes, rock type, and gold potential of Murray-type mineralization. The outcrop is also used as an example for its geochemically similar protolith within 20 m of the *ca.* 7 ppm gold-bearing quartz vein.

The following rock descriptions of each alteration zone apply to rocks within the Murray Shear Zone. Descriptions are derived from observations made in both the field and laboratory.

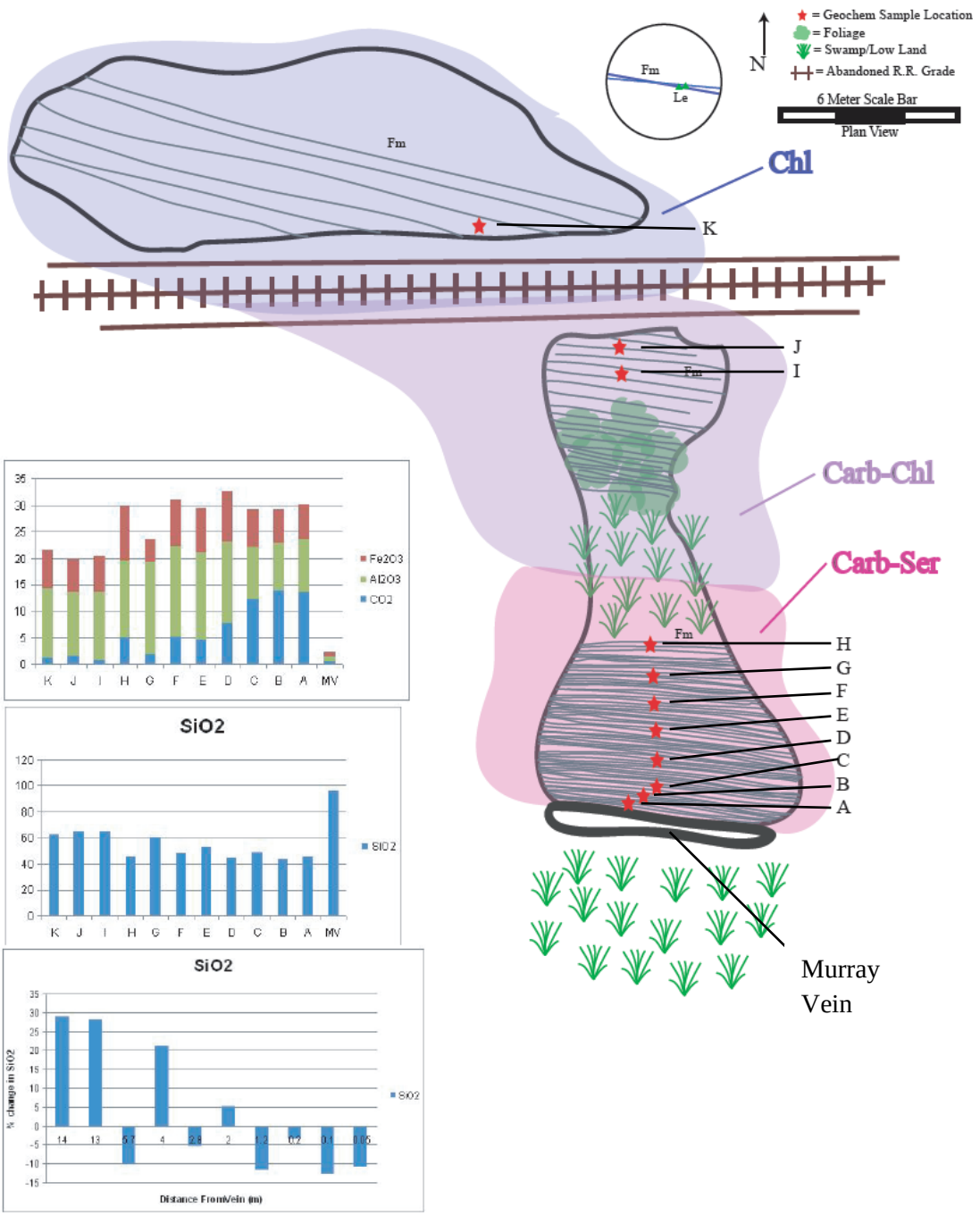

Figure 21: Cartoon diagram of outcrop M08-003 illustrating geochemical signatures, structural fabric, and alteration zones associated with a mineralized vein. Note degree of penetrative F_m close to the vein. Geochemical sample locations A-K are shown along with chart data. The top two charts display constituent concentrations. The bottom chart shows SiO_2 concentrations with respect to the isocon.

Chlorite Schist

Green to dark green very fine- to fine-grained, chloritic schists are generally composed of fine-grained chlorite folia anastomozing around small (1mm x 6mm) domains of more massive grains. The dominant protolith for the chloritic schists is pillow basalt and andesite flows. Weathered surfaces are commonly pock-marked with elongate pits aligned along the dominant foliation trend. Chlorite schist is the least penetratively foliated in a spectrum ranging from chlorite schist to carbonate-chlorite schist to carbonate-sericite schist.

Carbonate-Chlorite Schist

Strongly foliated and carbonatized rocks that contain an abundance of Fe-bearing carbonate (ankerite). These rocks occur in concentrated, well-foliated bands containing ankerite porphyroblasts in chlorite schist, and quartz vein-bearing brittle domains of nearly massive ankerite replacement of previously sheared schist. The carbonate-chlorite schists are believed to form from deep crustal CO_2-rich hydrothermal fluids channeled from depth within the Murray Shear Zone, and are analogous to carbonate alteration zones associated with mesothermal lode gold deposits.

Carbonate-Sericite ± green mica schist

Pale yellow-green to gray, very fine- to fine-grained schists that are highly foliated, siliceous, and iron-stained. Green mica occurs in nodules (5 x 2 mm) with a long axis parallel to L_e. Disseminations of pyrite are common within these rocks. Felsic volcanic or porphyritic felsic intrusive protolith for some zones of sericitic schist can be

locally interpreted. The carbonate-sericite ± green mica schists host gold-bearing quartz dilational veins and appear intensely foliated.

Locally intense quartz-epidote alteration and alkali metasomatism are prevalent in the study area (Griffin, 1967; Schulz, 1977; Peterson, 2001; Hudak et al., 2002; Hudak et al., 2005). Quartz-epidote alteration has been interpreted by Peterson (2001) and Hudak et. al. (2002) as synvolcanic in the Lower Member of the Ely Greenstone Formation.

Quartz-epidote alteration is a ubiquitous feature of massive sulfide deposits at and below the seafloor. Seafloor hydrothermal fluid circulates above a magmatic heat source and is capable of leaching and transporting metals and other elements. Widespread carbonatization, or carbonate alteration, and quartz-epidote alteration exists within the Murray Shear Zone, believed as evidence of hydrothermal fluid-rock interaction. Extensive carbonatization is associated with carbonate-rich metamorphic or magmatic fluids moving through host rocks during lode gold mineralization processes. Both carbonatization and quartz-epidote alteration are prominent in rocks surrounding the Murray Shear Zone as well (e.g. Fivemile Lake and Skeleton Lake; Hudak et al., 2002).

1.5 Hydrothermal Alteration and Au Mineralization

Geochemical data confirmed the presence of gold in quartz veins (Table 3). Samples of host lithology returned without detectable gold values. Most significant for gold mineralization is a 20 cm-thick quartz + sericite + ankerite + tetrahedrite + pyrite + green mica vein known as the Murray Vein (6.7 ppm gold, outcrop M08-003, sample MV), which crops out for 3 m and strikes 275°/86°N. The Murray Vein is abutted to the north by outcrop and to the south by swamp (Figure 21). Immediately adjacent to the

north is an alteration zone of ankerite + sericite + chlorite ± pyrite ± green mica in well foliated schist. Foliation is so penetrative at this location that collecting core samples proved difficult. The degree of alteration and foliation dissipate away from the vein such that 20 meters north is sufficient distance to reach moderately foliated, chloritized protolith. The F_m orientation remains consistent throughout the traverse except to the north where F_m strikes at a slightly higher angle (*ca.* 280°-285°).

Low but detectable gold values exist in other samples of quartz veins within the Murray Shear Zone, which include samples from outcrop M08-030 (3 ppb, CS-J-27), M08-033 (3 ppb, CS-I-22), and M08-029 (2 ppb, CS-H-17) (Table 3). Sample CS-J-27 from one of two parallel 5 cm-wide quartz veins in outcrop M08-030 contains gold. Sample CS-I-22 from outcrop M08-033 has gold in a 15 cm-wide quartz concentration. The presence of gold at the detectable limit of 2 ppb in sample CS-H-17 is found in 10 cm-wide dilational quartz veins.

Sample CS-H-17 from outcrop M08-029 appears to be a hydrothermally altered metagabbro lacking penetrative foliation. The alteration is greenschist grade metamorphism. Weathered surfaces are pot-marked with (1-3mm) chlorite nodules in a light gray to greenish blue rock. In addition to the lack of foliation, the alteration lacks ankerite and sericite mineral assemblages present in other outcrops of this study associated with gold mineralization.

Both locations M08-030 and M08-033 share similarities in the intensity of alteration and unique differences in structure to M08-003. Associated alteration of M08-030 in addition to silicification is ankerite + sericite + chlorite + mica. Chlorite makes up

a dark blue to dark green fine- to very fine-grained matrix. 20-25 % of the phyllite matrix is ankerite in 1-3 mm subhedral porphyroblasts. Sericite and white mica (talc?) are in wrinkled reddish pink to yellow foliations.

Alteration within M08-033 is albite + quartz ± epidote ± actinolite with disseminated sulfides near a 15 cm-wide quartz concentration (3 ppb gold). Outcrop surfaces on either side of, or immediately adjacent to, the vein show reddish-brown gossan staining. Wall rock hosting the mineralized quartz concentration is altered to chlorite + carbonate + green mica.

Qualitative rock hardness data was obtained while using a hammer to collect hand samples. Outcrop M08-030 seems rheologically hardest of all four comparative outcrops, whereas outcrop M08-003 is softest and most penetratively foliated. Rheology contrast may be due to the amount of silica alteration (remobilization?) experienced by the outcrop. However, the observation that the degree of penetrative foliation is directly related to softness is a contemporary one and may not hold true through its history.

Also in outcrop is a large patchy-white quartz-epidote-sericite-green mica alteration zone located several meters from the vein (Figure 22). At the Fivemile Lake area, Hudak and others (2002) define an alteration zone dominated by quartz + epidote-bearing mineral assemblages exhibiting mineralogical and geochemical characteristics of metal-depleted rocks found within deep parts of subaqueous convective hydrothermal cells. Murray associated alteration zones overprint the synvolcanic quartz + epidote ± actinolite ± chlorite assemblages. Early seafloor metasomatism during deposition of the volcanic pile and later mesothermal gold mineralization has similar metamorphic

characteristics, e.g. greenschist facies mineral assemblages, CO_2 and H_2O rich fluids, and 300°-475° C temperatures. Thus, difficulty arises in distinguishing between metamorphic events; overprinting relationships can be blurred from homogeneity of the systems.

Figure 22: Photograph of quartz-epidote zone (whitish area). 50 cm hammer for scale. Located in outcrop M08-033 along Hwy 169.

Another interesting alteration zone in the study area is the tourmaline-white mica (talc?) schist shown in Figure 18. Tourmaline rods and 2-5 cm white mica nodules (Figure 23) make for conspicuous secondary alteration features. Tourmaline can occur in trace amounts (generally < 1%) and is most commonly an accessory mineral in felsic volcanic or igneous rocks. Tourmaline commonly occurs in association with white micas

and iron carbonate minerals in shear zones that host anomalous mesothermal gold mineralization (Goldfarb, 2005). An over abundance of tourmaline in outcrop is apparent from the photograph in Figure 18 and Figure 23.

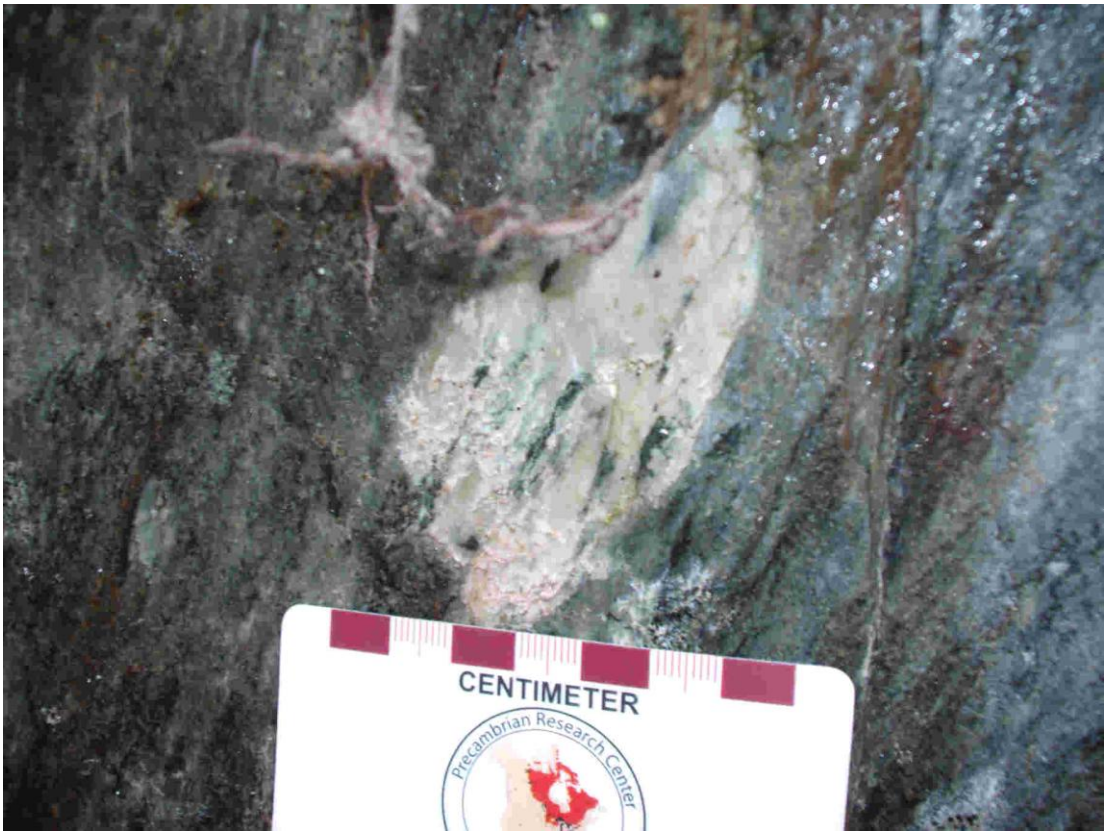

Figure 23: Talc nodule on same outcrop surface as in Figure 18.

2. Laboratory Data: Petrography and Microstructures

This section is a synopsis of petrographic and microstructural analysis. The aim of this section is to provide high resolution detail of data collected in the field. Petrographic and microstructural analysis utilizes a microscope to examine: 1) the description and classification of rocks; and 2) the internal structure and character of rocks, respectively.

2.1 Methods

In total, 41 oriented thin section billets cut from oriented samples were investigated to determine mineral assemblage, metamorphic grade, possible protoliths, microstructural fabric, and shear sense. Each thin section was cut parallel to the motion plane, perpendicular to foliation and parallel to lineation for kinematic analysis (Figure 24). Asymmetric microstructures which record shear include S-C fabric, mica mats, and rotated clasts with tails.

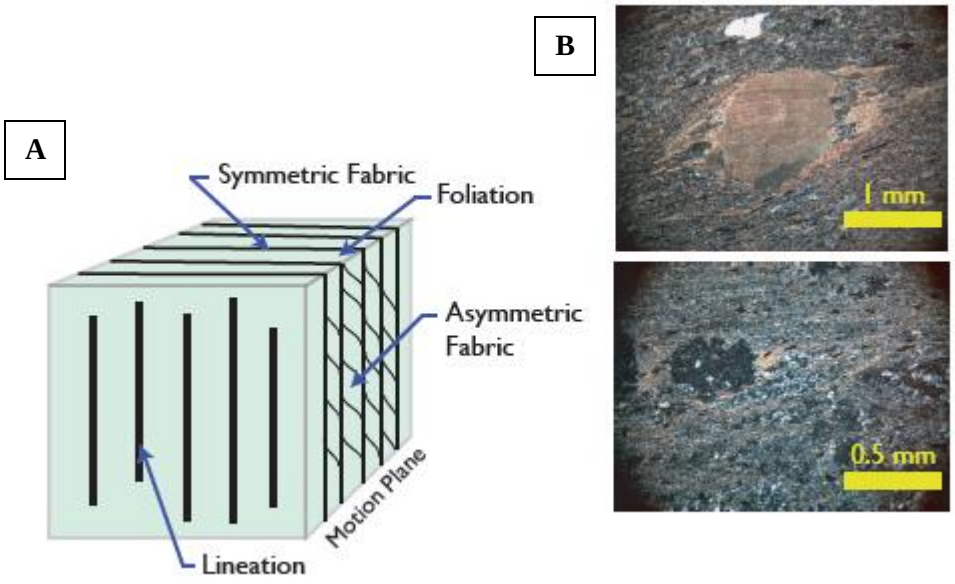

Figure 24: a) Block diagram illustrating a motion plane. **b)** Photomicrographs of kinematic indicator examples found in the motion plane, cross nicols. Top photo shows calcite porphyroblasts in a fine grained matrix of plagioclase and sericite, dextral sense of shear. Bottom photo shows calcite nodule in fine grained matrix of quartz and sericite, dextral sense of shear.

2.2 Petrography

Petrographic analysis was conducted to gain insight into metamorphic conditions that accompanied deformation. Petrographic work identified mineral assemblages, metamorphic facies, and possible protoliths by evaluating relative mineral abundances and alteration minerals (Table 1). Identification of some minerals proved difficult due to very fine grain sizes for the majority of thin sections. Protolith is generalized where no relict fabric was observed as both deformation and metamorphism obscured much of the original layering and grain boundaries.

Commonly occurring phases include typical greenschist minerals such as chlorite, quartz, epidote, actinolite, clinozoisite, plagioclase, muscovite, sericite, pyrite, and carbonate (ferrugenous dolomite, calcite, ankerite, and siderite). Most samples are chlorite and mica schist, although biotite schist occurs as well. Muscovite is rarely present as a primary mineral whereas its fine-grained equivalent sericite is common. Because of the fine-grained texture in the majority of thin sections sericite can easily be confused with fine grained actinolite. Very fine-grained feldspar appears similar to fine-grained quartz as well.

Mafic volcanic, lesser felsic volcanic, associated sedimentary rocks and iron-formation comprise the majority of protoliths. Potassium metasomatism produced the white mica, whereas chlorite and actinolite commonly derive from mafic volcanic rocks such as basaltic pillow lavas. Quartz, calcite, and chlorite typically occur as vein material. Diagenetic cement may be represented in the abundance of matrix calcite and siderite. Some veins are mineralized with pyrite and iron-oxides. Mineralization is typically disseminated in wall rock and crosscutting veins.

Table 1 (below): Petrographic data. Mineral assemblages are listed in order of decreasing abundance. Photomicrographs of each thin section are included in attached CD.

TABLE 1

Sample	Location NAD83 UTM(E)	Location NAD83 UTM(N)	Protolith	Rock Type	Notes	Mineral Assemblage
M002	561258	5296117	basalt	foliated basalt	calcite vein	plag+mgchl+ser+opaque
M003	561258	5296174	basalt	ser-carb schist	coherent shear lenses separated by anast foliation	Plag+ser+calc+mgchl
M004	561258	5296174	andesite	ser-chl-carb schist	calcite vein	plag+calc+ser+mgchl+qtz
M006	560504	5295842	basalt	ser-chl-ank schist	anast foliation, 1-5 cm pumice, ank-ser alteration	plag+chl+ser+ank
M008	554185	5295680	mafic volcanic	carb-ank-schist	anast foliation network, ank vein, chl nodules 2cm	plag+ank+calc+mgchl+act+ep
M010	557108	5296406	andesite	ank schist	qtz vein coarse grained	plag+ank+qtz
M011	557108	5296406	basalt	chl-ser schist	qtz vein coarse grained	mgchl+plag+ser
M012	557108	5296406	andesite	chl-ser schist	qtz vein coarse grained	mgchl+plag+ser+qtz
M014			andesite	ser schist		ser+qtz
M016	557501	5296665	andesite	ser schist	anast ser, qtz veins	ser+qtz
M019	555635	5295284	andesite	carb-ank-schist	anast ser, qtz veins	qtz+plag+ser+ank+Fechl
M020	558291	5296133	intermediate volcaniclastic	ser-ank schist	anast ser, qtz veins	ser+Fechl+qtz
M021	558291	5296133	felsic volcanic	ser-ank schist	euhedral qtz xstls (2mm)	ser+qtz+ank+Fechl+mgchl
M022	559374	5296388	mafic volcanic	Fechl-carb schist	almost all Fe chl, sulfides	mgchl+Fechl+plag+carb
M023	559374	5296388	andesite	act schist	qtz vein coarse grained	act+qtz
M025	559374	5296388	mafic volcanic	chl-carb schist	Mg-chl, anast fabric	felds+mgchl+carb
M028	559920	5296647	mafic volcanic	ser-carb schist	chl nodules	ser+carb+mgchl
M032	558487	5295314	basalt	ser-chl-carb schist	foliation present, ser alteration	plag+ser+chl+ms
M038	561217	5296530	volcanic ash	chl schist	anast chl, felty plag	chl+felds
M042	560941	5296486	mafic volcanic	carb-chl schist	calcite with chl nodules, sulfides	carb+mgchl
M043	560941	5296486	volcanic ash	chl schist		felds+mgchl+opaques
M044	560700	5296374	volcanic ash	chl schist	felty plag	felds+mgchl+opaques

TABLE 1 Continued

Sample	Alteration minerals	Metamorphic Grade	Grain Size	Picture
M002	chl + ser	gs	f.g.	M002_10x_XP, M002_4x_XP
M003	chl + ser	gs	f.g.	M003_4x_XP, M003_10x_XP
M004	chl + ser	gs	f.g.	M004_4x_XP, M004_4x_XP_cprime
M006	chl + ser	gs	f.g.	M006_4x_XP, M006_10x_XP
M008	ank + chl + ep	gs	v.f.g.	M008_4x_PP_flat, M008_4x_XP
M010	ank	gs	v.f.g.	M010_4x_XP
M011	chl + ser	gs	v.f.g.	M011_4x_XP, M011_10x_XP
M012	chl + ser	gs	v.f.g.	M012_4x_XP, M012_4x_XP
M014	ser+qtz	gs	f.g.	M014_4x_XP
M016	ser+qtz	gs	v.f.g.	M016_4x_XP
M019	ser+ank +chl	gs	v.f.g.	M019_4x_XP, M019_10x_XP
M020	ser + Fe chl + qtz	gs	v.f.g.	M020_4x_XP, M020_4x_XP_vein, M020_4x_PP
M021	ser + qtz +chl	gs	v.f.g.	M021_4x_XP, M021_10x_XP
M022	chl	gs	v.f.g.	M022_10x_PP, M022_4x_XP
M023	act			
M025	chl	gs	f.g.	M025_4x_XP
M028	ser + chl	gs	v.f.g.	M028_4x_XP, M028_4x_pyr, M028_4x_boudin, M028_10x_LL, M028_10x_RL
M032	ms + chl + ser	gs	c.g.	M032_4x_XP, M032_4x_break
M038	chl	gs	f.g.	M038_10x_PP, M038_4x_XP
M042	chl	gs	v.f.g.	M042_4x_PP
M043	chl	gs	m.g.	M043_4x_XP, M043_4x_PP
M044	chl	gs	m.g.	M044_4x_PP, M044_4x_RL

TABLE 1 Continued

Sample	Location		Protolith	Rock Type	Notes	Mineral Assemblage
	NAD83 UTM(E)	NAD83 UTM(N)				
M046	560480	5296365	basalt	chl-carb schist	Fe chl and Mg chl, calcite veining	mgchl+felds+carb+ep
M047	570856	5295669	diorite	act-bt-schist	sulfides present	qtz + bt+act + chl + py + ep
M049	570856	5295669	andesite	act-chl schist	fine grained act	act+mgchl+qtz+plag
M050	553355	5294380	andesite	act-chl schist	sulfides present	act+mgchl+qtz+plag+calc+py
M051	570917	5295762	andesite	bt-ms-chl schist	well foliated, sulfides present	bt + ms + chl + sulfides + fe oxide
M053	578148	5297505	basalt	chl-carb schist	chl, sulfides present	chl+plag+calc+ep+py
M055	560369	5295790	basalt	chl schist	sulfides present	chl+plag
M056	560444	5295855	basalt	chl-carb schist	well foliated, iron staining	mgchl+carb+plag
M057	553401	5294445	intermediate volcaniclastic	mica schist	welded pumice?	qtz+plag+ms+bt
M058	553401	5294445		ser schist		plag+ser
M059	553397	5294453	basalt	ank-ser-chl schist	well foliated, heavily altered, pockets of ank	ank + ser + chl + ep
M081	561497	5297403	andesite	chl-ank-ser-quartzo schist	ank staining, qtz clusters	chl + mica + qtz + ser + ank
M087	560895	5296881	andesite	chl-ser schist	euhedral felds xtls	qtz+chl+ser+ank
T403	558043	5296202	andesite	ser schist		ser+qtz+chl
T405	557984	5296764	diorite	chl-ser schist	similar to T403	qtz + ser + chl
T409	557973	5296968	andesite	quartzo ser-chl-ank schist	well mineralized	qtz + ser + ank
T418	559299	5296543	basalt	chl-carb schist	anast chl matrix	chl + plag + carb
T419	559244	5296557	basalt	chl-carb schist	calcite nodules	chl + plag + calc
T420	559267	5296674	basalt	Fe chl-ank schist	Fe chl	chl + plag + qtz
T424	562917	5296021	basalt	chl-carb schist	py mineralization	plag + calc + ank + ms

TABLE 1 Continued

Sample	Alteration minerals	Metamorphic Grade	Grain Size	Picture
M046	chl + ep	gs	f.g.	M046_4x_PP
M047	bt + chl + ep	gs	v.f.g.	M047_4x_PP, M047_4x_XP
M049	act + chl	gs	v.f.g.	M049_4x_PP, M049_4x_PP2, M049_4x_PP3
M050	act + chl	gs	v.f.g.	
M051	bt + ms + chl	gs	f.g.	M051_4x_XP, M051_4x_RL
M053	chl+ep	gs	f.g.	M053_4x_PP
M055	chl	gs	f.g.	M055_4x_XP, M055_4x_XP2
M056	chl	gs	f.g.	M056_4x_PP
M057	ms+bt	gs	f.g.	M057_10_XP, M057_10x_XP2
M058	ser	gs	v.f.g.	M058_4x_PP, M058_4x_PP, M058_10x_XP
M059	ank + ep	gs	v.f.g.	M059_4x_XP, M059_4x_XP_RL
M081	ser + mica + ank	gs	f.g.	M081_4x_PP, M081_4x_XP
M087	chl+ser+ank	gs	c.g.	M087_4x_XP, M087_4x_PP
T403	ser+chl	gs	v.f.g.	T403_10x_XP, T403_10x_PP
T405	ser + chl	gs	v.f.g.	T405_4x_PP
T409	ser + ank	gs	f.g.	T409_4x_XP, T409_10x_PP
T418	chl	gs	f.g.	T418_10x_PP
T419	chl + calc	gs	f.g.	T419_4x_PP
T420	Fe chl	gs	m.g.	T420_4x_PP
T424	ank + ms	gs	f.g.	

Modal abundances of alteration minerals present in thin section include (in order of most abundant to variable) magnesium-chlorite, quartz (silicified), sericite, carbonate, iron-chlorite, ± actinolite, ± secondary feldspar, ± epidote, ± pyrite, ± biotite. Alteration zones progress from greenschist metamorphosed unaltered metabasalt, meta-andesite, and metadacite to a chlorite alteration, carbonate-chlorite alteration, and carbonate-sericite ± green mica alteration.

The metamorphic mineral assemblages of 41 thin sections indicate that the rocks experienced greenschist (Chl + Alb + Ep + Qtz ± Act) facies metamorphism (Winter, 2000). Mineral assemblages indicating amphibolite (Hbld + Plag ± Grt) facies metamorphism were not found in thin section.

2.3 Microstructural Fabric

A deforming body of rock records incremental strain through ductilely and brittlely deformed tectonites, which record particle displacement through time. Discernable asymmetric fabric in an oriented thin section displays a motion plane view of kinematic features such as: 1) *ductile*; S-C fabric, sigmoids, bent or folded veins, asymmetric boudins, and fragmented porphyroclasts; and 2) *brittle*; displacement markers, veins, fractures, incohesive and cohesive brittle fault rocks, pseudotachylyte, and slickensides (Passchier and Trouw, 2005). These indicators are useful when describing a shear zone, its mode or modes of deformation, and local shear sense with respect to map structures.

S-C fabric is a robust shear sense indicator. Generally, penetrative S foliation is defined by metamorphic compositional layering consisting of micaceous, siliceous, carbonaceous, or epidote-rich layers. C foliation is spaced foliation defined by micaceous minerals or shear bands, and cross cut S foliations. The relationship between two foliations, S and C, define the orientation of non-coaxial shear. However, many samples from the Murray Shear Zone are fine grained and therefore difficult to distinguish S or C foliations.

2.4 Microstructure Data

Shear sense was interpreted from S-C fabric, boudinaged veins, porphyroblasts with tails, folded veins, and micro-faults (Figure 25). Interpretation of the micro-section data utilized a level-of-confidence scale from 1-5; 1 being the lowest. Features like porphyroblasts and sigmoids signify low confidence, whereas well defined S-C fabric represents high confidence. Depending on the orientation of each thin section north-side-up or south-side-up indicators were extrapolated from shear sense. Table 2 summarizes the data for each oriented thin section.

Microstructures within the Murray Shear Zone are dominated by an alignment of platy minerals in parallel to anastomozing F_m or C-planes (Figure 26). Out of 41 thin sections, 28 show defined C-planes, some very intensely foliated. In a few cases S and C planes in one area of a thin section show an opposite angular relationship than that recorded in another area of the same section. The two foliations do not overlap or crosscut each other. This fact is taken to represent coaxial shear or flattening in which bisecting planes of no finite elongation have an equal and opposite shear sense. Two

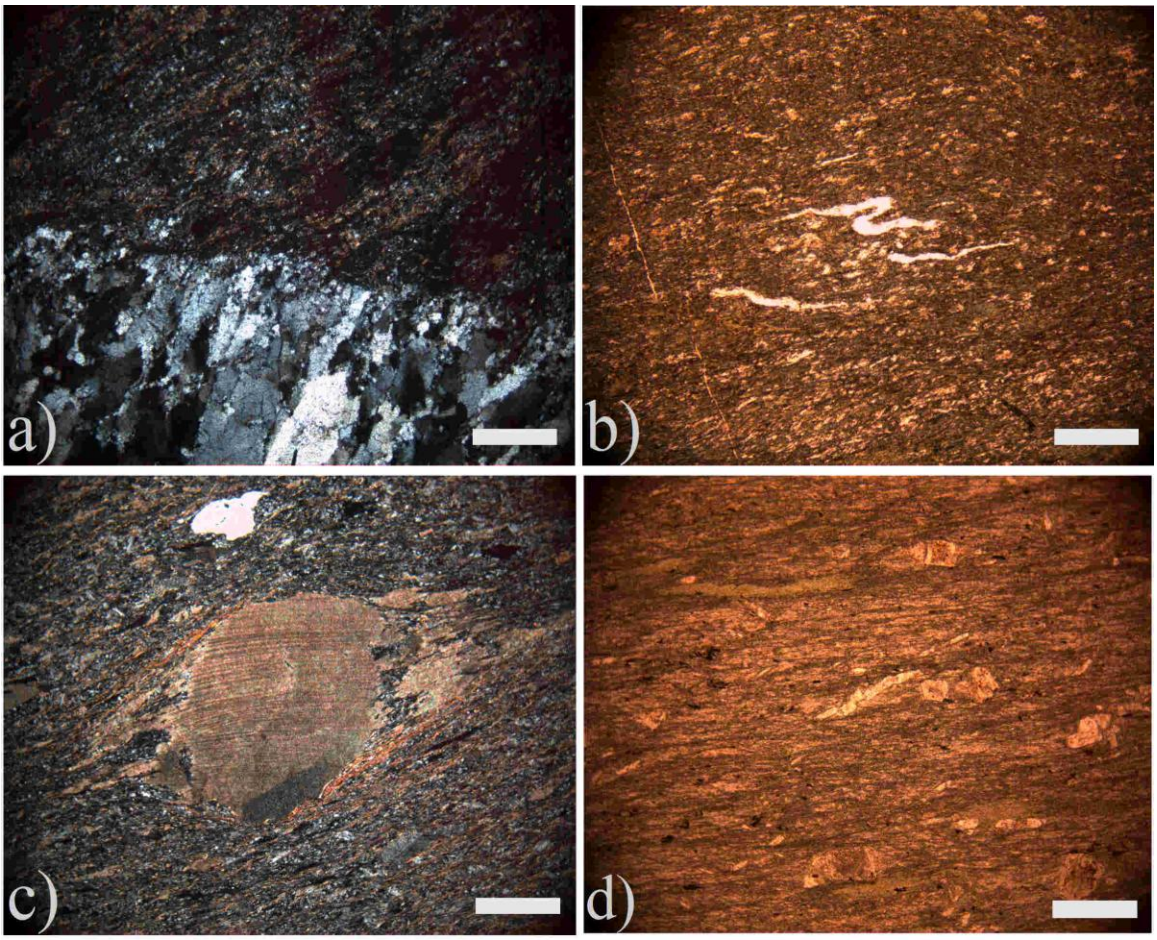

Figure 25: Photomicrographs of deformation features used for kinematic interpretation, scale bar = 1mm. a) Sample M010 (cross nicols), dilational quartz vein with strong grain shape preferred orientation (GSPO) parallel to direction of opening and normal to vein walls, note foliation oblique to vein; b) Sample M049 (plane polarized light), ductile after brittle deformation shown in buckle-folded quartz vein, dextral sense of shear; c) Sample M019 (cross nicols), mantled calcite porphyroclast showing sigma-type trails, note fine grained groundmass; d) Sample M022 (plane polarized light), brittle features in boudinaged feldspar grain (center) and faulted chlorite (upper left).

shear senses and parallel C-planes coincide with an instantaneous strain ellipse aligned with foliation, thus interpreted to be the product of flattening (Figure 27c).

Of the 28 samples with defined F_m only two have a slight shear sense in addition to C-plane development. The other 26 sections lack recorded shear sense. The remaining 13 without F_m have some form of shear fabric but lack definitive S-C or F_m fabric with which to base interpretations. However, only one sample has a confidence level of 5 (Sample M049). This high level of confidence resulted from S-C fabrics, Z folds (Figure 25b), and a faulted vein, all of which indicate right lateral shear. The other 12 samples show a weak to moderate sense of shear with no S-C fabric. In those cases the fine grained nature of the sample prevented observation of concise structure.

Some samples contain a crenulation cleavage forming tight wavy F_m as evident in sweeping extinction using cross polars (Figure 27a). The crenulation is defined by small folds in micaceous layers and helps identify angular relationships between S and C planes. Crenulation folds are difficult to see in the photomicrograph of Figure 27a; lines highlight axial planes of crenulation folds. Shear sense is found in the same manner as 'Z' or 'S' folds with respect to the axial plane; 'Z' folds are right lateral and 'S' folds are left lateral.

Grain shape preferred orientation (GSPO) of calcite and quartz reflects the strain ellipse orientation with respect to foliation and, thus, shear sense. GSPO is evident in strain shadows of porphyroblasts (Figure 25c), dilational veins (Figure 25a), and within planes of F_m (Figure 26c). Preferred growth of crystals or the reorientation of grains through rotation represent a GSPO, formed by the dissolution of material on the side of

instantaneous shortening and growth of quartz fibers in the orientation of instantaneous stretching. GSPO is a useful tool to identify shear sense if it exists in a similar orientation throughout a sample.

Microstructures and kinematic patterns in thin sections confirm a brittle-ductile environment with intermingling ductile and brittle failure (Figure 25 and 26). Ductile deformation features like C fabric (Figure 26), Z folds (Figure 25b) GSPO, and mantled porphyroclasts (Figure 25c) are consistent with a continuous time-transgressive deformational history. Brittle features such as dilational veins and micro-faults cut ductile features (Figure 25a, d). Evidence of ductile deformation after brittle, i.e. folded dilational veins (Figure 25c), or brittle deformation after or during ductile, i.e. dilational veins crosscutting foliation and broken feldspar crystals within planar chlorite fabric (Figure 25 and 26), give rise to interacting discontinuous and continuous deformation. This interaction very likely occurred at or near the brittle-ductile transition.

2.5 Kinematic Map

Microstructural kinematic data is helpful when evaluating localized kinematic response patterns within a regional pattern of deformation. Microstructural kinematic data was plotted at sample locations as a stereonet of individual sample orientations including north- and south-side-up indicators (Plate 1). A larger stereoplot shows F_m and L_e data, illustrating that F_m and L_e are similar across the Murray Shear Zone. North-side-up and south-side-up indicator data does not coincide with a high confidence level. The low confidence might be partly attributed to variations in rheology and therefore slip planes within a host rock. Rheology contrasts may result from changes in gross lithology

or protolith. Some areas may show north-side-up indicators while others close by have south-side-up, but the overarching event at the time(s) of deformation may produce both indicators.

2.6 Microstructural Analysis and Summary

The major theme of Murray Shear Zone deformation appears to be sub-horizontal flattening strain and dip-slip shearing evident in the majority of samples. Remaining samples confirm a degree of deformation through shear fabric, although lacking F_m. Flattening strain and dip-slip shear are deduced from the following: 1) sub-vertical F_m; 2) sub-vertical L_e; 3) asymmetric (shear) fabric oriented in a sub-vertical motion plane, which consistently parallels a cross sectional (N-S) plane through the Murray Shear Zone; 4) sub-horizontal dilational veins; and 5) boudinaged veins and crystals oriented sub-vertically.

The requirement for a particular orientation of a Z-axis is to be perpendicular to F_m. Orientations of both F_m and L_e are consistent with sub-horizontal shortening and sub-vertical elongation strain from dip-slip shearing. Shear fabric asymmetry occurs in a generally vertical plane, whereas dilational veins are subhorizontal—normal to foliation. Boudinaged veins and feldspar grains have their axis of elongation oriented sub-vertically within the plane of foliation. Strain shadows adjacent to porphyroblasts and relict quartz grains exist sub-vertically with evidence of dissolution on the perpendicular grain surfaces or the side experiencing shortening. All of these features present a case for horizontal contraction, dip-slip shear, and subsequent vertical extrusion of the crust within the Murray Shear Zone.

Table 2 (below): Microstructural data for each oriented thin section from the Murray Shear Zone. Kinematic indicators include south-side-up and north-side-up. A level of confidence from 1-5 is given for each sample along with indicator minerals that define microstructures.

TABLE 2

Outcrop #	Sample #	NAD83 UTM(E)	NAD83 UTM(N)	Foliation	Lineation Rake	Kinematics	Confidence	Kinematic Indicators	Foliation and S-C Defined by: Chl	Ser	Act	Calc	Qtz	Plag	Opq
M08-006	M002	561258	5296117	110/85 S		South up	3	S-C and pblast	x					x	x
M08-006	M003	561258	5296174	090/83 S	56	Flattening	0	S-C	x	x					
M08-007	M004	561258	5296174	270/76 N	85	Flattening	0	S-C, boudins	x	x	x				x
M08-010	M006	560504	5295842	090/60 S	82	Flattening	0	S-C, boudins	x	x					x
M08-013	M008	554185	5295680	290/85 N	80	Flattening	0	S-C			x	x		x	x
M08-016	M010	557108	5296406	250/50 N		South up	4	S-C and tension fractures S-C, kink	x		x		x		
M08-016	M011	557108	5296406	264/84 N	120	Flattening	0	folds, GSPO	x		x				
M08-016	M012	557108	5296406			Flattening	0	pblast, boudins		x			x		
M08-019	M014	556500	5296352	275/80 N	60	Flattening	0	pblast, boudins		x		x	x		x
M08-021	M016	557501	5296665	241/87 N	90	Flattening	0	S-C and actinolite mats		x	x		x		
M08-028	M019	555635	5295284	267/85 N	120	South up	4	S-C, rotated pblast	x	x					
M08-030	M020	558291	5296133	274/90 N	104	Flattening/ SUP	2	S-C	x	x					
M08-030	M021	558291	5296133	283/86 N	132	Flattening	0	S-C		x			x		
M08-033	M022	559374	5296388	084/90 S	67	Flattening	0	S-C and chl mats, boudins	x						x
M08-033	M023	559374	5296388	272/90 N	62	Flattening	0	S-C			x				
M08-033	M025	559374	5296388	092/90 S	66	Flattening	0	S-C	x				x		
M08-047	M028	559920	5296647	094/78 S	87	Flattening	0	S-C and actinolite mats	x	x	x		x		

TABLE 2 (Continued)

Outcrop #	Sample #	NAD83 UTM(E)	NAD83 UTM(N)	Foliation	Lineation Rake	Kinematics	Confidence	Kinematic Indicators	Foliation and S-C Defined by: Chl	Ser	Act	Calc	Qtz	Plag	Opq
M08-037	M032	558487	5295314	295/70 N	95	Flattening	0	boudins	x	x					
M08-056	M038	561217	5296530	264/76N	84	North up	4	S-C	x					x	
M08-061	M042	560941	5296486	095/77 S	100	North up	2	strain shadows, tension fractures	x	x			x		x
M08-061	M043	560941	5296486	249/80 N	95	North up	3	S-C, pblast	x				x		
M08-060	M044	560700	5296374	110/88 S	94	Flattening	0	S-C	x				x		
M08-066	M046	560480	5296365	110/90 S	75	Flattening	0	S-C	x	x			x		
M08-067	M047	570856	5295669	276/85 N	80	Flattening	0	S-C and biotite mats	x						
M08-068	M049	570856	5295669	105/90 S	50	South up	5	S-C, z folds	x		x				
M08-069	M050	553355	5294380	270/69 N	70	?		tension fractures	x		x				
M08-063	M051	570917	5295762	268/60 N	90	Flattening	0	S-C and chlorite mats	x		x		x		
M08-062	M053	578148	5297505	250/70 N		Flattening	0	chl foliation	x						
M08-059	M055	560369	5295790	304/74 N	84	Flattening	0	S-C	x				x		
M08-075	M056	560444	5295855	105/85 S	90	South up	2	strain shadows, tension fractures	x				x		
M08-076	M058	553401	5294445	024/87 S	62	North up	2	S-C	x	x		x			
M08-077	M059	553397	5294453	190/83 N	130	South up	1	S-C	x	x			x		x
M08-095	M081	561497	5297403	090/65 S	65	Flattening	0	S-C and ser mats	x	x		x	x		

TABLE 2 (Cont.)

Outcrop #	Sample #	NAD83 UTM(E)	NAD83 UTM(N)	Foliation	Lineation Rake	Kinematics	Confidence	Kinematic Indicators	Foliation and S-C Defined by: Chl	Ser	Act	Calc	Qtz	Plag
M08-098	M087	560895	5296881	262/83 N	90	Flattening	0	S-C	x			x	x	x
M08-101	T401	558110	5296104	115/38 S	96	South up	3	S-C and tension fractures	x			x	x	x
M08-106	T403	558043	5296202	100/71 S	55	Flattening	0	S-C	x		x			
M08-112	T405	557984	5296764	280/82 N	135	Flattening	0	S-C	x	x	x			x
M08-118	T409	557973	5296968	095/58 S	75	Flattening/ SUP	2	S-C, GSPO	x			x		x
M08-135	T418	559299	5296543	276/77 N	100	North up	4	S-C actinolite mats	x		x			x
M08-136	T419	559244	5296557	266/90 N	120	Flattening	0	S-C and strain shadows	x		x	x		
M08-138	T420	559267	5296674	256/88 N	130	South up	4	S-C and chlorite mats	x					
M08-151	T424	562917	5296021	072/85 S	82	Flattening	0	S-C and strain shadows	x		x	x		

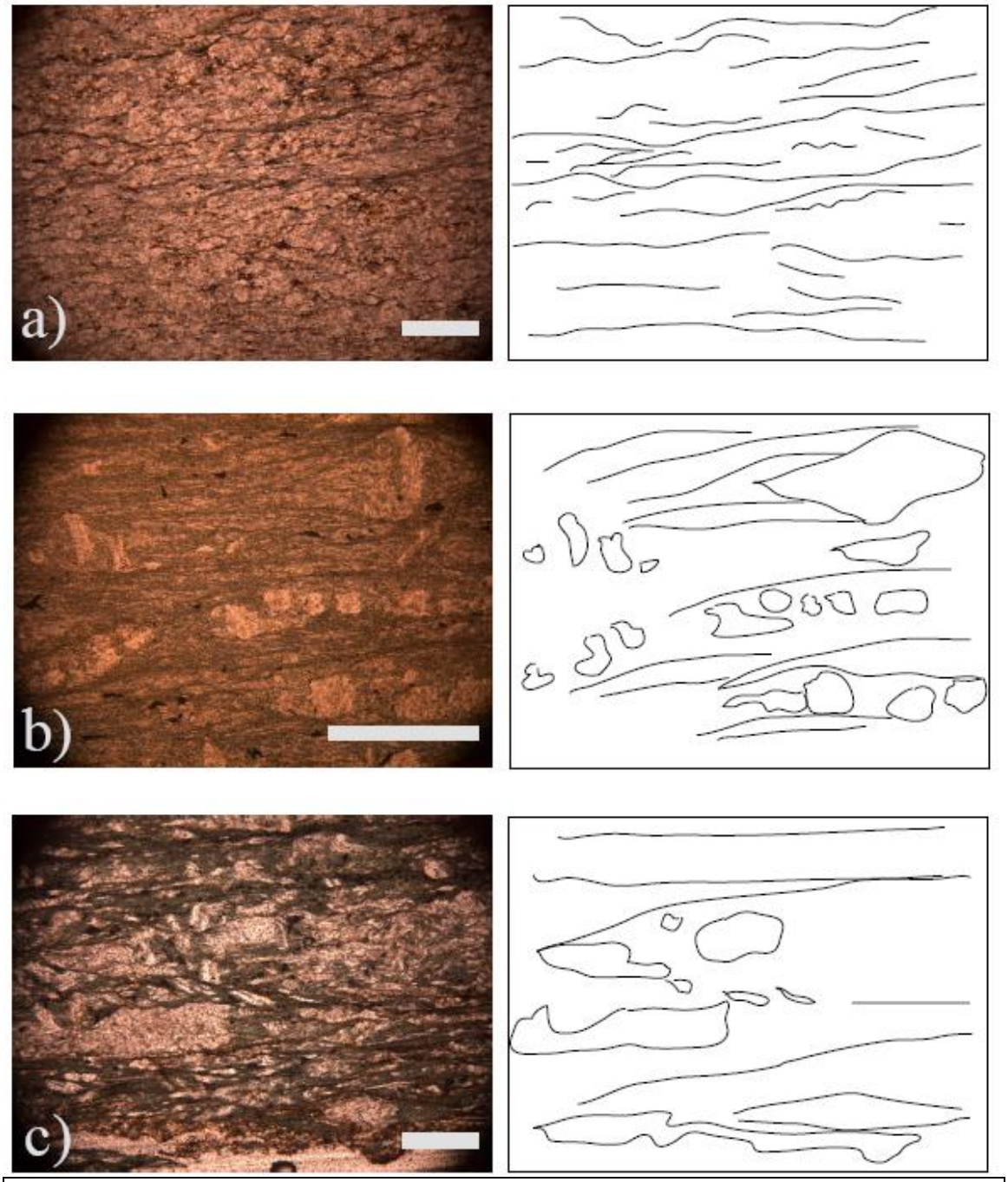

Figure 26: Photomicrographs of penetrative F_m from the Murray Shear Zone, scale bar = 1mm. Sketches to the right highlight foliation (C planes) and deformation features such as boudinaged feldspar crystals. **a)** Sample M008 (plane polarized light), planar to anastomozing chlorite marking F_m. **b)** Sample M022 (plane polarized light), planar chlorite marking F_m and boudinaged feldspar crystals representing brittle deformation. **c)** Sample T418 (plane polarized light), planar to anastomozing chlorite marking F_m and shards of feldspar aligned sub-horizontally in the plane of F_m.

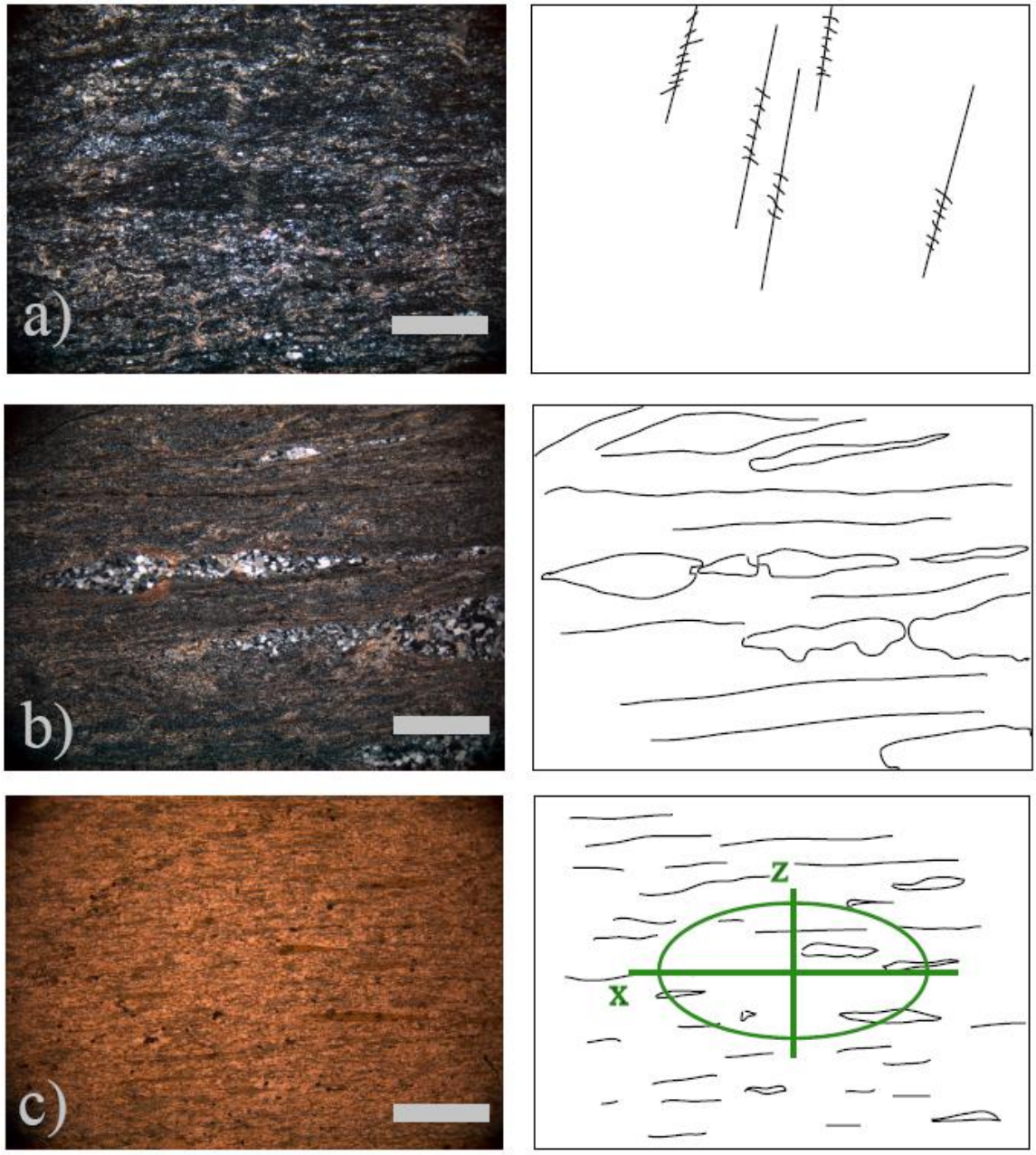

Figure 27: Photomicrographs of deformation features, scale bar = 1mm. **a)** Crenulation cleavage in a fine grained chlorite-sericite schist, axial planes shown to the right. **b)** Flattening in fined grained sericite schist as evidenced by boudins and parallel C-planes. **c)** Flattening in chlorite-biotite schist. Strain ellipse drawn in orientation of predicted flattening strain. Z = shortening axis, X = elongation axis.

3. Laboratory Data: Geochemistry

Geochemistry is a tool by which to evaluate chemical attributes of rocks. Chemical attributes of rocks may be the result of primary or secondary processes (Rollinson, 1993). In order to fully understand and accurately interpret secondary lithogeochemical changes associated with alteration processes it is essential to first understand a rock's primary composition (Grant, 1986).

Metasomatism is a secondary process which changes textural, mineralogical, and lithogeochemical characteristics of the rock (Winter, 2000). Thus, examination of both mineral assemblages and the lithogeochemical characteristics of those mineral assemblages are essential to understand metasomatic processes, some of which may be associated with ore forming systems. This thesis represents the first detailed major and trace element evaluation of the geochemical characteristics of the Murray Shear Zone hydrothermal system. Given the similarities in structural style and alteration assemblages associated with this hydrothermal event and shear zones which host economic gold mineralization in Archean rocks elsewhere (e.g. Canada, Australia, South Africa), the results of this study may shed light on the potential for the Murray Shear Zone to host economically significant mesothermal gold mineralization.

3.1 Methods

Whole rock and trace element lithogeochemical analysis was performed on 21 rock samples (Table 3). Three sample groups were chosen based on: 1) presence of quartz veins with varying amounts of mineralization; 2) continuity of rock type at sample locations; and 3) perceived alteration changes laterally adjacent to veins.

Group 1 (Location A, Plate 1, and Figure 21) includes the Murray Vein of outcrop M08-003, and is composed of eleven variably altered basalts and one quartz sample. Group 2 (Location B, Plate 1) is located at outcrop M08-033, and is composed of three basalt samples and one quartz sample. Group 3 (Location C, Plate 1) comprises three felsic volcaniclastic samples and one quartz sample within outcrop M08-030. Additionally, one quartz sample from outcrop M08-029 was selected for gold analysis only (Location D, Plate 1). No perceived hydrothermal alteration was noted in this quartz vein which cuts through greenschist facies metamorphosed gabbro.

Sample collection was done utilizing a hand-held gasoline powered diamond drill with a BQ-size (36.4 mm) diamond drill bit. At each sample location the rock was drilled to a depth of approximately 12 centimeters. Upon completion of the drilling the core was extracted by first breaking the sample from the outcrop by applying lateral pressure using a 6 inch screw driver, then removing the core sample from the outcrop with a thin forceps. Samples were labeled and placed in a plastic bag, and after removal of surface weathering, were sent to ACTLABS (Ancaster, Ontario, Canada) for preparation (crushing with mild steel) and major- and trace-element lithogeochemical analysis.

Prior to analysis, the entire sample was crushed to a nominal minus 10 mesh (1.7 mm), mechanically split to obtain a representative sample and then pulverized to at least 95% minus 150 mesh (106 microns). Sample crushing utilized mild steel to minimize contamination (www.actlabs.com). Twenty samples were analyzed using the following techniques: 1) major and trace elements utilizing the "4LITHO" technique (fusion ICP-MS); 2) Au via fire assay; and 3) CO_2 assay. Major element oxides and CO_2 report in

weight percent, and various base and precious metals and trace elements report in parts per million (ppm). The Murray Vein sample (MV) was assayed using ACTLABS instrumental neutron activation analysis (INAA) and fire assay methods to determine both its gold content and geochemistry. Other quartz samples were analyzed only for gold values. Detailed descriptions, method detection limits, and analytical results of these lithogeochemical analyses and assays are included in Appendix 3. The IGPET2002 software package (Carr, 2002) was utilized to evaluate the primary lithogeochemical characteristics of the sample and to classify the rocks utilizing the methods of Pearce (1996) and LeMaitre et al. (2002). The isocon method (Grant, 1986) was utilized to evaluate metasomatic changes associated with hydrothermal alteration which affected the samples.

3.2 Primary Rock Compositions

Rock samples were lithologically classified using both major and trace element ratios. Samples collected for this study are fine-grained to very fine-grained and therefore required geochemical analysis to unambiguously determine chemical composition. The IUGS (International Union of Geological Sciences) accepted classification of igneous rocks whose mineral mode cannot be determined except by chemical analyses, and whose H_2O and CO_2 contents are negligible, is a TAS (Total Alkali Silica) diagram (LeBas et al., 1986; LeMaitre et al., 2002: Figure28a). The TAS classification exploits the fact that relative proportions of silica (SiO_2) and alkalis (NA_2 + K_2O) play an important role in determining mineral assemblages. Figure 29a shows data from outcrop M08-003 plotted on a TAS diagram. Note the high degree of scatter

represented in the plot. Such scatter is typical in ancient hydrothermally altered rocks due to mobility of sodium, potassium, and/or silica during hydrothermal alteration processes. This problem in variability is rectified by plotting immobile trace elements, in particular the high field strength elements (HFSE). Both Winchester and Floyd (1977) and Pearce (1996) have utilized HFSE to lithologically classify hydrothermally altered ancient rocks. This method is most effective because it does not rely on components which are mobile for classification. Ratios of the immobile elements remain constant despite later alteration allowing for comparison of altered rocks versus least altered rocks of the same protolith and therefore primary (e.g. pre-alteration) rock compositions can be determined. Pearce (1996) has utilized the immobile element ratios of Nb, Y, Ti, and Zr to lithologically classify hydrothermally altered rocks, and this method is used for classification of rocks for this study (Figure 28b). When this classification scheme is used the data cluster relatively tightly in the basalt and basalt/andesite field. The immobile element classification method of Pearce (1996) closely matches field and petrographic features in the rocks and corresponds to the observed mafic to intermediate composition.

The lithological classification results based on the TAS diagram and the Zr/TiO2—Nb/Y diagram are presented graphically in Figures 28-30. Samples from outcrop M08-003 (Figure 28) analyzed with a TAS diagram indicate a spread in composition range from picrobasalt to dacite. This is inconsistent with field and petrographic observations, in addition to possessing a degree of scatter within various compositional ranges. Those samples plotted in a Zr/TiO_2—Nb/Y diagram (after Pearce,

1996) show a variance in composition from basalt to andesite/basalt, which is more in line with field and petrographic observations.

Outcrop M08-033 samples were plotted in a TAS diagram (Figure 29a) and show a compositional range from foidite to basaltic andesite to dacite. The large ranges of compositions seem rather inconsistent with field observations, especially within a single outcrop. The same data plotted in a Zr/TiO_2—Nb/Y diagram (Figure 29b) show andesite/basalt to basalt in composition. This rather large (almost an order of magnitude difference) spread in the data may indicate two different primary lithologies. Consequently, outcrop M08-033 was not evaluated further as a primary, single protolith could not unambiguously be established.

Samples from outcrop M08-030 indicate a composition between basaltic trachyandesite to basaltic andesite to andesite when plotted on a TAS diagram (Figure 30a). These results are more consistent with mafic to intermediate lava flows as thought to be present within the study area. However, data plotted in a Zr/TiO_2—Nb/Y diagram (Figure 30b) display a group within the basalt field. The tighter cluster represents field and petrographic observations of the fine-grained rocks.

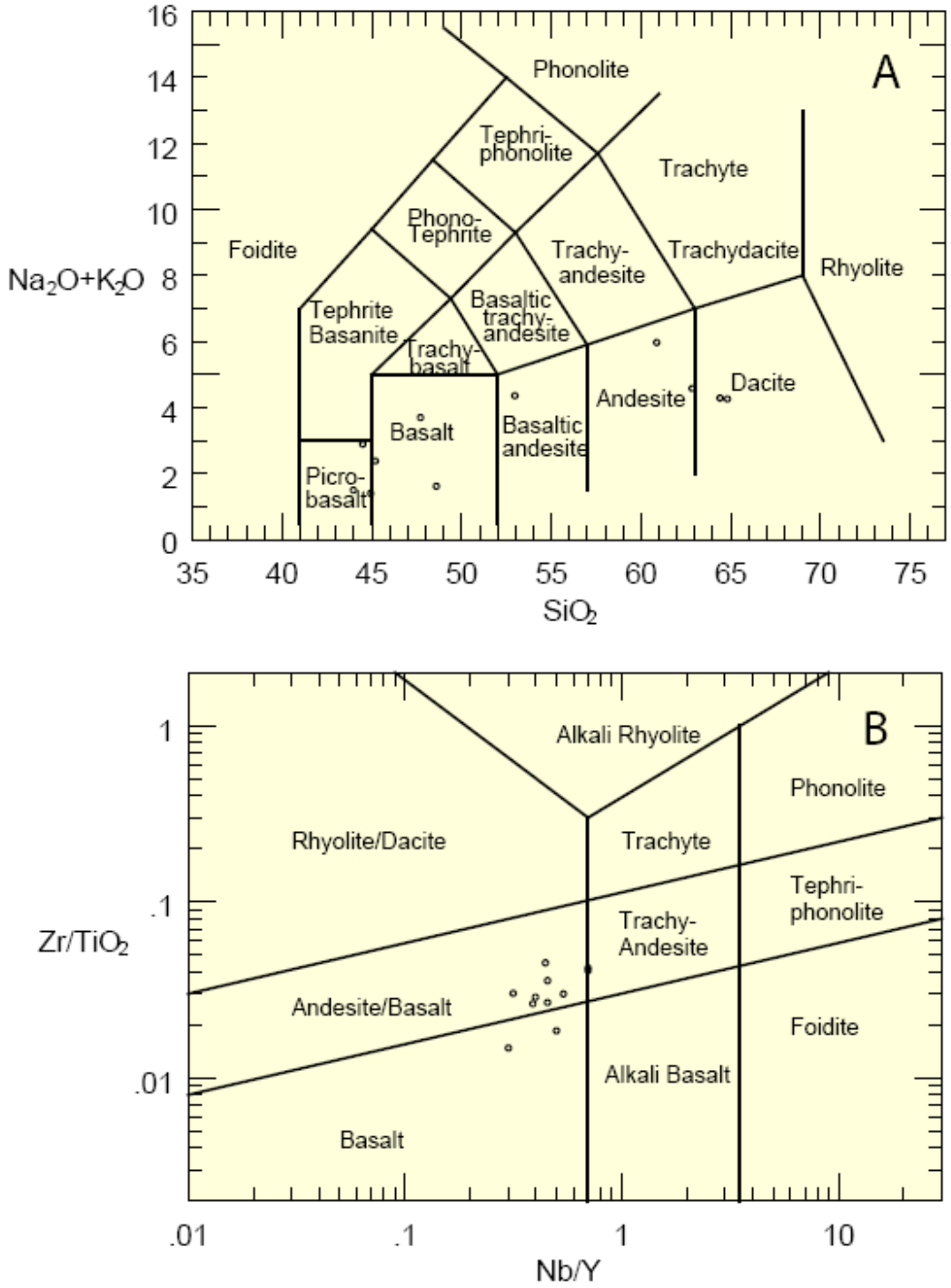

Figure 28: Lithogeochemical classification of samples collected from outcrop M08-003 utilizing both major and trace elements. **A)** Total alkalis ($Na_2O + K_2O$) versus silica classification (after LeMaitre et al., 2002) indicates that samples vary in composition from picrobasalt to dacite, which is inconsistent with field observations. **B)** Immobile element classification utilizing Zr, Ti, Nb, and Y (after Pearce, 1996) indicates that, according to least altered sample CS-C-11, the samples vary in composition from basalt to andesite/basalt, which is consistent with field observations.

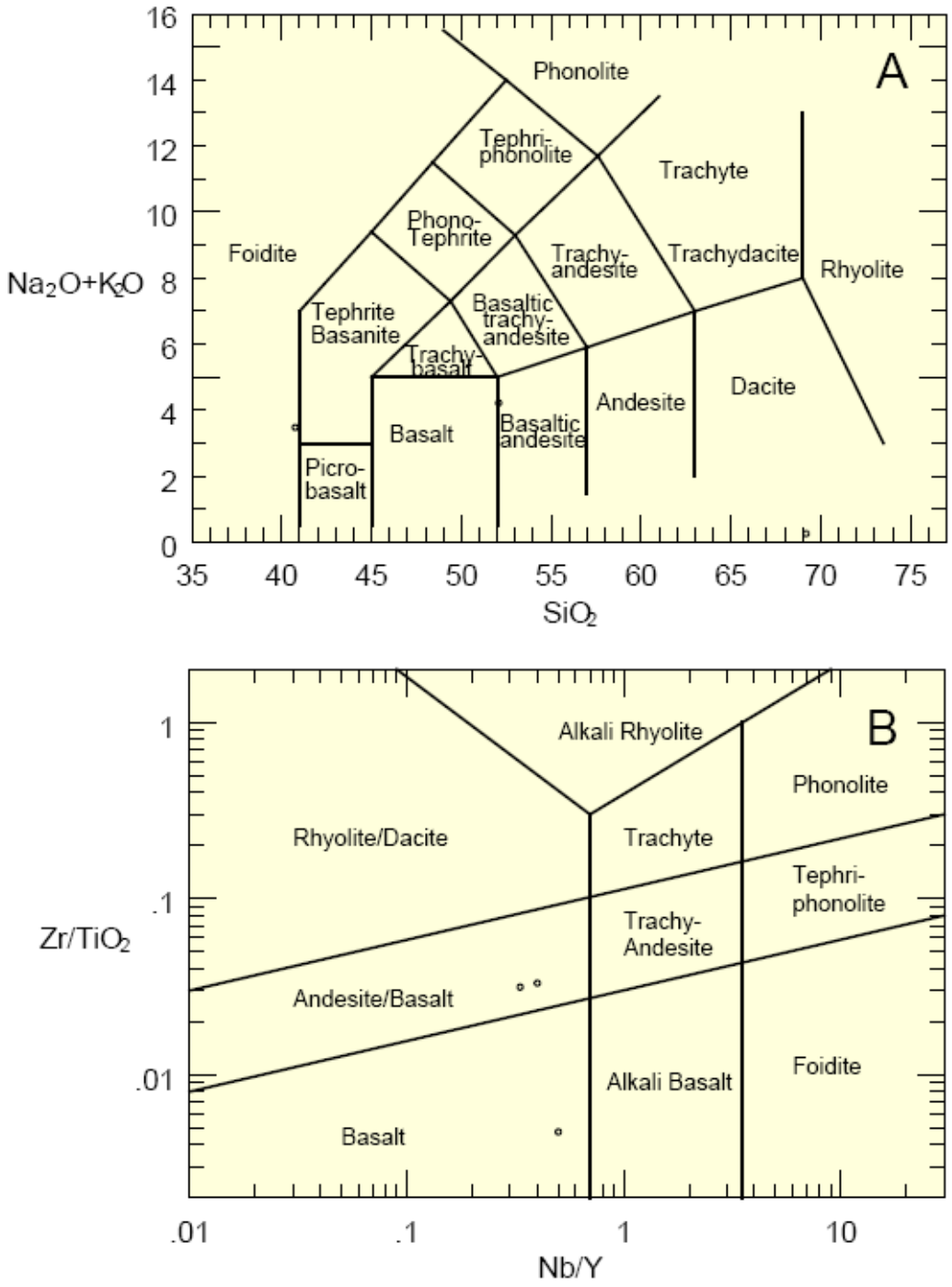

Figure 29: Lithogeochemical classification of samples collected from outcrop M08-033 utilizing both major and trace elements. **A)** Total alkalis ($Na_2O + K_2O$) versus silica classification (after LeMaitre et al., 2002) indicates that samples vary in composition from foidite to dacite, which is inconsistent with field observations. **B)** Immobile element classification utilizing Zr, Ti, Nb, and Y (after Pearce, 1996) indicates that, according to least altered sample CS-J-30, samples vary from andesite/basalt to basalt composition, which may represent two separate protoliths.

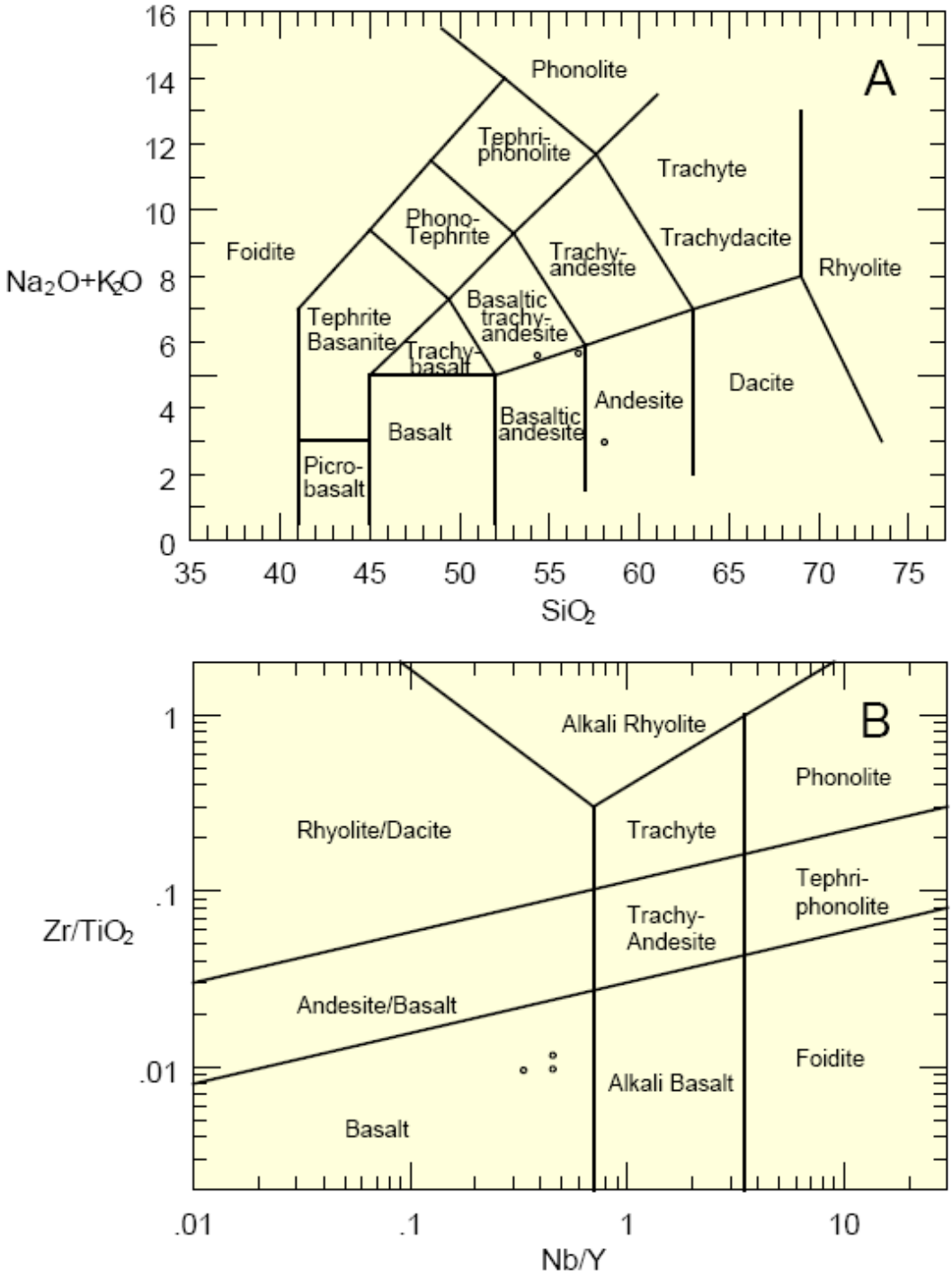

Figure 30: Lithogeochemical classification of samples collected from outcrop M08-030 utilizing both major and trace elements. **A)** Total alkalis ($Na_2O + K_2O$) versus silica classification (after LeMaitre et al., 2002) indicates that samples vary in composition from basaltic trachy-andesite to andesite, which is inconsistent with field observations. **B)** Immobile element classification utilizing Zr, Ti, Nb, and Y (after Pearce, 1996) indicates, according to least altered sample CS-I-19, a sample group of basalt composition, which is consistent with field observations.

3.3 Mass Balance Analysis

Mass balance analysis is a technique whereby the lithogeochemical characteristics associated with metasomatism can be evaluated (Gresens, 1967; Grant, 1986; Grant 2005). Mass balance enables the evaluation of lithogeochemical signatures associated with ore-forming hydrothermal systems. This technique is commonly used as a geochemical tool which enables exploration geologists to vector in to the most prospective parts of mineralizing hydrothermal systems. This thesis is the first to employ mass balance analysis to various alteration mineral assemblages associated with various parts of the Murray Shear Zone hydrothermal system.

The "isocon method" (Grant, 1986) is applied in this thesis for mass balance analysis. The isocon method is a graphical means from which mass balance analysis may be achieved. Plotting the lithogeochemistry of rocks which share the same protolith, and which are altered to different alteration mineral assemblages, is required for analysis. On an x-y graph, the lithogeochemical results of a least or less altered rock and an altered rock are plotted on the x- and y-axes, respectively. The isocon is a straight line drawn through the origin and defined by species that remain immobile during metasomatic alteration (Grant, 1986). Gained species plot above the isocon and lost species plot below. Using this technique relative gains and losses can be calculated by first calculating the slope through each component relative to the isocon. Those components that have slopes greater than the slope of the isocon are gained during the process of metasomatic alteration and those components that have slopes lesser than the slope of the isocon have been geochemically lost during the alteration process. The gains and losses

of each component are determined by evaluating the slopes of each component relative to the slope of the isocon. Summarizing from Grant (1986), the equation for composition-volume relations in metasomatic alteration is

$$C_i^A = M^O/M^A(C_i^O + \Delta C_i)$$

where C_i is the concentration of species "i" , "O" refers to the original rock and "A" to the altered rock, M^O and M^A are equivalent masses before and after alteration. ΔC_i is the change in concentration of species "i".

There are several ways to determine the isocon including changes in mass, volume, or a best-fit line through elements that are determined immobile. The constant mass isocon has a slope of 1 and is unrealistic for this work because changes in mass occurred during metasomatism. Removal of basaltic materials for less dense felsic materials (e.g. quartz, white micas) during the process of metasomatism makes a constant mass determination invalid. The constant volume isocon is a possibility; however, field evidence indicates the presence of numerous veins in the alteration zones, suggesting that, at least for a time, volume loss may have accompanied the hydrothermal alteration process. The method applied in this thesis is to define the isocon using a best-fit line through elements that were determined to be immobile during the alteration process.

Determination of immobile elements for the best fit isocon requires knowledge of electromagnetic forces in chemical bonds. Larger atoms with fewer valence electrons and therefore a lower ionic charge are considered to have a weak attraction force, whereas smaller atoms with tightly packed valence electrons and a high ionic charge would have a strong attractive force. Based on this principal Saunders et al. (1980)

proposed a definition of immobile elements utilizing ionic charge/ionic radius ratios (ir/ic), with those having ir/ic > 0.2 called low field strength elements, and those with ir/ic < 0.2 called high field strength elements (Jenner, 1996). Elements with strong attractive forces, ir/ic < 0.2, favor a solid phase over a melt phase (i.e. they are compatible). Likewise weaker elements, ir/ic > 0.2, favor the melt phase and are likely to migrate away from the original rock during hydrothermal alteration (i.e. they are incompatible). High field strength elements Ti, Zr, Hf, Nb, Ta, Y, and P, certain rare earth elements Gd, Tb, Dy, Er, Yb, and Lu, and transitional elements Cr, Ni, Sc, and V are generally immobile during hydrothermal processes.

Discrimination diagrams are used to evaluate the degree to which elements are considered immobile. Relative immobility of immobile elements becomes apparent by plotting geochemical concentration data of least altered samples against altered samples on an x-y graph (Figure 31). The set of data points corresponding to ratios of elements "before" and "after" alteration plot in a scatter within the discrimination diagram. Pairs of elements that plot along a best fit line maintain their concentration within a sample despite varying styles of alteration. These elements are considered immobile during metasomatism. Statistical analysis of the data with respect to a best fit line is a means by which to evaluate the relative immobility of elements. Elements are considered more immobile if statistics prove a higher correlation (or lower variability) in concentration between least altered and altered. The highest correlation element ratios can have is 1, where anything close to 1 is considered immobile.

Results of discrimination plots of immobile elements are displayed in Figures 31-33. Elements utilized for the isocon have the same ratios and thus have a best fit line with a high correlation coefficient (approaching 1). Elements that are mobile show scatter on discrimination diagrams in which samples containing all alteration types are plotted.

Outcrop M08-003 (also known as the Murray Vein outcrop) has concentration data plotted for the trace elements hafnium and zirconium (Figure 31a) and concentration data plotted for major elements potassium and silica (Figure 31b). Immobility of trace elements is apparent in the hafnium-zirconium plot as seen by the high correlation coefficient. These trace elements were chosen for the isocon in geochemical analysis of samples from outcrop M08-003. Major elements potassium and silica show a large degree of variation in concentration and a negative correlation coefficient. The major elements were subsequently not used as an isocon.

Outcrop M08-033 (also known as the Highway 169 outcrop) shows trace elements hafnium and zirconium as having a correlation coefficient of 1 and therefore immobile (Figure 32a). These trace elements were utilized for the isocon for analysis of samples from outcrop M08-033. Once again the major elements potassium and silica are highly variable with respect to concentrations during alteration processes (Figure 32b).

Finally, outcrop M08-030 trace elements titanium and zirconium were used for the isocon (Figure 33a). The large correlation coefficient and tight pattern of data points in relation to the best-fit line describes trace element immobility. On the other hand

potassium and silica are major elements that show a high degree of variability and are not used as an isocon (Figure 33b).

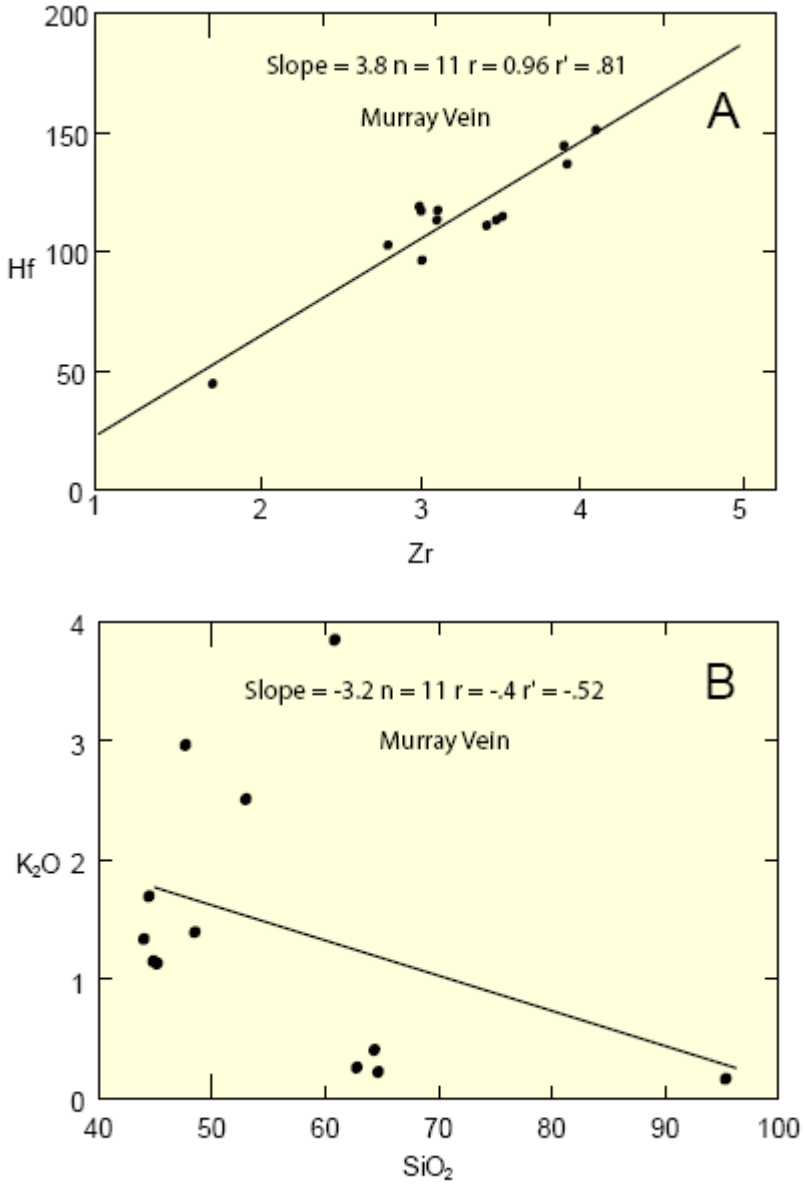

Figure 31: Variation diagrams illustrating the behavior of immobile and mobile elements throughout all the alteration mineral assemblages at outcrop M08-003 (Murray Vein). Trace element concentrations are in parts per million (ppm) and major elements are in weight percent (%). **A)** Concentrations of trace elements hafnium and zirconium plot close together with a high correlation coefficient (approaching 1) and display a best fit line with positive slope. **B)** Major element concentrations of potassium and silica show a high degree of variance noticeable in the negative correlation coefficient and inverse relationship of the best fit line.

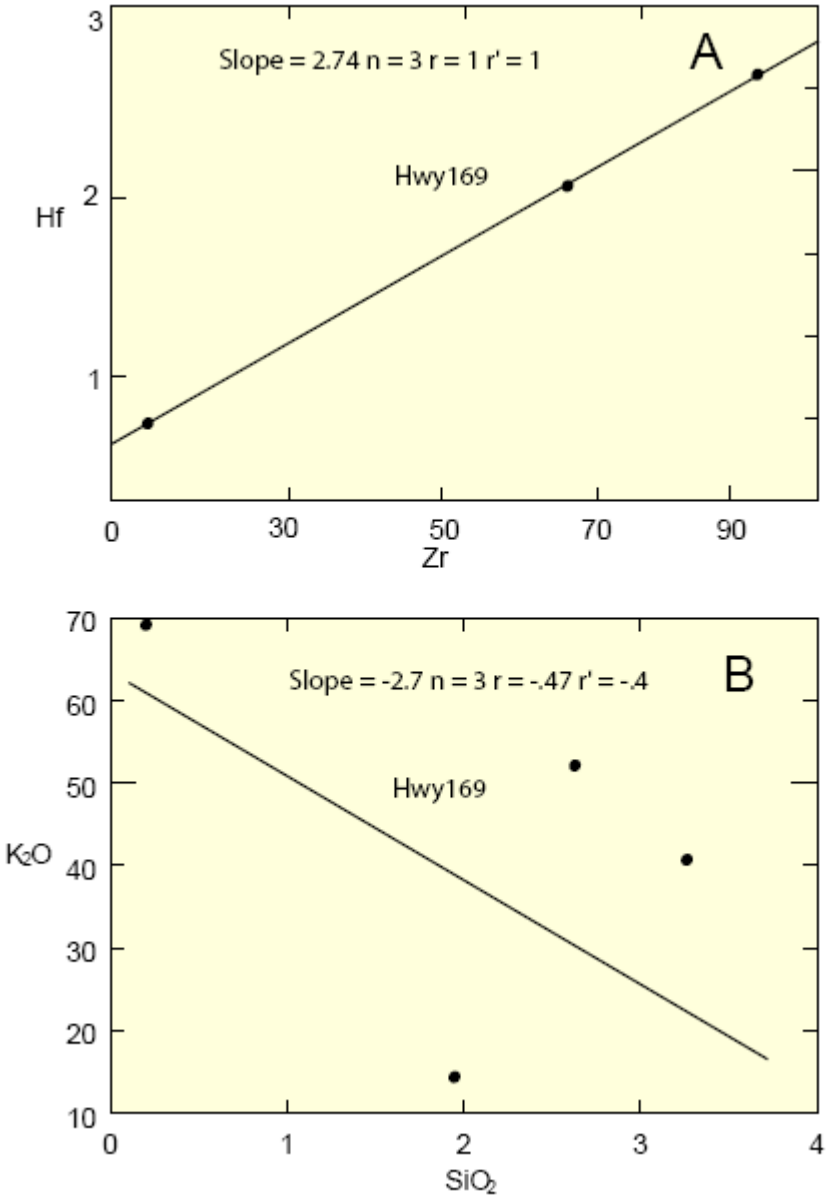

Figure 32: Variation diagrams illustrating the behavior of immobile and mobile elements throughout all the alteration mineral assemblages at outcrop M08-033 (Hwy 169). Trace element concentrations are in parts per million (ppm) and major elements are in weight percent (%). **A)** Concentrations of trace elements hafnium and zirconium plot close together with a correlation coefficient of 1 and display a best fit line with positive slope. **B)** Major element concentrations of potassium and silica show a high degree of variance noticeable in the negative correlation coefficient and inverse relationship of the best fit line.

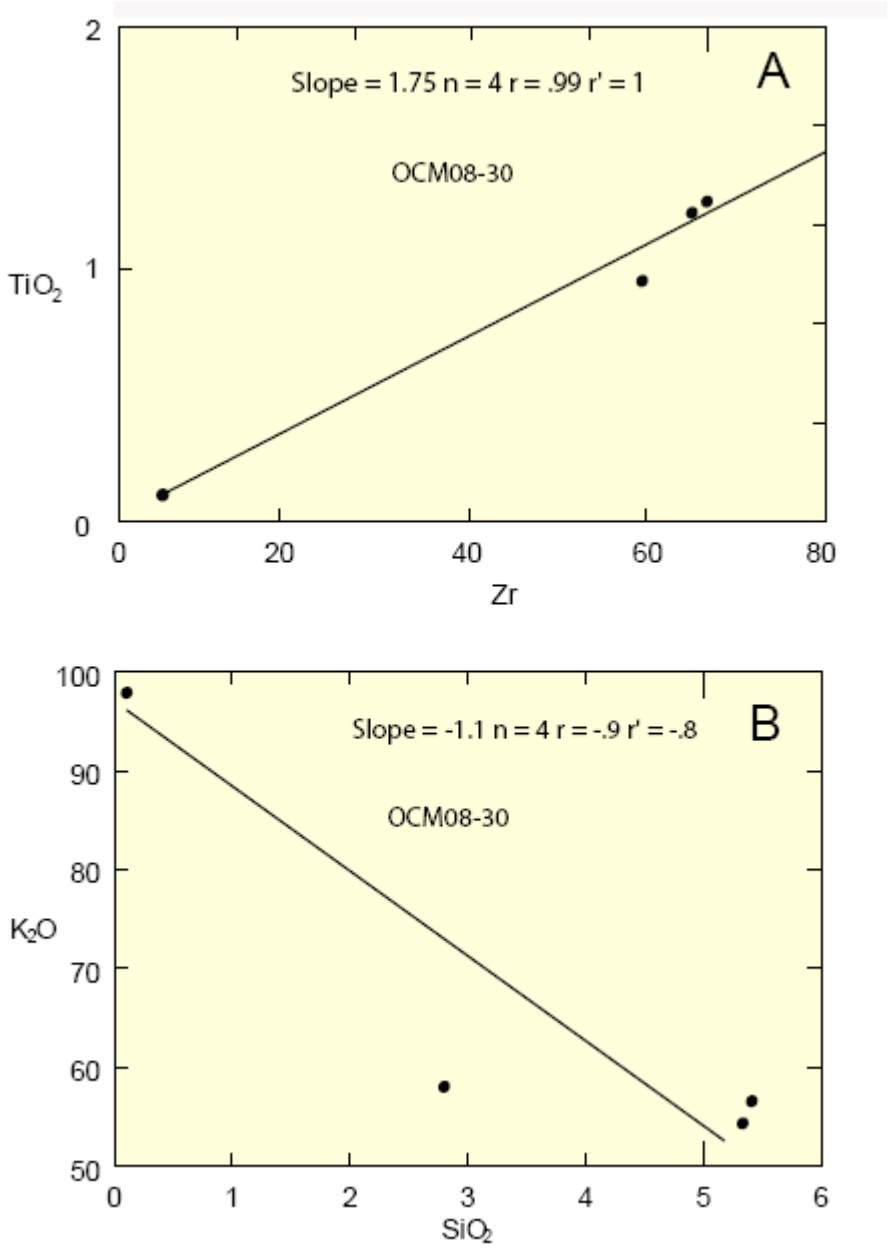

Figure 33: Variation diagrams illustrating the behavior of immobile and mobile elements throughout all the alteration mineral assemblages at outcrop M08-030. Trace element concentrations are in parts per million (ppm) and major elements are in weight percent (%). **A)** Concentrations of trace elements titanium and zirconium plot close together with a high correlation coefficient (approaching 1) and display a best fit line with positive slope. **B)** Major element concentrations of potassium and silica show a high degree of variance noticeable in the negative correlation coefficient and inverse relationship of the best fit line.

3.4 Geochemical Data and Analysis

Lithogeochemical classification and metasomatic changes were evaluated at three locations: 1) Outcrop M08-003 containing the Murray Vein (Location A, Plate 1); 2) Outcrop M08-033 along Hwy 169 (Location B, Plate 1); and 3) Outcrop M08-030 along Hwy 169 near the town of Soudan (Location C, Plate 1). Table 3 shows alteration mineral assemblages and NAD 83 UTM coordinates for each location. Tables 4, 5, and 6 list data of percent change in concentration from least altered to altered within samples from outcrops M08-003, M08-030, and M08-033, respectively. The focus of analysis is on M08-003 for two reasons: 1) the location of the gold-mineralized Murray Vein; and 2) the amount of data in relation to M08-030 and M08-033. Discussion on metasomatic changes within samples follows as well as implications for observed changes. Finally, a summary is presented on the findings of lithogeochemical analysis within the Murray Shear Zone hydrothermal system with possible links to similar hydrothermal systems that are gold producing are suggested.

TABLE 3 (next page): Elemental concentrations from each sample. Alteration assemblage indicated at top of table. All data shown in weight percent.

TABLE 3

NAD 83 UTM (E), UTM (N)	MV1 0561550, 5296200	CS-A-1 0561550, 5296200	CS-A-2 0561550, 5296200	CS-A-3 0561550, 5296200	CS-A-4 0561550, 5296203	CS-A-5 0561550, 5296203	CS-A-6 0561550, 5296203	CS-A-7 0561550, 5296203	CS-A-8 0561550, 5296203	CS-B-9 0561550, 5296210	CS-B-10 0561550, 5296210	CS-C-11 0561550, 5296220
Alteration	Qtz Vein	Ank + Ser + Chl + Py	Ank + Ser + Chl + Py	Ank + Ser + Chl + Py	Ank + Ser + Chl + Py	Ank + Ser + Chl + Py	Ank + Ser + Chl + Py	Ank + Ser + Chl + Py	Ank + Ser + Chl + Py	Chl + Act + Ank	Chl + Act + Ank	Chl + Ank
SiO2 (%)	95.37	43.97	48.59	44.93	44.49	52.97	47.71	60.87	45.19	64.4	64.81	62.85
Al2O3 (%)	0.7	8.97	9.66	9.9	15.37	16.52	17.09	17.09	14.59	12.79	12	13.19
Fe2O3(T) (%)	0.99	6.32	7.14	6.64	9.61	8.3	8.73	4.39	10.17	6.8	6.37	7.27
MnO (%)	0.03	0.159	0.185	0.159	0.153	0.116	0.122	0.084	0.156	0.121	0.114	0.115
MgO (%)	0.22	9.07	8.63	9.38	8.15	5.05	6.89	2.65	8.4	4.16	3.74	4.46
CaO (%)	0.44	10.08	8.42	9.32	5.21	3.43	3.76	2.02	6.43	1.77	2.39	2.14
Na2O (%)	0.08	0.17	0.22	0.25	1.19	1.85	0.74	2.11	1.25	3.88	4.03	4.32
K2O (%)	0.16	1.33	1.4	1.15	1.7	2.51	2.96	3.86	1.13	0.41	0.23	0.26
TiO2 (%)	0.015	0.435	0.468	0.464	0.576	0.73	0.699	0.423	1.074	0.874	0.841	0.801
P2O5 (%)	0.03	0.34	0.34	0.36	0.1	0.18	0.17	0.19	0.34	0.2	0.21	0.22
LOI (%)	0.77	17.47	15.31	16.31	12.08	8.25	9.43	5.12	9.93	3.78	3.97	3.85
Total (%)	98.81	98.31	100.3	98.86	98.63	99.9	98.29	98.81	98.66	99.18	98.7	99.47
CO2 (%)	0.61	13.9	12.3	13.6	7.71	4.49	5.14	2.01	4.96	0.89	1.47	1.09
H2O- (%)	< 0.1	0.2	0.4	0.2	0.6	0.5	0.4	0.4	0.4	0.3	0.2	0.1
H2O+ (%)	0.3	3.1	3.4	3.6	4.9	4.2	5.1	3.3	5.7	3.3	2.9	3.4
Total S (%)	< 0.01	0.03	0.02	0.02	0.02	0.05	0.12	0.02	< 0.01	0.02	< 0.01	< 0.01
Ag (ppm)	18.6	< 0.5	< 0.5	< 0.5	< 0.5	< 0.5	< 0.5	< 0.5	< 0.5	< 0.5	< 0.5	< 0.5
As (ppm)	< 0.5	2	4	2	< 0.5	1	3	2	< 0.5	< 0.5	< 0.5	< 0.5
Au (ppm)	6690	<2	<2	<2	<2	<2	<2	<2	<2	<2	<2	<2
Ba (ppm)	25	160	183	147	331	491	538	632	224	123	48	90
Be (ppm)	< 1	1	1	1	1	1	1	1	1	< 1	< 1	1
Bi (ppm)	2.6	< 0.4	1.3	< 0.4	18.3	1.4	< 0.4	246	< 0.4	0.7	< 0.4	< 0.4
Br (ppm)	2	< 0.5	< 0.5	< 0.5	< 0.5	< 0.5	< 0.5	< 0.5	< 0.5	< 0.5	< 0.5	< 0.5
Ce (ppm)	1.2	93	80.1	85.9	14.3	31.5	60.5	53.5	49.6	25.4	33.3	30.5
Co (ppm)	1	37	41	37	44	32	40	20	44	21	19	24
Cr (ppm)	36	626	695	600	298	76	315	116	346	23	10	17
Cs (ppm)	< 0.5	1	0.9	1	1	1.5	1.7	2.3	0.7	0.6	< 0.5	< 0.5
Cu (ppm)	< 10	30	30	30	20	30	50	20	10	20	100	120
Dy (ppm)	< 0.1	2.4	2.2	2.4	1.9	2.3	2.6	1.8	3.3	3.4	2.5	3.3
Er (ppm)	< 0.1	1.1	1.1	1.1	1.2	1.5	1.6	0.9	2.1	2.2	1.7	2.2

TABLE 3 (Continued)

	MVI	CS-A-1	CS-A-2	CS-A-3	CS-A-4	CS-A-5	CS-A-6	CS-A-7	CS-A-8	CS-B-9	CS-B-10	CS-C-11
Eu (ppm)	0.05	1.97	1.94	1.63	0.54	0.84	1.36	0.99	1.36	0.76	0.69	1.13
Ga (ppm)	1	11	13	13	15	16	16	18	17	15	14	13
Gd (ppm)	< 0.1	4.6	4.3	4.5	1.9	2.7	3.5	2.9	4	3.2	2.7	3.3
Ge (ppm)	< 1	< 1	< 1	1	1	1	1	1	1	< 1	< 1	< 1
Hf (ppm)	< 0.2	2.8	3	3.1	1.7	3.5	3	3.4	3.1	3.9	4.1	3.9
Ho (ppm)	< 0.1	0.4	0.4	0.4	0.4	0.5	0.5	0.3	0.7	0.7	0.6	0.7
In (ppm)	< 0.2	< 0.2	< 0.2	< 0.2	< 0.2	< 0.2	< 0.2	< 0.2	< 0.2	< 0.2	< 0.2	< 0.2
Ir (ppm)	< 5	< 5	< 5	< 5	< 5	< 5	< 5	< 5	< 5	< 5	< 5	< 5
La (ppm)	1.4	44.5	38.3	41.5	7.3	16.7	31.5	29.2	23.3	11.8	15.9	14
Lu (ppm)	< 0.04	0.12	0.13	0.13	0.17	0.22	0.24	0.11	0.28	0.3	0.28	0.29
Mo (ppm)	3	< 2	< 2	< 2	< 2	4	< 2	< 2	< 2	< 2	< 2	< 2
Nb (ppm)	1	7	5	7	3	5	6	4	8	7	7	6
Nd (ppm)	0.5	36.3	32.6	33.7	7.2	14.3	22.1	21.6	23	12.3	13.1	14.1
Ni (ppm)	< 20	260	280	240	240	100	260	110	170	40	40	50
Pb (ppm)	58	6	< 5	< 5	< 5	< 5	< 5	11	< 5	< 5	< 5	8
Pr (ppm)	0.12	10.3	10.1	9.75	1.9	3.98	6.41	6.95	6.84	3.1	3.6	3.84
Rb (ppm)	5	32	32	29	39	61	68	93	31	12	5	6
Sb (ppm)	< 0.2	< 0.2	< 0.2	0.2	< 0.2	0.2	0.4	< 0.2	0.6	< 0.2	< 0.2	< 0.2
Sc (ppm)	< 1	14	15	14	18	20	21	8	29	18	16	15
Se (ppm)	< 3	< 3	< 3	< 3	< 3	< 3	< 3	< 3	< 3	< 3	< 3	< 3
Sm (ppm)	0.1	7.2	6.4	6.8	1.7	2.9	4.5	4.1	4.6	3	2.9	3.2
Sn (ppm)	< 1	14	< 1	5	< 1	< 1	1	< 1	1	2	2	1
Sr (ppm)	12	340	304	328	127	99	71	58	101	48	55	85
Ta (ppm)	< 0.1	0.3	0.3	0.3	0.2	0.4	0.5	0.3	0.5	0.5	0.6	0.6
Tb (ppm)	< 0.1	0.5	0.5	0.5	0.3	0.4	0.5	0.3	0.6	0.5	0.4	0.6
Th (ppm)	0.1	5.7	3.8	4.4	0.6	1.8	2.3	3.7	1.1	1.8	2.3	2.4
Tl (ppm)	< 0.1	0.3	< 0.1	0.3	< 0.1	0.1	0.4	0.6	0.1	0.1	< 0.1	< 0.1
Tm (ppm)	< 0.05	0.15	0.15	0.16	0.19	0.22	0.24	0.13	0.3	0.31	0.26	0.33
U (ppm)	< 0.1	1	0.9	0.8	0.2	0.7	0.6	0.7	0.3	0.5	0.5	0.6
V (ppm)	< 5	91	100	100	130	153	134	67	186	116	110	102
W (ppm)	1	6	4	11	7	8	7	5	8	6	5	1
Y (ppm)	< 2	10	11	10	10	11	15	9	16	18	13	19
Yb (ppm)	< 0.1	0.8	0.9	0.9	1.2	1.4	1.5	0.8	1.9	2	1.7	2
Zn (ppm)	< 30	80	60	100	60	50	140	120	190	140	110	130
Zr (ppm)	8	106	100	117	51	117	120	114	119	138	151	145

TABLE 3 (Continued)

NAD 83 UTM (E), UTM (N)	CS-I-19 0559402, 5296398	CS-I-20 0559402, 5296398	CS-I-21 0559402, 5296398	CS-I-22 0559402, 5296398	CS-I-27 0558300, 5296135	CS-I-28 0558300, 5296135	CS-I-29 0558300, 5296135	CS-J-30 0558300, 5296135
Alteration	Ank + Chl + Ser	Ank + Chl + Ser	Ank + Chl + Ser	Qtz Vein	Qtz Vein	Ank + Ser+ Chl +- Py	Ank + Ser+ Chl +- Py	Ank + Ser+ Chl +- Py
SiO2 (%)	52.08	40.75	14.35	69.19	97.83	54.33	58.06	56.61
Al2O3 (%)	14.67	11.71	9.66	0.82	0.57	20.5	15.22	20.17
Fe2O3(T) (%)	7.06	5.62	8.41	0.98	1.04	9.66	14.05	9.03
MnO (%)	0.083	0.123	0.25	0.119	0.008	0.046	0.071	0.04
MgO (%)	7.32	6.53	10.84	0.75	0.15	2.41	3.34	2.08
CaO (%)	3.85	11.47	19.75	15.18	0.07	0.29	0.16	0.16
Na2O (%)	1.58	0.22	0.43	0.05	0.04	0.26	0.17	0.24
K2O (%)	2.64	3.26	1.95	0.21	0.11	5.34	2.8	5.42
TiO2 (%)	0.5	0.388	0.529	0.029	0.029	1.276	0.934	1.222
P2O5 (%)	0.11	0.11	0.03	0.05	0.03	0.22	0.1	0.13
LOI (%)	8.89	18.99	31.8	12.85	0.27	4.48	4.2	4.26
Total (%)	98.78	99.31	98.4	100.2	100.2	98.83	99.1	99.36
CO2 (%)	5.57	18	32	13.2	0.03	0.02	0.03	0.02
H2O- (%)	0.2	0.2	0.2	< 0.1	< 0.1	0.5	0.3	0.4
H2O+ (%)	4.2	2.2	2	0.3	0.3	5	5	4.6
Total S (%)	< 0.01	0.02	0.02	0.01	< 0.01	0.24	0.14	0.03
Ag (ppm)	< 0.5	< 0.5	< 0.5	< 0.5	0.9	< 0.5	< 0.5	0.6
As (ppm)	< 0.5	2	50	< 0.5	3	87	145	296
Au (ppm)	<2	<2	<2	3	3	<2	<2	<2
Ba (ppm)	678	378	78	24	16	954	491	640
Be (ppm)	1	1	< 1	< 1	< 1	3	2	2
Bi (ppm)	35.9	< 0.4	< 0.4	< 0.4	< 0.4	0.4	1.3	4.4
Br (ppm)	< 0.5	< 0.5	< 0.5	1	< 0.5	< 0.5	< 0.5	< 0.5
Ce (ppm)	26	25.7	4.2	18	6.5	22.4	16.1	15.5
Co (ppm)	27	15	38	2	2	65	86	44
Cr (ppm)	233	180	201	24	28	330	230	314
Cs (ppm)	1.9	1.4	1.1	< 0.5	< 0.5	6.8	3.8	6
Cu (ppm)	40	60	10	20	10	30	110	50
Dy (ppm)	2	2	1.1	0.6	0.1	2.7	2	2.2
Er (ppm)	1.3	1.3	0.6	0.4	< 0.1	1.7	1.4	1.6

TABLE 3 (Continued)

	CS-I-19	CS-I-20	CS-I-21	CS-I-22	CS-J-27	CS-J-28	CS-J-29	CS-J-30
Eu (ppm)	0.63	0.69	0.15	0.4	0.12	1.01	0.7	0.6
Ga (ppm)	14	11	9	1	1	21	16	20
Gd (ppm)	2.1	2.1	0.9	0.7	0.3	3	2	2
Ge (ppm)	1	< 1	< 1	< 1	2	2	2	2
Hf (ppm)	2.8	2.1	0.5	< 0.2	< 0.2	2.2	1.9	2.2
Ho (ppm)	0.4	0.4	0.2	0.1	< 0.1	0.5	0.4	0.5
In (ppm)	< 0.2	< 0.2	< 0.2	< 0.2	< 0.2	< 0.2	< 0.2	< 0.2
Ir (ppm)	< 5	< 5	< 5	< 5	< 5	< 5	< 5	< 5
La (ppm)	12.7	12.7	1.9	10.5	3.8	10.1	7.8	7.4
Lu (ppm)	0.18	0.19	0.09	0.05	< 0.04	0.21	0.2	0.23
Mo (ppm)	< 2	< 2	< 2	< 2	< 2	< 2	< 2	< 2
Nb (ppm)	4	4	2	< 1	< 1	5	5	5
Nd (ppm)	10.5	10.6	2.5	5	2.4	12.1	8.2	8.2
Ni (ppm)	110	80	140	20	< 20	140	240	110
Pb (ppm)	< 5	< 5	< 5	< 5	< 5	< 5	< 5	5
Pr (ppm)	3.09	3.06	0.54	1.69	0.71	3.06	2.17	2.15
Rb (ppm)	56	71	38	5	3	179	97	175
Sb (ppm)	< 0.2	< 0.2	< 0.2	< 0.2	< 0.2	0.3	< 0.2	< 0.2
Sc (ppm)	17	13	19	3	< 1	36	26	34
Se (ppm)	< 3	< 3	< 3	< 3	< 3	< 3	< 3	< 3
Sm (ppm)	2.3	2.2	0.7	0.9	0.4	2.9	1.9	1.8
Sn (ppm)	< 1	< 1	3	< 1	< 1	3	2	< 1
Sr (ppm)	93	75	119	104	3	18	11	13
Ta (ppm)	0.4	0.3	< 0.1	< 0.1	< 0.1	0.3	0.3	0.3
Tb (ppm)	0.3	0.3	0.2	< 0.1	< 0.1	0.5	0.3	0.3
Th (ppm)	2.1	1.7	0.3	0.1	0.2	0.6	0.6	0.6
Tl (ppm)	0.1	< 0.1	< 0.1	< 0.1	< 0.1	0.7	0.6	0.9
Tm (ppm)	0.19	0.19	0.09	0.05	< 0.05	0.25	0.2	0.25
U (ppm)	0.5	0.4	0.1	< 0.1	< 0.1	0.2	0.2	0.4
V (ppm)	109	86	149	7	5	278	206	262
W (ppm)	1	2	< 1	< 1	2	29	6	3
Y (ppm)	10	12	4	4	< 2	15	11	11
Yb (ppm)	1.2	1.2	0.6	0.3	< 0.1	1.5	1.3	1.6
Zn (ppm)	40	< 30	< 30	< 30	< 30	80	140	100
Zr (ppm)	99	73	15	13	5	73	65	71

3.4.1 Analysis at the Murray Vein (Outcrop M08-003)

Figure 34 illustrates the isocon analysis in the vicinity of the Murray Vein at location A (Plate 1). Refer back to Figure 21 for location of samples within the outcrop and in relation to the Murray Vein. The results of mass balance analysis are included in Table 4. Relative to a least altered sample (CS-C-11, Data K) numerous geochemical changes exist within outcrop M08-003. The least altered sample is located farthest away from the Murray Vein at this sample location, and shows no signs of deformation and/or alteration as present in closer proximity to the Murray Vein. Both field mapping and trace element lithogeochemical characteristics indicate that the rocks at this location shared a common protolith. If this is the case, the vein forming event brought about a distinct alteration type to the outcrop as evident in geochemical signatures.

In broad terms, certain elements increase while others decrease in concentration in sample data leading up to the vein. Elements that are gained or lost have percentages greater than 5% from the best fit isocon. Those elements characterized as "immobile" have gains or losses less than 5 % based on isocon analysis.

The closest sample to the vein, CS-A-3, shows a depletion in elements SiO_2, Al_2O_3, Na_2O, TiO_2, Cu, and Zn among others. Gained species within the outcrop approaching the vein include MgO, Fe_2O_3, MnO, CaO, K_2O, CO_2, Ba, Co, Cr, Ni, Rb, Sr, V, and W. Notable gains include Cr (5004 %), K_2O (572 %), and Ni (599 %). Notable losses include Na_2O (-93 %), Cu (-68 %), and Sn (-100 %).

When plotted on a bar graph concentrations of SiO_2 and CO_2 show inverse relationships to each other (Figure 35a and 36a). A decrease in silica concentration leading up to the vein corresponds to an increase in carbon dioxide. This relationship occurs in outcrop M08-030 and M08-033 as well, but is best documented here due to a larger data set. True gains or losses of elements within a sample must be in relation to the isocon as previously outlined and determined. Figure 35b and 36b show percent change in concentration from a least altered sample with respect to the best-fit isocon. In Figure 35b, both silica depletion and silica addition appear to be present with respect to a Zr-Hf isocon. Figure 36b shows strong carbon dioxide increases approaching the vein in relation to the isocon.

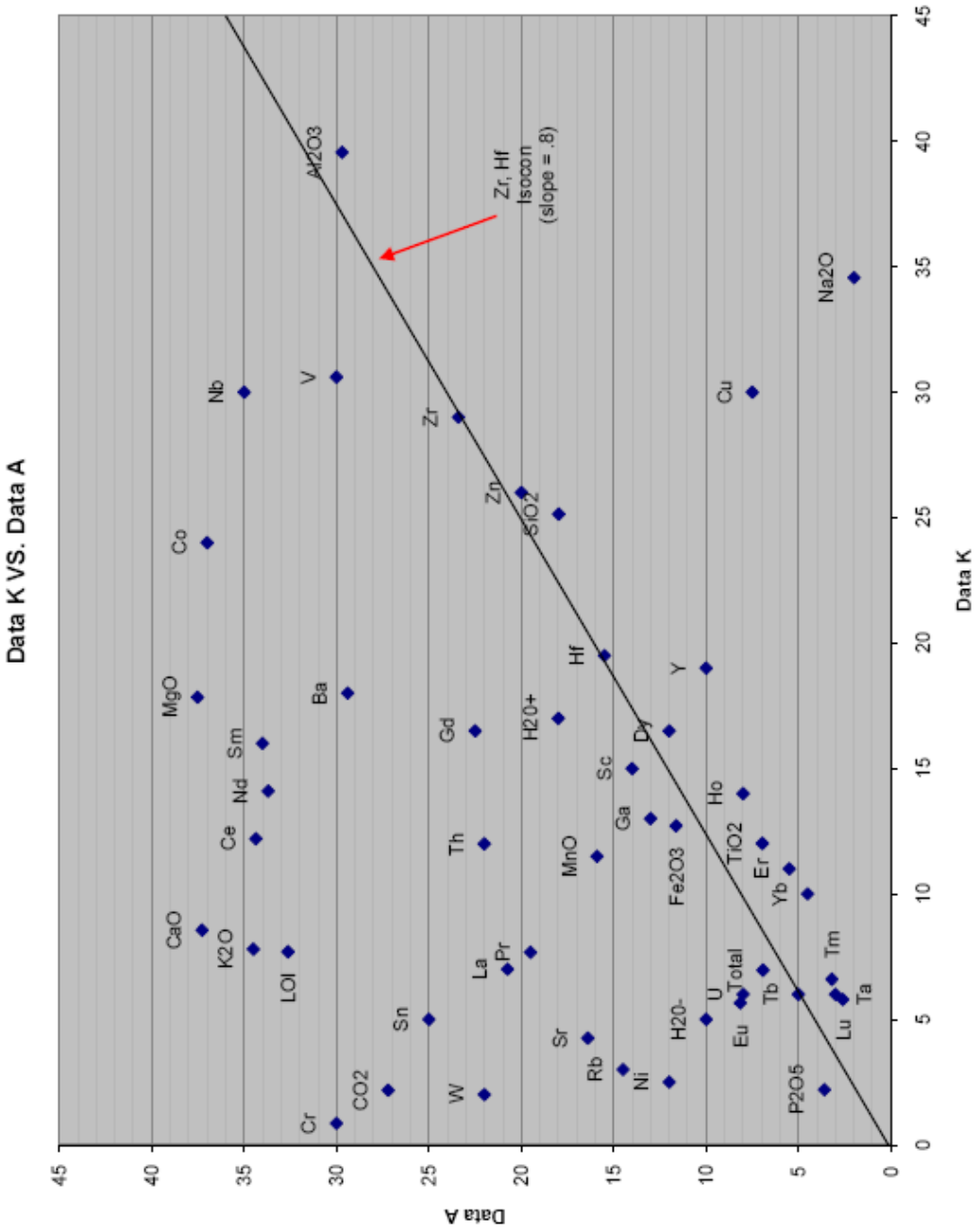

Figure 34: Element concentration of samples from the Murray Vein outcrop (M08-003). The isocon shown as a line from the origin. Elements that plot above the isocon increase in concentration from least altered (Data K) to altered (Data A). Refer to Table 5 for data.

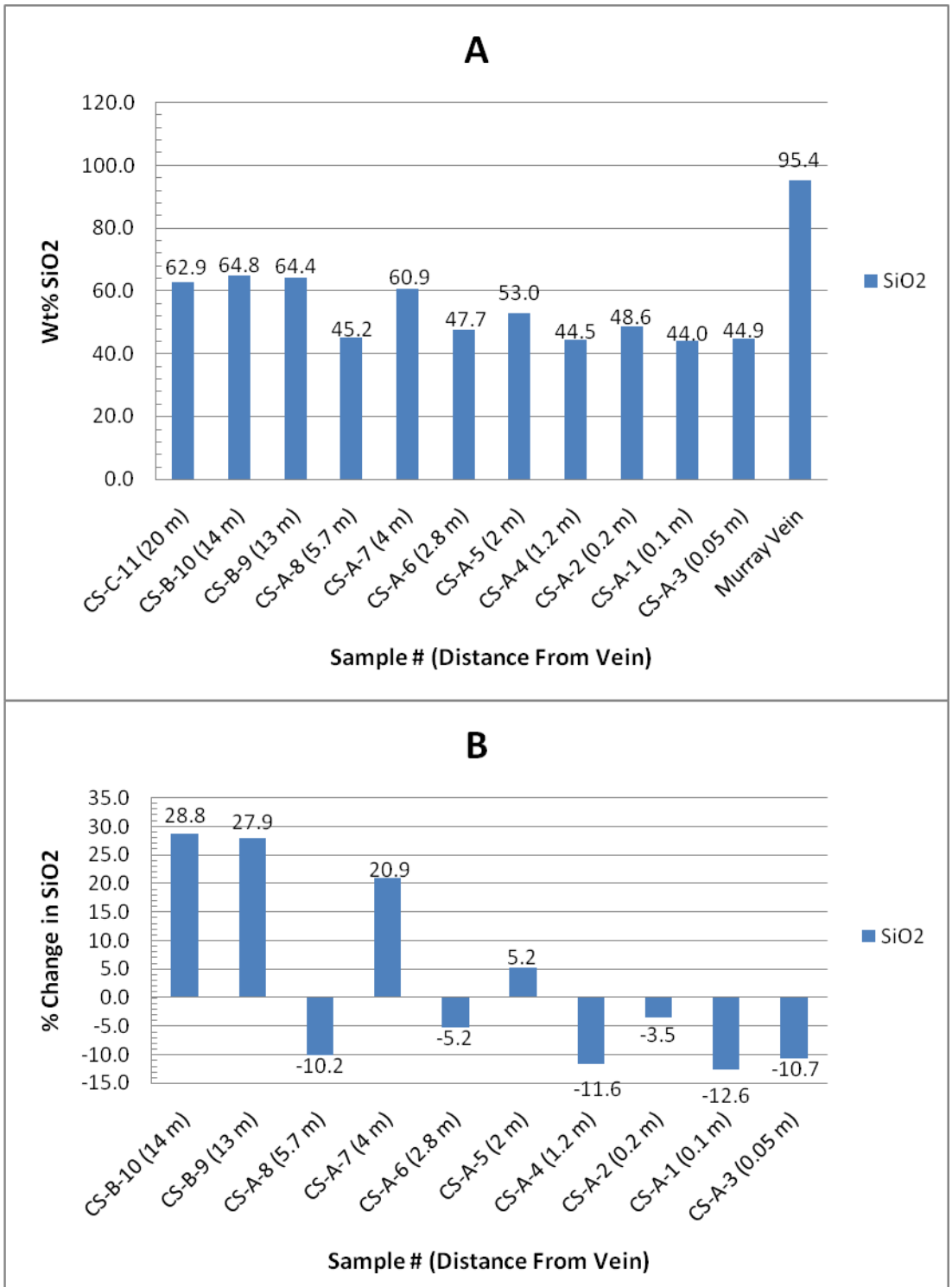

Figure 35: SiO_2 data from outcrop M08-003. **A)** Weight percent concentration of SiO_2 for each sample including the Murray Vein. **B)** Percent change in SiO_2 concentration relative to the least altered sample, CS-C-11.

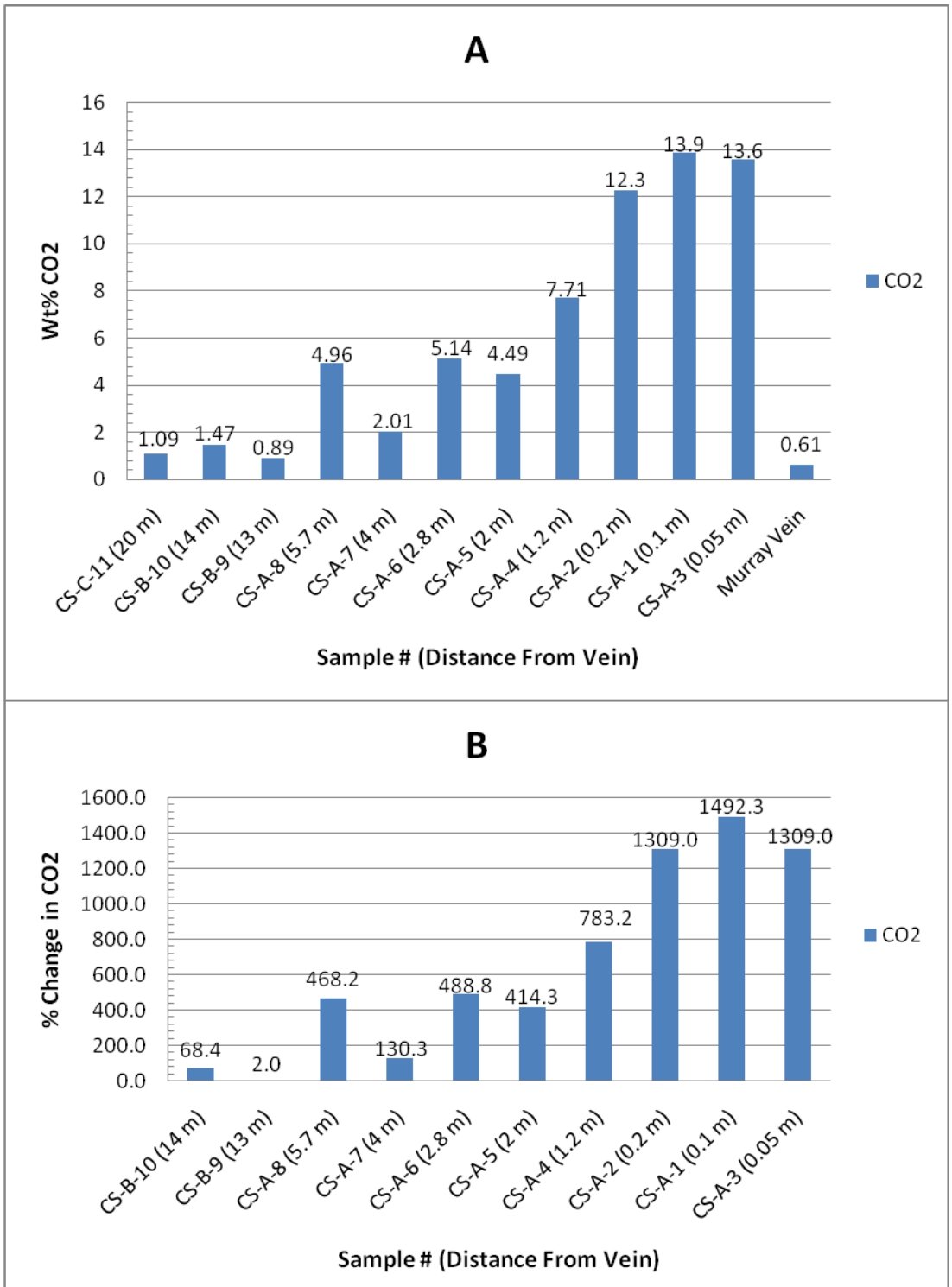

Figure 36: CO_2 data from outcrop M08-003. **A)** Weight percent concentration of CO_2 for each sample including the Murray Vein. **B)** Percent change in CO_2 concentration relative to the least altered sample, CS-C-11.

MURRAY VEIN OUTCROP

	Least Altered	% change relative to least altered, sample CS-C-11											Most Altered
Dist_Vein (m)	K 20	J (Δ%) 14	I (Δ%) 13	H(Δ%) 5.7	G (Δ%) 4	F (Δ%) 2.8	E (Δ%) 2	D(Δ%) 1.2	C(Δ%) 0.2	B (Δ%) 0.1	A (Δ%) 0.05
COMPT	CS-C-11	CS-B-10	CS-B-9	CS-A-8	CS-A-7	CS-A-6	CS-A-5	CS-A-4	CS-A-2	CS-A-1	CS-A-3
SiO2	62.85	28.76	27.94	-10.22	20.93	-5.22	5.23	-11.61	-3.47	-12.65	-3.47
Al2O3	13.19	13.60	21.08	38.11	61.78	61.78	56.39	45.50	-8.55	-15.09	-8.55
Fe2O3	7.27	9.40	16.79	74.67	-24.60	49.94	42.55	65.05	22.63	8.55	22.63
MnO	0.115	23.78	31.38	69.38	-8.80	32.46	25.95	66.12	100.86	72.64	100.86
MgO	4.46	4.70	16.46	135.17	-25.81	92.89	41.38	128.17	141.61	153.92	141.61
CaO	2.14	39.45	3.27	275.17	17.86	119.38	100.13	203.99	391.28	488.14	391.28
Na2O	4.32	16.48	12.14	-63.87	-39.01	-78.61	-46.53	-65.61	-93.64	-95.09	-93.64
K2O	0.26	10.45	96.90	442.67	1753.72	1321.51	1105.40	716.41	572.33	538.72	572.33
TiO2	0.801	31.10	36.24	67.42	-34.06	8.96	13.79	-10.21	-27.05	-32.19	-27.05
P2O5	0.22	19.19	13.51	92.97	7.84	-3.52	2.16	-43.24	92.97	92.97	92.97
LOI	3.85	28.75	22.59	222.05	66.05	205.83	167.56	291.77	396.53	466.58	396.53
Total	99.47	23.90	24.50	23.85	24.03	23.38	25.40	23.81	25.90	23.41	25.90
CO2	1.09	68.39	1.95	468.18	130.25	488.80	414.34	783.20	1308.99	1492.28	1308.99
H2O-	0.1	149.72	274.59	399.45	399.45	399.45	524.31	649.17	399.45	149.72	399.45
H2O+	3.4	6.50	21.19	109.33	21.19	87.29	54.24	79.95	24.86	13.84	24.86
Ba	90	-33.41	70.64	210.77	776.81	646.40	581.19	359.21	153.89	121.98	153.89
Ce	30.5	36.32	3.98	103.05	119.02	147.68	28.96	-41.46	227.92	280.73	227.92
Co	24	-1.15	9.25	128.91	4.05	108.10	66.48	128.91	113.31	92.50	113.31
Cr	17	-26.55	68.93	2441.31	752.00	2213.62	458.21	2088.76	5004.65	4497.86	5004.65
Cu	120	4.05	-79.19	-89.59	-79.19	-47.97	-68.78	-79.19	-68.78	-68.78	-68.78
Dy	3.3	-5.41	28.65	24.86	-31.89	-1.62	-12.97	-28.11	-16.76	-9.19	-16.76
Er	2.2	-3.52	24.86	19.19	-48.92	-9.19	-14.87	-31.89	-37.57	-37.57	-37.57
Eu	1.13	-23.76	-16.02	50.28	9.39	50.28	-7.18	-40.33	114.36	117.68	114.36
Ga	13	34.47	44.07	63.28	72.89	53.68	53.68	44.07	24.86	5.65	24.86
Gd	3.3	2.16	21.08	51.35	9.73	32.43	2.16	-28.11	62.70	74.05	62.70
Hf	3.9	31.27	24.86	-0.75	8.85	-3.95	12.06	-45.57	-3.95	-10.36	-3.95
Ho	0.7	7.02	24.86	24.86	-46.49	-10.81	-10.81	-28.65	-28.65	-28.65	-28.65
La	14	41.81	5.24	107.81	160.43	180.94	48.94	-34.89	241.59	296.88	241.59
Lu	0.29	20.56	29.17	20.56	-52.64	3.33	-5.28	-26.81	-44.03	-48.33	-44.03
Nb	6	45.67	45.67	66.48	-16.76	24.86	4.05	-37.57	4.05	45.67	4.05
Nd	14.1	16.01	8.92	103.68	91.28	95.71	26.63	-36.24	188.69	221.45	188.69
Ni	50	-0.11	-0.11	324.53	174.70	549.28	149.72	499.34	599.23	549.28	599.23
Pr	3.84	17.06	0.80	122.41	125.99	108.43	29.41	-38.22	228.41	234.92	228.41
Rb	6	4.05	149.72	545.12	1835.36	1315.10	1169.43	711.60	565.93	565.93	565.93
Sc	15	33.19	49.83	141.40	-33.41	74.81	66.48	49.83	24.86	16.54	24.86
Sm	3.2	13.16	17.06	79.49	59.98	75.59	13.16	-33.67	149.72	180.94	149.72
Sn	1	149.72	149.72	24.86	-100.00	24.86	-100.00	-100.00	-100.00	1648.07	-100.00
Sr	85	-19.21	-29.49	48.37	-14.80	4.30	45.43	86.56	346.57	399.45	346.57
Ta	0.6	24.86	4.05	4.05	-37.57	4.05	-16.76	-58.38	-37.57	-37.57	-37.57
Tb	0.6	-16.76	4.05	24.86	-37.57	4.05	-16.76	-37.57	4.05	4.05	4.05
Th	2.4	19.66	-6.35	-42.77	92.50	19.66	-6.35	-68.78	97.70	196.55	97.70
Tm	0.33	-1.62	17.29	13.51	-50.81	-9.19	-16.76	-28.11	-43.24	-43.24	-43.24
U	0.6	4.05	4.05	-37.57	45.67	24.86	45.67	-58.38	87.29	108.10	87.29
V	102	34.66	42.00	127.69	-17.98	64.03	87.29	59.14	22.41	11.40	22.41
W	1	524.31	649.17	898.90	524.31	774.03	898.90	774.03	399.45	649.17	399.45
Y	19	-14.57	18.29	5.15	-40.85	-1.42	-27.71	-34.28	-27.71	-34.28	-27.71
Yb	2	6.13	24.86	18.62	-50.06	-6.35	-12.60	-25.08	-43.81	-50.06	-43.81
Zn	130	5.65	34.47	82.49	15.26	34.47	-51.98	-42.37	-42.37	-23.16	-42.37
Zr	145	30.03	18.83	2.47	-1.83	3.33	0.75	-56.08	-13.89	-8.72	-13.89

Table 4: Metasomatic changes based on a best fit isocon analysis with respect to varying distances to the vein and alteration mineral assemblages. Each shaded column is percent change in concentration from least altered sample (unshaded column).

OUTCROP M08-030

% change relative to least altered, sample CS-J-30

	A	B (Δ%)	C (Δ%)
Dist_Vein (m)	3	0.1	0.05
COMP'T	CS-J-30	CS-J-29	CS-J-28
SiO2	56.61	24.39	16.40
Al2O3	20.17	-8.48	23.27
Fe2O3	9.03	88.71	29.75
MnO	0.04	115.28	39.48
MgO	2.08	94.75	40.53
CaO	0.16	21.28	119.83
Na2O	0.24	-14.09	31.39
K2O	5.42	-37.34	19.49
TiO2	1.222	-7.30	26.64
P2O5	0.13	-6.70	105.25
LOI	4.26	19.58	27.55
Total	99.36	20.97	20.64
CO2	0.02	81.93	21.28
H20-	0.4	-9.04	51.61
H20+	4.6	31.83	31.83
S	0.03	465.99	870.27
Ag	0.6	-100.00	-100.00
As	296	-40.59	-64.35
Ba	640	-6.95	80.79
Be	2	21.28	81.93
Bi	4.4	-64.17	-88.97
Ce	15.5	25.98	75.28
Co	44	137.06	79.17
Cr	314	-11.16	27.46
Cs	6	-23.19	37.46
Cu	50	166.83	-27.23
Dy	2.2	10.26	48.85
Er	1.6	6.12	28.86
Eu	0.6	41.50	104.16
Ga	20	-2.97	27.35
Gd	2	21.28	81.93
Ge	2	21.28	21.28
Hf	2.2	4.75	21.28
Ho	0.5	-2.97	21.28
La	7.4	27.84	65.54
Lu	0.23	5.46	10.74
Nb	5	21.28	21.28
Nd	8.2	21.28	78.97
Ni	110	164.62	54.36
Pb	5	-100.00	-100.00
Pr	2.15	22.41	72.62
Rb	175	-32.77	24.06
Sc	34	-7.25	28.42
Sm	1.8	28.02	95.40
Sr	13	2.63	67.93
Ta	0.3	21.28	21.28
Tb	0.3	21.28	102.14
Th	0.6	21.28	21.28
Tl	0.9	-19.14	-5.67
Tm	0.25	-2.97	21.28
U	0.4	-39.36	-39.36
V	262	-4.64	28.69
W	3	142.57	1072.41
Y	11	21.28	65.39
Yb	1.6	-1.46	13.70
Zn	100	69.80	-2.97
Zr	71	11.03	24.70

TABLE 5

OUTCROP M08-033

% change relative to least altered, sample CS-I-19

	A	B (Δ%)	C (Δ%)
Dist_Vein (m	10.00	0.02	0.10
COMP'T	CS-I-19	CS-I-20	CS-I-21
SiO2	52.08	2.70	-63.83
Al2O3	14.67	4.77	-13.57
Fe2O3	7.06	4.48	56.36
MnO	0.083	94.51	295.35
MgO	7.32	17.09	94.37
CaO	3.85	291.04	573.33
Na2O	1.58	-81.72	-64.28
K2O	2.64	62.08	-3.05
TiO2	0.5	1.86	38.87
P2O5	0.11	31.26	-64.20
LOI	8.89	180.38	369.51
Total	98.78	31.96	30.75
CO2	5.57	324.17	654.08
H20-	0.2	31.26	31.26
H20+	4.2	-31.25	-37.50
Ba	678	-26.82	-84.90
Be	1	31.26	-100.00
Bi	35.9	-100.00	-100.00
Ce	26	29.74	-78.80
Co	27	-27.08	84.73
Cr	233	1.40	13.23
Cs	1.9	-3.28	-24.01
Cu	40	96.88	-67.19
Dy	2	31.26	-27.81
Er	1.3	31.26	-39.42
Eu	0.63	43.76	-68.75
Ga	14	3.13	-15.62
Gd	2.1	31.26	-43.75
Ge	1	-100.00	-100.00
Hf	2.8	-1.56	-76.56
Ho	0.4	31.26	-34.37
La	12.7	31.26	-80.36
Lu	0.18	38.55	-34.37
Nb	4	31.26	-34.37
Nd	10.5	32.51	-68.75
Ni	110	-4.54	67.05
Pr	3.09	29.98	-77.06
Rb	56	66.41	-10.93
Sc	17	0.37	46.70
Sm	2.3	25.55	-60.05
Sr	93	5.85	67.95
Ta	0.4	-1.56	-100.00
Tb	0.3	31.26	-12.50
Th	2.1	6.26	-81.25
Tl	0.1	-100.00	-100.00
Tm	0.19	31.26	-37.83
U	0.5	5.01	-73.75
V	109	3.56	79.42
W	1	162.51	-100.00
Y	10	57.51	-47.50
Yb	1.2	31.26	-34.37
Zn	40	-100.00	-100.00
Zr	99	-3.21	-80.11

TABLE 6

Table 5 and Table 6 (above): Metasomatic changes based on best fit isocon analysis with respect to varying distances to the vein and alteration assemblages. Each shaded column is percent change in concentration from least altered sample (unshaded column).

3.4.2 Analysis at Outcrop M08-033

Isocon analysis was not performed at this location because lithogeochemical evidence suggests that two different protoliths were sampled at this location. Isocon analysis using two different protoliths is not a proper use of the method.

3.4.3 Analysis at Outcrop M08-030

Within outcrop M08-030 many changes are apparent with respect to the least altered sample. Table 5 displays data of percent change in concentration from the least altered sample, CS-J-30. Elements lost approaching the vein include SiO_2, As, Ba, Cr, Ni, Rb, Sc, V, and Zn. Gained elements include Al_2O_3, Fe_2O_3, MnO, MgO, CaO, Na_2O, K_2O, TiO_2, P_2O_5, CO_2, Co, Cs, S, Sm, Sr, Th, W, and Y among others. Large changes in concentration levels are apparent in elements studied in this sample. Gains of elements include Fe_2O_3 (+56 %), MnO (+295 %), MgO (+94 %), CaO (+573 %), CO_2 (+654 %), Co (+84 %), and Ni (+67 %) among others. Losses of elements include Na2O (-64 %), Ba (-84 %), Ce (-78 %), and Cu (-67 %) among others. Small changes in K_2O (-3 %) and Cr (+ 13%) are interesting in that they do not match concentration patterns of outcrop M08-003. Silica depletion and carbonation exist in accordance with outcrop M08-003.

3.5 Summary of Mass Balance Analysis

Relative to a least altered sample numerous geochemical trends appear to exist. In general, these trends indicate:

- *SiO_2 depletion approaching mineralized veins.* This pattern is only slightly similar to the "gull wing" diagram of Boyle (1955). Although the data show a decrease in silica when evaluated by isocon analysis, the decrease is minor. SiO_2 concentrations and observed wall rock inclusions parallel to vein walls may indicate an episodic vein opening in which silica migrated to vein centerlines but most likely silica came in from a deep fluid source.
- *CO_2 enrichment approaching the Murray Vein and the quartz vein in outcrop M08-033.* Carbonation is well documented in outcrops M08-003 and M08-033. Increasing CO_2 is thought to occur as a consequence of inorganic carbon rich fluids upwelling from a deep source during the vein forming event.
- *Inverse concentration trend in Na and Ca approaching quartz veins.* Likely the result of the breakdown of plagioclase feldspar during hydrothermal metasomatism. This is clearly shown in at outcrop M08-003.
- *Increasing Ca also attributed to carbonatization of the rocks, possibly during the same vein-forming event that depleted SiO_2.* This is further evidenced by the large increases in Sr, Ba, and Eu, which substitute for Ca in carbonates. Increasing Mg, Mn, and especially Ca towards a quartz

vein is indicative of varying substitution of these elements in the Fe-structural position in ankerite as noticed in hand sample, although Fe concentrations vary. This concept is illustrated in all three outcrops.

- *Increasing Mg, Fe, and H_2O correspond to chloritization, which occurs ubiquitously in the area.* Increases in MgO + Fe2O3 are related to increases in chlorite approaching the vein.
- *Variance in Al.* The variance in Al concentration is attributed to Al-Si-O reacting with K to make sericite, a fine-grained muscovite. Sericite is commonly associated with gold mineralization in mesothermal systems. For example, gold-bearing quartz veins in the Murray Shear Zone associate with carbonate + sericite ± green mica schist. Sericitization is further exemplified by the large increase in Ba, Rb, H_2O, and K approaching the vein. The maximum concentration levels of these elements are about half way between the vein and the least altered sample. However, this is only apparent in outcrop M08-003. Outcrop M08-030 shows an inverse to that relationship. Layered stratigraphy of different geochemical signatures may account for these irregularities.
- *Increases in Co, Cr, V, and Ni.* The rather large increase in Cr suggests that the green mica present in the rocks is fuchsite ($K(Al,Cr)_3Si_3O_{10}(OH)_2$). Increasing V suggests another green mica, roscoelite ($K(V,Al_2)AlSi_3O_{10}(OH)_2$), may be present. These minerals are an established guide to mesothermal gold deposits and are a common gangue mineral. There may be substitution of Cr and V for Al in the

octahedral sites of muscovite/sericite as well. The increases in these minerals exist in outcrop M08-003 which, consequently, yields the highest gold values by 3 orders of magnitude.

- *Zn decrease.* Decreasing Zn is related to the pH of the fluid as its concentration is very dependent on acidity. Low Zn values also indicate the paucity of sphalerite in the rocks. This is interesting in that the nearby Fivemile Lake VMS prospect has Zn in quartz veins (Hudak et al., 2002b). Decreasing Zn is apparent in all three outcrops.

In summary, future gold prospects within the Murray Shear Zone region may possess similar identifiers or signatures based on this geochemical investigation. A plausible method of approach might be to look for rocks adjacent to quartz veins in that are low in SiO_2, Zn, and Na. These outcrops should also have high concentrations of CO_2, Al, K, Mg, Fe, Ca, Co, Cr, and V. Minerals to identify in hand sample that represent the unique style of mineralization in the Murray Shear Zone include sericite, chlorite, green mica, and Fe carbonate ± tourmaline ± sulfides.

3.6 Discussion

Lithogeochemical analysis of rocks within the Murray Shear Zone introduces a question as to how these data relate to findings from other known Archean mesothermal gold deposits in greenschist facies environments. Ore and geochemical relations exist in

the context of ore grades and indicator minerals, but differences exist as well. For example, based on the compilation work of Groves (1993) for the crustal continuum model: 1) the deposits have consistent enrichments in Au, normally 10^3-10^4 times background, Ag, As, and W, with variable enrichments in Bi, Sb, Te, B, and Pb, and minor enrichments in Cu and Zn (clearly Bi, Cu, Te and Zn enrichments are not present in the Murray Shear Zone); 2) the alteration assemblages are characteristically enriched in CO_2, S, K, among other LILE; and 3) a fluid that is common to all deposits and is of low salinity with the components H_2O-CO_2-CH_4. The Murray Shear Zone shares some characteristics of known mesothermal gold deposits including major element and lithophile components and Au enrichments. However, many of the ore minerals are either not present or depleting in proximity to a quartz vein.

Other common features of mesothermal gold deposits are ankeritized rock, potassic alteration, and a diverse suite of associated minerals like pyrite, variable arsenopyrite, chalcopyrite, tourmaline, and Cr-V-Ba muscovite (fuchsite-mariposite) (e.g. eastern Campbell-Red Lake, and Golden Mile deposits). Tungsten is characteristic of deposits such as the central Otago lodes, New Zealand, Hollinger-McIntyre, Abitibi subprovince, and Moose River, Meguma terrane (Goldfarb, 2005). Within the Murray Shear Zone tungsten shows large increases in outcrops M08-003 and M08-030. Bismuth-bearing mineral phases are recognized in mesothermal gold deposits although not so in this study. Common gangue phases in most gold deposits in metamorphic rocks are quartz, albite, white/green mica, chlorite, tourmaline, biotite, and carbonate minerals. Likewise, rocks within the Murray Shear Zone are enriched in these minerals.

V. INTERPRETATION

Known gold deposits within granite greenstone terranes of the Superior province of North America are associated with structural architecture that provides a setting for fluid transportation and mineral deposition. In the Superior craton, the largest and most gold-productive structural zones include the Porcupine-Destor and Larder Lake-Cadillac breaks of the Abitibi Greenstone Belt, Canada. Most of the gold is concentrated within narrow rich belts of the Abitibi (TVGB) and Uchi (RPGB) subprovinces (Plate 1, Figure 1). Belts of lode gold deposits can occur in all rock types in greenstone belts but three lithologies host the majority of large deposits: 1) iron-rich mafic igneous rocks, such as tholeiitic basalt; 2) iron-rich clastic metasedimentary rocks and banded iron formation (BIF); 3) and dioritic to felsic phorphyritic stocks and dikes (Robert et al., 2005). Located within the southern reaches of the Superior craton, the Murray Shear Zone of northeastern Minnesota is defined by similar age, structure, and host rock lithology to Canadian gold-hosting greenstone terrains. This investigation of the Murray Shear Zone attempts to better understand unique characteristics shared with gold-rich belts in Canada, and the paucity of developed gold districts in northeastern Minnesota.

1. Structural Architecture

Investigation within the Murray Shear Zone reveals steep-plunging mineral lineations within steeply dipping foliation. Strain partitioning into constricted bands of metamorphic foliation follows an anastomozing network. F_m diverge around coherent lithologic blocks while keeping with a curvilinear E-W trajectory. Strain heterogeneity, possibly resulting from a rheological contrast among various lithologies, occurs where

rocks experience extensive silica alteration. Brittle deformation features are present as in the case of dilational quartz veins, which commonly crosscut ductile features. F_m and L_e highlight sub-horizontal shortening of the crust accompanied by sub-vertical extrusion. Brittle-ductile features within an anastomozing network are similar to features associated with known mesozonal gold deposits (e.g. Sigma-Lamaque, Abitibi GB).

2. Microstructures and Kinematics

Kinematic study of microstructures uncovers evidence of flattening strain and dip-slip shear as evident by: 1) sub-vertical F_m; 2) sub-vertical L_e; 3) asymmetric fabric oriented in a sub-vertical cross-cutting motion plane; 4) sub-horizontal dilational veins; and 5) boudinaged veins and crystals oriented sub-vertically. These elements of macro- and microstructural fabric call upon discrete strain axis orientations and therefore describe a particular deformation event(s). Microstructural features within the Murray Shear Zone are interpreted to represent dominant horizontal contraction and dip-slip shear, which leads to vertical extrusion of the crust within localized zones of weakness. Strike-slip shear is not part of Murray Shear Zone deformation history.

3. Geochemistry

Relative to least altered samples numerous geochemical changes exist. Among the most striking examples of geochemical changes are the presence of alteration envelopes, which help locate a possible gold deposit, and the changes in concentration of SiO_2 and CO_2 adjacent to mineralized veins. Alteration envelopes approaching mineralized quartz veins include chlorite schist, carbonate-chlorite schist, and carbonate-sericite-green mica schist. Enrichment of CO_2 adjacent to mineralized quartz veins may

be the product of a hot, high-pressure CO_2-rich fluid that permeated local lithology during a vein-forming deformational event. The inverse solubility relationships between SiO_2 and CO_2 help explain why the hot saturated fluid from depth would expel CO_2 and leach SiO_2 during its accent. Hot fluids tend to dissolve SiO_2 which is precipitated upon cooling, whereas cold fluids dissolve CO_2 which is precipitated upon heating. However, pressure also plays a critical role in solubility. High-pressure fluids have an easier time transporting ions as in the case of CO_2. This mobilization of fluid could have occurred as a consequence of regional scale contraction and metamorphism. Upon the opening of a dilational vein drops in pressure occur which have dramatic consequences on transported ion species. In the cases studied here, a combination of changes in both temperature and pressure affect localized areas within the Murray Shear Zone. A third variable to fluid transportation and precipitation is the composition of host rock. The composition of rocks containing mineralized quartz veins within the Murray Shear Zone vary from andesite to basalt with no observed ultra mafic rocks. Iron Formation is abundant within the study area and may affect mineralization. However, it is believed that the governing processes are pressure and temperature considering the distances between iron formation and gold mineralization within outcrop.

4. Discussion

The Murray Shear Zone contains structural, kinematic, and lithogeochemical signatures that appear to closely resemble known Archean mesozonal gold deposits. Steep foliation and lineation formed during horizontal shortening, dip-slip shearing and subsequent vertical extrusion. Brittle fracture networks host mineralized veins in

portions of the study area, which may indicate a more extensive network at depth (Figure 37). As a start to further gold exploration it is suggested here that drilling a gold-bearing quartz vein and following it to depth might be effective. Geochemical data show zones of hydrothermal alteration enclosing gold-bearing quartz veins of anomalous gold mineralization in regionally-prevalent greenschist grade metamorphism. Zones of widespread carbonate alteration (adjacent to regional structures) should be identified and used to focus subsequent exploration (Peterson and Patelke, 2004). Carbonate from a CO_2-rich Archean environment could have infiltrated the rocks during deformation and metamorphism (Ericksen, 2008). Intense carbonate alteration changes the rheology of a rock by increasing its strength and tendency towards brittle deformation (Sibson et al., 1988). However, the two deposit types may not be spatially interdependent. More structural and geochemical work within the Murray Shear Zone will further help to advance our understanding of its geologic history and mineral potential.

5. Conclusion

Epigenetic gold mineralization along the Murray Shear Zone came late in the shear zone during dilational veining in a fault-valve cycle. Fluids from proximal and sub-lateral sources within the study area deposited gold in veins. Fluids were generated from two possible sources. One possible source is late intruding felsic porphyries (feldspar porphyry and quartz-feldspar porphyry) in the Fivemile Lake Sequence, the tonalitic Purvis Pluton, and Giants Range Batholith. A second possible source may be dewatering from metamorphism in a convergent margin tectonic regime. Gold sources within the Murray Shear Zone may be the roots of an eroded and exhumed VMS system,

although VMS in mafic dominated systems such as in the Vermilion District are generally gold poor. On the other hand, felsic intrusions within the study area may be the contributing factor for gold, heat, and fluids creating convecting cells. These convecting cells may have been active during progressive deformation, which subsequently created the Murray Shear Zone.

Figure 37: Schematic illustration of a hypothetical cross section through the Murray Shear Zone. Mineralized veins are shown in red, Fm is shown in black lines. Two lithologies represented although thought to be independent of gold mineralization processes.

VI. REFERENCES

Andrews, A.J., Hugon, H., Durocher, M.E., Corfu, F., Lavigne, M.J., 1986. The anatomy of a gold-bearing greenstone belt, Red Lake, northwestern Ontario, Canada. In: Macdonald, A.J., (editor), Gold '86: Willowdale, Ontario, Konsult Internat., Inc., pp. 3-22.

Bauer, R.L., 1985. Correlation of early recumbent and younger upright folding across the boundary between an Archean gneiss belt and greenstone terrane, northeastern Minnesota: Geology, v. 13 pp. 657-660.

Berthe, D., Choukroune, P., Jegouzo, P., 1979. Orthogness, mylonite, and non coaxial deformation of granites: the example of the South Armorican Shear Zone. J. Struct. Geol. Vol. 1, pp. 31-42.

Boerboom, T.J., Zartman, R.E., 1993. Geology, geochemistry, and geochronology of the central Giants Range Batholith, northeastern Minnesota, Canadian Journal of Earth Sciences, v. 30, no. 12, pp. 2510-2522.

Boyle, R.W., 1955. The geochemistry and origin of the gold-bearing quartz veins and lenses of the Yellowknife greenstone belt. Economic Geology, v. 50, pp. 51-66.

Boyle, R.W., 1976. Mineralization processes in Archean greenstone and sedimentary belts: Canada Geol. Survey Paper 75-15, 45 p.

Colvine, A.C., Andrews, A.J., Cherry, M.E., Durocher, M.E., Fyon, A.J., Lavigne, M.N., MacDonald, A.J., Marmont, S., Poulsen, K.H., Springer, J.S., Troop, D.G., 1984. An integrated model for the origin of Archean lode gold deposits: Ontario Geol. Survey Open-File Rept. 5524, 98 p.

Colvine, A.C., 1989. An Empirical Model for the Formation of Archean Gold Deposits: Products of Final Cratonization of the Superior Province, Canada, In: Keays, R.R., Ramsay, W.R.H., Groves, D.I., (editors), Econ. Geol. Monograph 6, The Geology of Gold Deposits: The Perspective in 1988, The Economic Geology Publishing Company, pp. 37-53.

Dube, B., Gosselin, P., 2007. Greenstone-Hosted Quartz-Carbonate Vein Deposits, In: Goodfellow, W.D. (editor), Mineral Deposits of Canada: A synthesis of Major Deposit-Types, District Metallogeny, the Evolution of Geological Provinces, and Exploration Methods: Geological Association of Canada, Mineral Deposits Division, Special Pub. No. 5, pp. 49-73.

Foster, R.P., Wilson, J.F., 1984. Geological setting of Archaean gold deposits in Zimbabwe, In: Foster, R.P., (editor), Gold '82: Rotterdam, A.A. Balkema Pub., pp. 521-552.

Franklin, J.M., 1996. Volcanic-associated massive sulfide in base metals. In: Eckstrand, O.R., Sinclair, W.D., and Thorpe, R.I., eds. Geology of Canadian Mineral Deposit Types. Geological Survey of Canada, no. 8, pp. 158-183.

Fyfe, W.S., Kerrich, R., 1984. Gold: Natural concentration processes, In: Foster, R.P., (editor), Gold '82: Rotterdam, A.A. Balkema Pub., pp. 99-128.

Goldfarb, R.J., Groves, D.I., and Gardoll, D., 2001. Orogenic gold and geologic time: A global synthesis: Ore Geology Reviews, v. 18, pp. 1-75.

Goldfarb, R. J., Baker, T., Dube, B., Groves, D. I., Hart, C. J. R., Gosselin, P., 2005. Distribution, character, and genesis of gold deposits in metamorphic terrains. Society of Economic Geologists, Inc., Economic Geology 100th Anniversary Volume, pp. 407-450.

Grant, J.A., 1986. The isocon diagram—a simple solution to Gresens' equation for metasomatic alteration. Economic Geology 81, 1976-1982.

Groves, D.I., Barley, M.E., Cassidy, K.F., Hagemann, S.G., Ho, S.E., Hronsky, J.M.A., Mikucki, E.J., Mueler, A.G., McNaughton, N.J., Perring, C.S., Ridley, J.R., 1991. Archean lode-gold deposits: The products of crustal-scale hydrothermal systems. In: E.A. Laderia, (Editor), Brazil Gold '91: The Economics, Geology, Geochemistry and Genesis of Gold Deposits. Balkema, Rotterdam, pp. 299-305.

Groves, D.I., 1993. The crustal continuum model for late-Archean lode-gold deposits of the Yilgarn Block, Western Australia. In: Mineral Deposita, v. 28, pp. 366-374.

Guilbert, J.M, Park, C.F, Jr., 1986. The Geology of Ore Deposits, New York: W. H. Freeman and Company, pp. 857-862.

Hansen, V.L., 2009. Personal Communication, University of Minnesota-Duluth.

Hodgson, C.J., MacGeehan, P.J., 1982. A review of the geological characteristics of "gold only" deposits in the Superior province of the Canadian shield: Canadian Inst. Mining Metallurgy Spec. Vol. 24, p. 211-228.

Hoffman, A.T., 2007. Lithostratigraphy, Hydrothermal Alteration, and Lithogeochemistry of Neoarchean Rocks in the Lower and Soudan Member of the Ely Greenstone Formation, Vermilion District, Northeastern Minnesota: Implications for Volcanogenic Massive Sulfides; University of Minnesota Duluth M.S. thesis, 295 p., 1 plate.

Hollings, P., and Wyman, D., 2005. The geochemistry of trace elements in igneous systems: principles and examples from basaltic systems. In: Linnen, R.L., and Samson, I.M., eds., Rare-Element Geochemistry and Mineral Deposits: Geological Association of Canada, GAC Short Course Notes 17, pp. 1-16.

Hooper, P., and Ojakangas, R., 1971. Multiple deformation in the Vermilion district, Minnesota: Canadian Journal of Earth Sciences, v. 8, pp. 423-434.

Hudak, G.J., 2008. Personal communication, University of Minnesota-Duluth.

Hudak, G.J., 2009. Personal communication, University of Minnesota-Duluth.

Hudak, G.J., Heine, J., Hocker-Finamore, S.M., Hauck, S., 2002a. Geologic Mapping of the Needleboy Lake-Six Mile Lake Area, Northeastern Minnesota: A Summary of Volcanogenic Massive Sulfide Potential; Report of Investigations NRRI/RI-2002/14.

Hudak, G.J., Heine, J., Newkirk, T., Odette, J., and Hauck, S., 2002b. Comparative Geology, Stratigraphy, and Lithogeochemistry of the Five Mile Lake, Quartz Hill, and Skeleton Lake VMS Occurrences, Western Vermilion District, NE Minnesota: A report to the Minerals Coordinating Committee, Minnesota Dept. of Natural Resources, Report No: NRRI/TR-2002/03 390 p.

Hudak, G.J., Heine, J., Jirsa, M.A., Peterson, D.M., 2004. Volcanic stratigraphy, hydrothermal alteration, and VMS potential of the Lower Ely Greenstone, Fivemile Lake to Sixmile Lake Area: *in* Severson, M. and Heinz, J., 2004, 50th Annual Meeting Institute on Lake Superior Geology, Proceedings Volume 50, Part 2 – Field Trip Guidebook, pp. 1-44.

Hudak, G.J., Hocker-Finamore, S.M., Heine, J., 2006. Field Distribution, Petrography, and Lithhogeochemistry of Epodosites in the Vicinity of Fivemile, Needleboy and Sixmile Lakes, Vermilion District, NE Minnesota: Proceedings of the 52nd ILSG Annual Meeting, Volume 52, Part 1, pp. 30-31.

Hudleston, P.J., 1976. Early deformational history of Archean rocks in the Vermilion district, northeastern Minnesota: Canadian Journal of Earth Sciences, v. 13, pp. 579-592.

Hutchinson, R.W., 1976. Lode gold deposits: The case for volcanogenic derivation, In: Proceedings volume, Pacific Northwest mining and metals conference, Portland, Oregon, 1975: Portland, Oregon Dept. Geology Mineral Industries, pp. 64-105.

Hutchinson, R.W., Burlington, J.L., 1984. Some broad characteristics of greenstone belt gold lodes, In: Foster, R.P., (editor), Gold '82: Rotterdam, A.A. Balkema Pub., pp. 339-372.

Hutchinson, R.W., 1987. Metallogeny of Precambrian Gold Deposits: Space and Time Relationships. Econ. Geol. Vol. 82, pp. 1993-2007.

Jahn, B.M., Murthy, V.R., 1975. Rb-Sr ages for the Archean rocks from the Vermilion District, northeastern Minnesota: Geochimica et Cosmochimica Acta, v. 39, pp. 1679-1689.

Jenner, G.A., 1996. Trace element geochemistry of igneous rocks: geochemical nomenclature and analytical geochemistry. In: Wyman, D.A., ed., Trace Element Geochemistry of Volcanic Rocks: Applications For Massive Sulphide Exploration: Geological Association of Canada, Short Course Notes, v. 12, p. 51-77.

Jirsa, M.A., 2000. The Midway sequence: a Timiskaming-type pull-apart basin deposit in the western Wawa subprovince, Minnesota: Canadian Journal of Earth Sciences, v. 37, pp. 1-15.

Jirsa, M.A., Southwick, D.L., and Boerboom, T.J., 1992. Structural evolution of Archean rocks in the western Wawa subprovince, Minnesota: Refolding of pre-cleavage nappes during D_2 transpression: Canadian Journal of Earth Sciences, v. 29, pp. 2146-2155.

Jirsa, M.A., Boerboom, T.J., and Peterson, D.M., 2001. Bedrock geologic map of the Eagles Nest quadrangle, St. Louis County, Minnesota: Minnesota Geological Survey Miscellaneous Map Series M-114, scale 1:24,000.

Jirsa, M.A., Boerboom, T.A., 2003. Bedrock geology of the Vermilion Lake quadrangle, northeast Minnesota: Minnesota Geological Survey Miscellaneous Map Series M-141, scale 1:100,000.

Jongewaard, P.K., 1989. Physical Volcanology and Hydrothermal Alteration of the Footwall Rocks to the Archean Sturgeon Lake Massive Sulfide Deposit, Northwest Ontario; University of Minnesota Duluth M.S. thesis, 140 p., 3 plates.

Lin, S., Parmenter, A., Parks, J., 2005. Synchronous vertical and horizontal tectonism at the late stage of Archean cratonization: an important process in gold mineralization? In: Mao, J., Bierlein, F. (Eds.), Mineral Deposit Research: Meeting the Global Challenge. Proceedings of the 8th Biennial SGA Meeting, Beijing, China, 18-21 August 2005, Springer Verlag, v. 1, pp. 29-32.

Meyer, C., 1988. Ore deposits as guides to geologic history of the earth: Ann. Rev. Earth Planet. Sci., v. 16, pp. 141-171.

Mikucki, E. J., 1998. Hydrothermal transport and depositional processes in Archean lode-gold systems: A review. Ore Geol. Rev. 13, pp. 307-321

Miller, J.D., Jr., Green, J.C., Severson, M.J., Chandler, V.W., Hauck, S.A., Peterson, D.M., Wahl, T.E., 2002. Geology and mineral potential of the Duluth Complex and related rocks of northeastern Minnesota: Minnesota Geological Survey Report of Investigations 58, 207 p.

Miller, L.D., Barton, C.C., Fredericksen, R.S., Bressler, J.R., 1992. Structural evolution of the Alaska-Juneau gold deposit, southeastern Alaska. Canadian Journal of Earth Science 29, pp. 865-878.

Moosavi, S., Johnson, T., Wendlend, C., Johnson, A., Hudak, G., 2007. Bedrock Geology Map of the Footwall to the Soudan Iron Formation South of Twin Lakes, St. Louis County, Northeastern Minnesota. Precambrian Research Center, Geological Map Series Map 2007-4, Natural Resources Research Institute, University of Minnesota-Duluth.

Newmont Exploration Limited, 1991. Fivemile Lake Project/Murray Joint Venture: Summary Report of Exploration Data; Eastern Portion, v. 1 of 3.

Newmont Exploration Limited, 1991. Fivemile Lake Project/Murray Joint Venture: Summary Report of Exploration Data; Western Portion, v. 2 of 3.

Ojakangas, R.W., 1972. Archean volcanogenic graywackes of the Vermilion district, northeastern Minnesota: Geological Society of America Bulletin, v. 83, pp. 429-442.

Ojakangas, R.W., Sims, P.K., Hooper, P.R., 1978. Geologic map of the Tower quadrangle, St. Louis County, Minnesota: U.S. Geological Survey, Geologic Quadrangle Map GQ-1457, scale 1:24,000.

Peterson, D.M., 2001. Development of Archean Lode-Gold and Massive Sulfide Deposit Exploration Models using Geographic Information System Applications: Targeting Mineral Exploration in Northeastern Minnesota from Analysis of Analog Canadian Mining Camps; University of Minnesota Ph.D. thesis, 503 p., 12 plates, 1 CD-Rom.

Peterson, D.M., 2007. Personal communication, University of Minnesota-Duluth.

Peterson, D.M., Jirsa, M.A., 1999(a). Bedrock geologic map and mineral exploration data, western Vermillion district, St. Louis and Lake Counties, northeastern Minnesota: MGS Miscellaneous Map M-98, scale 1:48,000.

Peterson, D.M., Jirsa, M.A., 1999(b). Lode gold and massive sulfide prospects in the Archean western Vermilion district: Minnesota Exploration Association, Minnesota Exploration Conference, Field Trip Guidebook, 10 maps, 30 p.

Peterson, D.M., Patelke, R.L., 2003. National underground science and engineering laboratory (NUSEL): geological site investigation for the Soudan Mine, northeastern Minnesota. Economic Geology Group, National Resources Research Institute, University of Minnesota Duluth: Technical Report NRRI/TR-2003/29.

Peterson, D.M., Patelke, R.L., 2004. Bedrock geology and lode gold prospect data map of the mud creek road area, northern Saint Louis County, Minnesota. Economic Geology Group, National Resources Research Institute, University of Minnesota Duluth: NRRI Map 2004-01.

Peterson, D.M., Patelke, R.L., 2004. Economic geology of Archean gold occurrences in the Vermilion district, northeast of Soudan, Minnesota; Institute on Lake Superior Geology, 50th Annual Meeting; National Resources Research Institute, University of Minnesota Duluth: Field trip guidebook, 27 p.

Petit, J.P. , 1987. Criteria for the sense of movement on fault surfaces in brittle rocks. J. Struct. Geol. Vol. 9, pp. 597 to 608.

Pirajno, F., 1992. Hydrothermal mineral deposits: principles and fundamental concepts for the exploration geologist, Berlin; New York: Springer-Verlag, pp. 100-155.

Rey, P.F., Coltice, N., 2008. Neoarchean lithospheric strengthening and the coupling of Earth's geochemical reservoirs. Geology, August 2008; v. 36; no. 8; p. 635-638.

Ridely, J.R., 1990. Source of ore fluid and ore components: alteration assemblages. Geology Department (Key Centre) and University Extension, The University of Western Australia Publication 20: pp. 268-272.

Robert, F., Brown, A.C., 1986. Archean gold-bearing quartz veins at the Sigma mine, Abitibi greenstone belt, Quebec: Part I. Geologic relationships and formation of the vein system: Econ. Geol., v. 81, pp. 578-592.

Robert, F., Poulsen, H.K., Cassidy, K.F., Hodgson, C.J., 2005. Gold metallogeny of the Superior and Yilgarn cratons. Society of Economic Geologists, Inc., Economic Geology 100th Anniversary Volume, pp. 1001-1033.

Robinson, L., ed., 2005. Field trip guidebook for selected geology in Minnesota and Wisconsin. Minnesota Geological Survey Guidebook 21, 278 p.

Rollinson, H., 1993. Using geochemical data: Evaluation, presentation, interpretation. Longman, Harlow, England. 352 p.

Saunders, A.D., Tarney, J., Marsh, N., Wood, D., 1980. Ophiolites as ocean crust or marginal basin crust: a geochemical approach. In: Panayiotou, F., ed., Ophiolites:

Proceedings of the International Ophiolite Symposium Cyprus 1979, Ministry of Agriculture and Natural Resources, Geological Survey Department, Cyprus, pp. 193-204.

Seward, T. M., 1993. The hydrothermal geochemistry of gold. In: Foster, R. P., (Ed.), Gold Metallogeny and Exploration, Chapman and Hall, London, pp. 37-62.

Schultz, K. J., 1980. The magmatic evolution of the Vermillion Greenstone belt, NE Minnesota. Precambrian Res., 11, pp. 215-245.

Sibson, R. H., 1977. Kinetic shear resistance, fluid pressures and radiation efficiency during seismic faulting. Pageoph, Vol. 115, pp. 387-400.

Sibson, R. H., 1987. Earthquake rupturing as a mineralizing agent in hydrothermal systems. Geology, Vol. 15, pp. 701-704.

Sibson, R. H., 1992. Earthquake faulting, induced fluid flow, and fault-hosted gold-quartz mineralization. In: Bartholomew, M. J., Hyndman, D. W., Mason, R., Mogk, D. W., (Editors.), Basement Tectonics 8: Characterization and Comparison of Ancient and Mesozoic Continental Margins—Proceedings of the 8th International Conference on Basement Tectonics (Butte, Montana, 1988) Kluwer Academic Publishers, Dordecht, The Netherlands, pp. 603-614.

Sibson, R. H., 2004. Controls on maximum fluid overpressure defining conditions for mesozonal mineralization. J. Struct. Geol. Vol. 26, pp. 1127-1136.

Sibson, R.H., 2007. Au-quartz mineralization near the base of the continental seismogenic zone. In: Ries, A.C., Butler, R.W.H., Graham, R.H., (editors), Deformation of the Continental Crust: The Legacy of Mike Coward. Geological Society of London, Special Publications, 272, pp. 519-532.

Sibson, R. H., Poulsen, K. H., Robert, F., 1988. High-angle reverse faults, fluid-pressure cycling, and mesothermal gold-quartz deposits. Geology, Vol. 16, pp. 551-555.

Sibson, R. H., Scott, J., 1998. Stress/fault controls on the containment and release of overpressured fluids: Examples from gold-quartz vein systems in Juneau, Alaska; Victoria, Australia and Otago, New Zealand. Ore Geol. Rev. 13, pp. 293-306.

Sims, P.K., Morey, G.B., Ojakangas, R.W., Griffin, W.L., 1968. Preliminary geologic map of the Vermilion district and adjacent areas, northern Minnesota: Minnesota Geological Survey, Miscellaneous Map Series M-5, scale 1:125,000.

Sims, P.K., 1972. Banded iron-formation in Vermilion district, *in* Sims, P.K., and Morey, G.B., editors, Geology of Minnesota; a centennial volume: Minnesota Geological Survey, pp. 79-81.

Sims, P.K., 1973. Geologic map of western part of Vermilion district, northeastern Minnesota: Minnesota Geological Survey, Miscellaneous Map Series M-13, scale 1:48,000.

Sims, P.K., 1976. Early Precambrian tectonic-igneous evolution of the Vermilion district, northeastern Minnesota. Geological Society of America Bulletin 87, pp 379-389.

Sims, P. K., and Southwick, D. L., 1980. Geologic map of the Soudan quadrangle, St. Louis County, Minnesota: U.S. Geological Survey, Geologic Quadrangle Map GQ-1540, scale 1:24,000.

Sims, P.K., 1985. Generalized bedrock geologic map of west-central Vermillion district, northern Minnesota: U.S. Geological Survey, Miscellaneous Investigation Series Map I-1529, scale 1:48,000.

Sims, P. K., and Southwick, D. L., 1985. Geologic map of Archean rocks, western Vermillion district, northern Minnesota: U.S. Geological Survey, Miscellaneous Investigations Map I-1527, scale 1:48,000.

Southwick, D.L., 1985. Bedrock geologic map of the Soudan-Big Fork area, northern Minnesota: Minnesota Geological Survey, Miscellaneous Map Series M-79, scale 1:100,000.

Southwick, D. L., 1993. Bedrock geologic map of the Soudan-Bigfork area, northern Minnesota: Minnesota Geological Survey Miscellaneous Map Series Map M-79, scale 1:100,000.

Tchalenko, J.S., 1970. Similarities between Shear Zones of Different Magnitudes. Geological Society of America Bulletin, v. 81, pp. 1625-1640.

Thompson, J.E., Hawley, J.E., Ward, W., Perry, O.S., Griffen, K., Charlewood, C.H., Hopkins, H., MacIntosh, C.G., Ogryzlo, S.P., 1948. Geology of the main ore zone at Kirkland Lake, Timiskaming district, Ontario: Ontario Dept. Mines, Ann. Rept., v. 57, pp. 54-188.

Twiss, R.J., Moores, E.M., 2007. Structural Geology. New York, New York: W. H. Freeman and Company, 736 p.

Winchester, J.A., Floyd, P.A., 1977. Geochemical discrimination of different magma series and the differentiation products using immobile elements: Chemical Geology, v. 20, p. 325-343.

Winter, J.D., 2001. An Introduction to Igneous and Metamorphic Petrology. Upper Saddle River, New Jersey: Prentice-Hall Inc., 697 p.